Trinity College Dublin
Coláiste na Tríonóide, Baile Átha Cliath
The University of Dublin

PhD DISSERTATION

OF

TRINITY COLLEGE DUBLIN

High Resolution Lithography Techniques for Applications in Plasmonic Nanomaterials

Submitted by:

Robert O'Meara

in Partial Fulfillment of the Requirements for the Degree of

DOCTOR OF PHILOSOPHY IN CHEMISTRY

Under the supervision of Prof. Richard Hobbs, Ph.D.

School of Chemistry and AMBER

Trinity College Dublin

The University of Dublin

2024

I declare that this thesis has not been submitted as an exercise for a degree at this or any other university and it is entirely my own work.

I agree to deposit this thesis in the University's open access institutional repository or allow the Library to do so on my behalf, subject to Irish Copyright Legislation and Trinity College Library conditions of use and acknowledgement.

I consent to the examiner retaining a copy of the thesis beyond the examining period, should they so wish (EU GDPR May 2018).

.....

Robert O'Meara

Acknowledgements

First and foremost I'd like to thank Prof. Richard Hobbs for his supervision and guidance throughout this PhD journey. Without his support and willingness to dedicate his time to assisting me, there is no way I would have made it this far, and I could have not asked for anything more out of a supervisor. I'd like to thank members of the Hobbs Group both past and present; Dr. Nebras Alatar, Dr. Ram Tak, Julian Carolan, Dr. Veerendra Dhyani, Dr. Kamonpan Chumpol, and Dr. Kenan Elibol, each of whom has helped greatly, whether it be through help with measurements, training, or just general advice and support.

I'd like to thank all of the technical staff who have helped me along the way. From the AML, I'd like to thank Dr. Megan Canavan, and Dermot Daly for training. I'd like to thank Clive Downing and Dr. Raman Bekarevich for help with taking TEM images. From the CRANN cleanroom, I'd like to thank Dr. Riley Gatensby and Dr. Peter Gleeson for help with training and sample preparation. I'd like to thank Dr. Jing Jing Wang from the photonics lab for help and training with Raman spectroscopy. It should go without saying that without the support of the technical staff, none of the work presented in this thesis would be possible.

I'd like to thank the funding bodies, SFI and AMBER, that have supported me during the PhD and for providing me with the means to access all of the equipment used throughout the PhD.

Finally I would like to thank my family and friends that have provided me with much needed emotional support throughout the last few years. To my parents and my sister, Niamh, without your love and continuous support and encouragement I would never have

made it this far. To my friends, in particular to Patrick, Lee, Susie, Ellen, Tigran, Frances, and Patrick who have been with me throughout every step of this journey, and to all my other friends who have supported me along the way; thank you so much for the support, advice, listening to my rants, and most importantly the laughs and good times. It is thanks to you that I have been able to that I've been able to enjoy this last few years so much.

"Think where man's glory most begins and ends, and say my glory was I had such friends."

W. B. Yeats

Summary

Metallic nanoparticles are of great scientific interest owing to their ability to support collective oscillations of electrons across their surface, known as localised surface plasmon resonances (LSPRs), when illuminated with light. These LSPRs amplify optical fields at the surface of the nanoparticle. The enhanced fields yield increased light-matter interactions, which have exciting applications in light-emitting devices, sensing, and the modification of the reactivity of chemical bonds via the formation of strongly-coupled systems. The enhanced fields can also result in the excitation of hot charge carriers which have applications in charge-transfer catalysis. The decay of hot carriers results in a localised heating of the nanoparticle that also has applications in catalysis. The LSPR wavelength is dependent on the metal used, the background medium, and the size and shape of the metal nanoparticle. As such, precise control over the dimensions of the metallic nanoparticle is essential for exploiting LSPRs for the aforementioned applications. Top-down fabrication methods such as electron-beam lithography (EBL) and helium ion beam lithography (HIBL) are ideal methods for the fabrication of plasmonic nanoparticles as they allow for the fabrication of arbitrary 2-D geometries with precise control of their on-chip location.

In this thesis, the limits of HIBL are investigated via the simulation and measurement of the point-spread functions of the He^+ ion beam in both poly (methyl methacrylate) (PMMA) and a fullerene-derivative resist suspended on ultrathin membranes. PSFs were measured by performing point exposures with varying He^+ ion beam dose. Transmission electron microscopy (TEM) was then employed to measure the average radius of the features produced as a function of beam dose. The experimental PSFs of both PMMA and the fullerene-derivative were then compared to a similar study carried out in PMMA ex-

posed using a state-of-the-art aberration-corrected STEM. The results indicate that HIBL has the potential to outperform aberration-corrected EBL for the patterning of dense arrays of nanostructures regardless of the pitch of the array.

In this work we used simulations alongside high-resolution EBL to design and fabricate various plasmonic Au nanoparticles. The enhanced optical properties the plasmonic nanoparticles were exploited to probe the coupling between a vibrational mode in a carbon nanodot and a plasmonic antenna. Finite-difference time domain (FDTD) simulations were used to determine the dimension of Au antennas capable of supporting both a mid-IR LSPR mode to couple with a graphitic G band peak, as well as a near-IR mode to couple with a Raman laser to allow the coupled system to be probed via surface-enhanced Raman spectroscopy (SERS). EBL was used to fabricate the segmented antennas, and the NIR resonance was confirmed using optical spectroscopy. To date, the presence of the IR LSPR mode has not been confirmed.

Finally, the application of the localised heating of plasmonic Au nanoparticles was investigated via the LSPR-induced growth of semiconductor materials. FDTD simulations were again used to design plasmonic Au nanoantennas having LSPRs resonant with an excitation laser. Au nanoparticles were fabricated using EBL and their resonance was confirmed using optical spectroscopy. Scanning electron microscopy (SEM), EDX, and TEM were used to confirm the growth of both crystalline Ge nanowires, and amorphous Ge. Preliminary results indicate the ZnO nanowires can also be grown via using the same experimental setup. It was determined that crystalline Ge is grown via a solution-liquid-solid growth mechanism. Amorphous Ge was determined to grow via the coffee-ring deposition of elemental Ge onto the surface of the Au nanoparticles due to the formation of air bubbles caused by the plasmonic heating of the precursor material. ZnO nanowires were also grown via a hydrothermal synthesis method. The growth of nanoscale semiconductor materials via a range of different mechanisms highlights the versatility of the LSPR-induced growth process.

Contents

Acknowledgements **iii**

Summary **v**

List of Figures **x**

1 Introduction **2**

1.1 Localised Surface Plasmon Resonance 2

1.1.1 Origin of LSPR 4

1.1.2 LSPR Field Enhancement 8

1.1.3 Coupling Between LSPR and Quantum Emitters 10

1.1.4 Hot Carriers 14

1.1.5 Thermal Losses 17

1.1.6 Plasmonic Materials 19

1.1.7 Geometric dependence of LSPR 21

1.2 Nanofabrication Techniques 24

1.2.1 Resolution of Photolithography Systems 26

1.2.2 Scanning Probe Lithography 29

1.2.3 Electron Beam Systems 30

1.2.4 Helium Ion Beam Systems 34

1.2.5 Electron and He^+ Ion Beam Lithography 36
1.2.6 Beam Diameter and Aberrations 39
1.2.7 Proximity Effect 41
1.2.8 Resists 41

2 Experimental Techniques **47**

2.1 Numerical Methods 47
2.1.1 Finite-Difference Time-Domain Method 49
2.1.2 FDTD Simulations 51
2.2 Optical Spectroscopy 53
2.3 FTIR Spectroscopy 54
2.4 Raman Spectroscopy 55
2.5 Transmission Electron Microscopy 57
2.6 Energy Dispersive X-Ray Spectroscopy 58
2.7 Fabrication of Nanostructures using Electron and Helium Ion Beam Lithography 60
2.7.1 Fabrication of Au Nanoantennas on ITO Substrates 60
2.7.2 Fabrication of Au Nanoantennas on TEM Membranes and X-Ray Windows 61
2.7.3 Fabrication of Negative-Tone Structures for Point-Spread Function Measurements 61
2.8 Simulation of Point-Spread Functions 62
2.9 Laser-Induced SLS Growth of Semiconductors 62

3 Measurement of the Point-Spread Function of a Focused Helium Ion Beam on Ultrathin Membranes **64**

3.1 Introduction 64
3.1.1 Proximity Effect 65
3.1.2 Sample Interaction 65
3.1.3 Fabrication on Ultra-Thin Membranes 67
3.1.4 HIBL Resists 68
3.2 Experimental 69
3.3 Results and Discussion 71
3.3.1 Negative-tone Structures Fabricated on Ultra-Thin Membranes . . 71
3.3.2 Determination of PSF 73
3.3.3 Comparison of HIBL to Aberration-Corrected EBL 74
3.3.4 Dose Contrast 78
3.3.5 Direct Imaging of PMMA Interaction Volume 80
3.4 Conclusions and Outlook 81

4 Plasmonic Nanoantennas for Strong Coupling to Molecular Vibrational Modes and Surface Enhanced Raman Spectroscopy 83

4.1 Introduction 83
4.1.1 Underlying Physics 84
4.1.2 Strong Coupling of Photonic Cavities to Molecular Vibrations . . 85
4.1.3 Surface-Enhanced Raman Spectroscopy (SERS) 87
4.2 Results 88
4.2.1 Design of IR Antennas 88
4.2.2 Fabrication of IR Antennas 90
4.2.3 Fabrication of Carbon Nanodots 91
4.2.4 Segmented Antenna Design 93

4.2.5 Fabrication of Segmented Antenna 93
4.2.6 Fabrication of Segmented Antennas on SiN_x X-ray Windows . . . 96
4.2.7 FTIR Spectroscopy of Segmented Antenna 98
4.2.8 Estimation of Coupling Between Carbon Nanodot and Segmented Antennas 99
4.3 Conclusions and Outlook 101

5 Localised Growth of Semiconductor Materials Driven by Localised Surface Plasmon Resonances 103

5.1 Semiconductor Nanomaterials 103
5.2 Fabrication of Nanocrystalline Germanium 105
5.2.1 Vapour-Liquid-Solid Growth of Semiconductor Nanowires 106
5.2.2 Laser Induced Growth of Semiconductor Nanowires 107
5.3 Results and Discussion 110
5.3.1 Optical Properties of Au Nanoantennas 110
5.3.2 Fabricated Au Bowties and Nanodiamonds on ITO 112
5.3.3 Growth of Ge on Bulk ITO on Glass Substrates 113
5.3.4 Fabrication of Au Nanodiamonds on SiN_x Membranes for TEM . 116
5.3.5 Growth of Ge on TEM Membranes 118
5.3.6 Elemental Analysis 119
5.3.7 Mechanism of SLS Growth of Ge Nanowires 121
5.3.8 Plasmon-Induced Growth of ZnO 124
5.4 Outlook 126

6 Conclusions 128

6.1 Thesis Summary 128

6.2 Future Directions 131

6.3 Final Remarks 134

7 Bibliography **ii**

A MATLAB Script Used to Generate Dose Contrasts Plots **xxvi**

B Data Generation for Simulated PSFs **xxxii**

C Lumerical Script to Calculate Extinction Spectra **xxxvii**

List of Figures

1.1 Localised surface plasmon resonance. 3

1.2 The Lycurgus cup. 4

1.3 Surface plasmon polariton. 5

1.4 Plasmonic field enhancement. 9

1.5 Vibrational strong coupling. 14

1.6 Plasmon decay. 16

1.7 Plasmon-induced hot carrier generation. 18

1.8 Dielectric function of metals. 19

1.9 Q_{LSPR} for common plasmonic metals. 21

1.10 Size dependence of LSPR. 23

1.11 Moore's Law. 27

1.12 Rayleigh criterion. 28

1.13 Schematic of a standard scanning electron microscope (SEM). 32

1.14 Electron beam interaction volume. 33

1.15 Helium ion microscope and trimer. 37

1.16 Schematic of a positive-tone EBL or HIBL process. 38

1.17 Spherical and chromatic aberrations. 39

1.18 Theoretical probe sizes of an electron and He^+ ion beam. 40

1.19 Resist contrast. 43

1.20 (a) Molecular diagram of generic fullerene resists. R represents the attached side chains to the C_{60} molecule. (b) Schematic showing the comparison between patterns formed from a high molecular weight resist and those from a low molecular weight resist after development.[1] 46

2.1 Position of the electric and magnetic field vector components about a cubic unit cell of the Yee space lattice. 50

2.2 Position of the electric and magnetic field vector components in space and time for a one-dimensional Yee cell. 51

2.3 Optical spectroscopy setup. 54

2.4 Inelastic scattering of light. 56

2.5 Schematic of a transmission electron microscope (TEM). 58

2.6 Schematic showing the generation of characteristic x-rays in an electron microscope. 59

2.7 Schematic of the setup used for the LSPR growth of Ge and ZnO. 63

3.1 Schematic of interaction of He^+ ion beam with the sample. 70

3.2 TEM images of negative-tone structures fabricated using HIBL. 72

3.3 Measurement of the thickness of the resist films. 73

3.4 Experimental and simulated PSFs for PMMA and a fullerene-derivative resist. 75

3.5 Comparison between HIBL and EBL. 76

3.6 Dose contrast of HIBL resists. 78

3.7 Direct measurement of HIBL interaction volume. 80

4.1 Simulated extinction spectrum of a strongly coupled system. 85

4.2 Schematic showing the strong coupling of a photonic cavity with a vibrational mode in a molecule. 86

4.3 Schematic of geometry of antennas capable of supporting both mid- and near-IR resonances. 89

4.4 Simulated extinction spectra of NIR and mid-IR plasmonic antennas. . . . 90

4.5 Antennas fabricated designed capable of supporting both mid- and NIR resonances. 91

4.6 Carbon nanodots fabricated in the centre of plasmonic nanoantennas using EBL. 92

4.7 Raman spectroscopy of a carbon nanodot. 92

4.8 Schematic and simulated spectra for a segmented plasmonic antenna. . . . 94

4.9 SEM micrograph of partially fabricated segmented nanoantenna. 95

4.10 Extinction and Raman spectra of a segmented plasmonic antenna. 96

4.11 Complete segmented nanoantennas fabricated on a 50-nm-thick SiN membrane. 96

4.12 Extinction spectra of segmented plasmonic antenna fabricated on a SiN_x membrane. 97

4.13 FTIR spectrum of segmented antenna. 98

4.14 Predicted extinction spectrum of carbon nanodot strongly coupled to a segmented plasmonic antenna. 100

5.1 SLS growth of Ge nanowires. 107

5.2 Simulations of plasmonic Au nanostructures. 111

5.3 Schematic of plasmonic nanostructure design. 112

5.4 SEM of plasmonic Au nanostructures fabricated by EBL. 114

5.5 LSPR-driven growth of Ge. 115

5.6 Simulated Au nanodiamonds on a SiN_x membrane. 117

5.7 SEM image of Au nanodiamonds fabricated on a SiN_x membrane. 117

5.8 Growth of Ge on Au nanodiamonds on a SiN_x membrane. 118

5.9 TEM images of Ge growth. 119

5.10 EDX spectra recorded from grown Ge. 120

5.11 Raman and extinction spectra of Ge nanowires. 121

5.12 SEM images of amorphous Ge. 122

5.13 Deposition of Ge on Au nanoantennas via the coffee-ring effect. 123

5.14 LSPR-induced growth of ZnO. 125

B.1 SRIM inputs used to generate He^+ ion trajectories for (a) PMMA and (b) a fullerene-derivative resist. xxxiii

Chapter 1

Introduction

1.1 Localised Surface Plasmon Resonance

A localised surface plasmon resonance (LSPR) refers to the collective oscillation of the electron gas cloud at the surface of a metal nanoparticle in response to an incident electromagnetic field. When the particle is illuminated at resonance the electron cloud is displaced relative to the nuclei. A restoring force arises due to the Coulombic attraction between the electron cloud and the nuclei, resulting in a periodic oscillation of the electron cloud. During this oscillation, the electron cloud is not distributed evenly around the particle and there is a transient accumulation of electrons on one side of the particle. The accumulation of electrons within a small volume leads to an enhancement of the electric fields around the nanoparticle. The extinction of light is proportional to the electric field intensity E^2, therefore the enhanced fields caused by LSPR result in a strong increase in the extinction of a metallic nanoparticle at the LSPR frequency. The wavelength at which the resonance, and thus the enhanced extinction occurs is dependent on the size and geometry of the metallic particle, as well as the metal used and the medium in which the particle resides. Noble metal nanoparticles have resonances across the visible and NIR region of the spectrum, making them an attractive choice for applications in light harvesting technologies. This enhanced absorption has been exploited since ancient times, with the most famous example being the Lycurgus cup. This cup, dating from the 4th-century

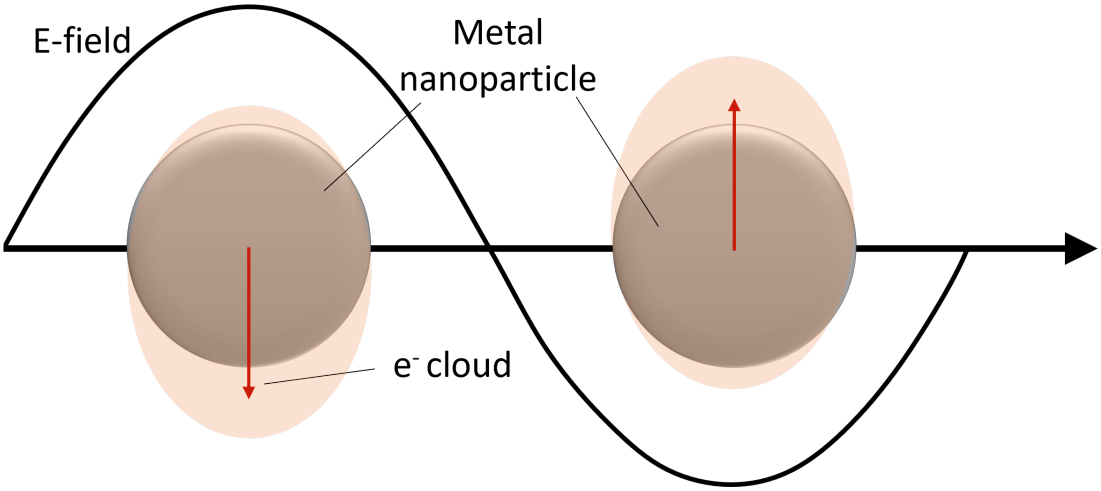

Figure 1.1: Schematic of the excitation of the localised surface plasmon resonance in response to an incident electric field.

CE, contains colloidal Au and Ag nanoparticles and as a result shows a different colour depending on whether it is being illuminated from the front or the back *i.e.,* transmission or reflection.

The enhanced absorption of light can also excite hot carriers in the nanoparticles *i.e.,* hot electrons or holes with energies corresponding to thousands of degrees of Kelvin.[2] To date, hot carriers excited by LSPR have been exploited for charge transfer processes in photocatalysis and the development of improved optoelectronic devices.[3–7] Furthermore, the relaxation of hot carriers can result in the heating of the nanoparticle and its local environment.[8] This localised heating allows plasmonic metal nanoparticles to be used as nanoscale heat sources.[9] In order for the potential of plasmonic nanoparticles to be fully realised, precise control of the wavelength at which they are resonant, and thus the geometry of the nanoparticle, is required. Bottom-up synthetic techniques have to date been used to fabricate a broad variety of complex geometries of plasmonic nanoparticles at large scales.[9–11] However, it is not possible to explicitly control the placement of individual nanoparticles. Furthermore, tuning the dimensions or geometries of synthesised nanoparticles is not trivial, and size distributions may be larger than for lithography-based methods. In addition to this limitation, the fabrication of devices made from nanoparticles demands precise control of the on-chip location of individual nanoparticles. The use of top-down fabrication methods such as electron and helium-ion-beam lithography allow

Figure 1.2: The Lycurgus cup is an artefact from the 4^{th} century that appears green when illuminated from the front (reflection) and red when illuminated from the back (transmission) due to the presence of plasmonic Ag and Au nanoparticles.[12]

for explicit control of the location and dimensions of plasmonic nanoparticles, allowing for LSPRs to be tuned precisely for a desired application.

1.1.1 Origin of LSPR

Surface plasmons (SPs) are quantized electromagnetic surface waves localised at the interface between a plasma, typically electrons in a metal, and a dielectric. The SP propagates along the interface as shown in Figure 1.3(a). SPs possess both transverse and longitudinal components. The transverse component of the SP can interact directly with photons. This interaction is sufficiently strong that the photon and SP form a coupled system known as a surface plasmon polariton (SPP). To find the dispersion of the SPP we assume the metal is characterized by a general, complex frequency-dependent dielectric

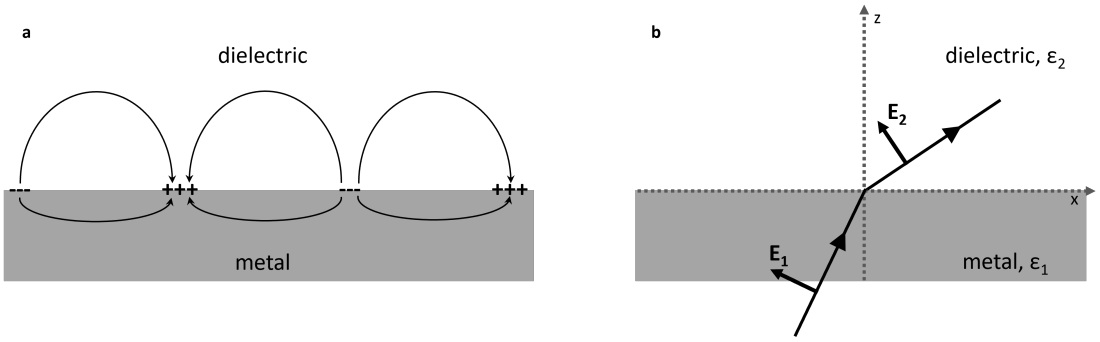

Figure 1.3: (a) A surface plasmon polariton propagating along a metal-dielectric interface. (b) Interface between a metal and dielectric with dielectric functions ϵ_1 and ϵ_2 respectively. The interface is defined by $z = 0$.

function:

$$\epsilon_1(\omega) = \epsilon_1' + i\epsilon_1''. \tag{1.1}$$

The real part of the dielectric function, ϵ_1', describes the strength of the polarization induced by an electric field, whereas the imaginary part, ϵ_1'', represents the losses encountered in polarizing the material *i.e.,* the absorption of the medium.[13] The dielectric function, $\epsilon_2(\omega)$, of the dielectric medium is assumed to be real valued only *i.e.,* no losses. We define the axes such that $z = 0$ coincides with the interface. We are looking for homogeneous solutions of Maxwell's equations that are localised at the surface. A homogeneous solution is an eigenmode of the system *i.e.,* it exists without external excitation. Mathematically, it is the solution to the wave equation:

$$\nabla \times \nabla \times \boldsymbol{E}(\boldsymbol{r}, \omega) - \frac{\omega^2}{c^2}\epsilon(\boldsymbol{r}, \omega)\boldsymbol{E}(\boldsymbol{r}, \omega) = 0 \tag{1.2}$$

where $\epsilon(\boldsymbol{r}, \omega) = \epsilon_1(\omega)$ if $z < 0$, and $\epsilon(\boldsymbol{r}, \omega) = \epsilon_1(\omega)$ if $z > 0$. The localization at the interface is characterized by electromagnetic fields that exponentially decay as they move into either medium. There are no solutions for the case of s-polarisation so we will consider only p-polarised waves. For p-polarised waves in half-spaces $j = 1, 2$, we have:

$$\boldsymbol{E}_j = \begin{pmatrix} E_{j,x} \\ 0 \\ E_{j,z} \end{pmatrix} e^{ik_x x - i\omega t} e^{ik_{j,z} z} \qquad j = 1, 2. \tag{1.3}$$

As the wavevector parallel to the interface is conserved we have:

$$k_x^2 + k_{j,z}^2 = \epsilon_j k^2, \quad j = 1, 2. \tag{1.4}$$

Here, $k = 2\pi/\lambda$ where λ is the vacuum wavelength. As the displacement fields in both half-spaces have to be source free *i.e.,* $\nabla \cdot \boldsymbol{D} = 0$, we have:

$$k_x E_{j,x} + k_{j,z} + E_{j,z} = 0, \quad j = 1, 2. \tag{1.5}$$

Combining Equations 1.4 and 1.5, we can rewrite Equation 1.3 as:

$$\boldsymbol{E}_j = E_{j,x} \begin{pmatrix} 1 \\ 0 \\ -k_x/k_{j,z} \end{pmatrix} e^{ik_{j,z}z}, \quad j = 1, 2. \tag{1.6}$$

The factor $e^{ik_x x - i\omega t}$ has been omitted in order to simplify the notation. As we require continuity of the parallel components of $\boldsymbol{E}$ and the perpendicular component of $\boldsymbol{D}$, we obtain the following set of equations:

$$\begin{aligned} E_{1,x} - E_{2,x} &= 0, \\ \epsilon_1 E_{1,z} - \epsilon_2 E_{2,z} &= 0. \end{aligned} \tag{1.7}$$

Equations 1.7 and 1.5 form a homogeneous system of four equations for the four unknown field components. The existence of a solution requires that the respective determinant vanishes. This happens either for $k_x = 0$, which does not describe excitations that travel along the interface, or for:

$$\epsilon_1 k_{2,z} - \epsilon_2 k_{1,z} = 0. \tag{1.8}$$

Combining Equations (1.4) and (1.8) we have a dispersion relation *i.e.,* a relationship between the wavevector along the direction of propagation and the angular frequency ω:

$$k_x^2 = \frac{\epsilon_1 \epsilon_2}{\epsilon_1 + \epsilon_2} k^2 = \frac{\epsilon_1 \epsilon_2}{\epsilon_1 + \epsilon_2} \frac{\omega^2}{c^2}. \tag{1.9}$$

We also obtain an expression for the normal component of the wavevector:

$$k_{j,z}^2 = \frac{\epsilon_j^2}{\epsilon_1 + \epsilon_2} k^2, \quad j = 1, 2. \tag{1.10}$$

For simplicity it is assumed that the imaginary parts of both complex dielectric functions are small compared to the real parts, and therefore they can be ignored. The existence of propagating waves at the interface requires a real value for k_x. From Equation (1.9) this can be fulfilled if the sum and the product of the dielectric functions are either both positive or both negative. In order to obtain a 'bound' solution, we require that the normal components of the wavevector are purely imaginary in both media, giving rise to exponentially decaying solutions. This is only possible if the denominator in Equation (1.10) is negative. From this we can conclude that for an interface mode to exist we require:

$$\epsilon_1(\omega) \cdot \epsilon_2(\omega) < 0, \tag{1.11}$$

$$\epsilon_1(\omega) + \epsilon_2(\omega) < 0. \tag{1.12}$$

This means that one of the dielectric functions must be negative with an absolute value larger than the other. Metals, in particular noble metals, have a large negative real part of the dielectric function as well as a small complex part. Consequently, the interface between a noble metal and a dielectric can support localised modes.

The dielectric function of an electron plasma can be derived from the Drude-Lorentz model as:

$$\epsilon_i(\omega) = 1 - \frac{\omega_p^2}{\omega^2 + i\gamma\omega}, \tag{1.13}$$

where ω is the angular frequency of the incident light, γ is the damping term, and ω_p is the plasma frequency given by:

$$\omega_p = (\frac{Ne^2}{\epsilon_0 m_0})^{1/2}. \tag{1.14}$$

Here *N* is the number density of electrons, *e* is the electron charge, ϵ_0 is the vacuum permittivity, and m_0 is the electron rest mass. For a lightly damped system *i.e.,* $\gamma = 0$,

we have:

$$\epsilon_i(\omega) = 1 - \frac{\omega_p^2}{\omega^2}. \tag{1.15}$$

From Equation (1.9), it can be seen that $k_x \to \infty$ when $\epsilon_1 = -\epsilon_2$. Substituting this into Equation (1.15) we find:

$$\omega_{sp} = \frac{\omega_p^2}{\sqrt{1+\epsilon_2}}, \tag{1.16}$$

where ω_{sp} is the surface plasmon resonance frequency. For the case of air ($\epsilon_2 = 1$), it can be seen that:

$$\omega_{sp} = \frac{\omega_p^2}{\sqrt{2}}. \tag{1.17}$$

So far we have only considered SPPs propagating along a metal-dielectric interface. In the case of metallic nanoparticles, the SPPs do not propagate as they are bound to the surface of the nanoparticle. Consequently, they are known as localised surface plasmons. If we consider a metallic nanoparticle with radius a much smaller than the wavelength of light, then the polarizability of the particle is given by:

$$\alpha = 4\pi a^3 \frac{\epsilon_1 - \epsilon_2}{\epsilon_1 + 2\epsilon_2}. \tag{1.18}$$

It can be seen in this case that resonance occurs when $\epsilon_1 = -2\epsilon_2$. For an undamped plasma in air we have:

$$\omega_{sp} = \frac{\omega_p^2}{\sqrt{3}}, \tag{1.19}$$

and the resonance is independent of particle size. However, in real metals, the frequency of the resonance is shifted due to the presence of interband transitions, and depends on the size of the particle.

1.1.2 LSPR Field Enhancement

When the LSPR of a nanoparticle is excited resonantly by light, the oscillation of the electron cloud results in a large electric dipole around the particle. This dipole can result in intense electric fields localised at the surface of the particle with an intensity that can be many orders of magnitude larger than the incident field.[14,15] These regions

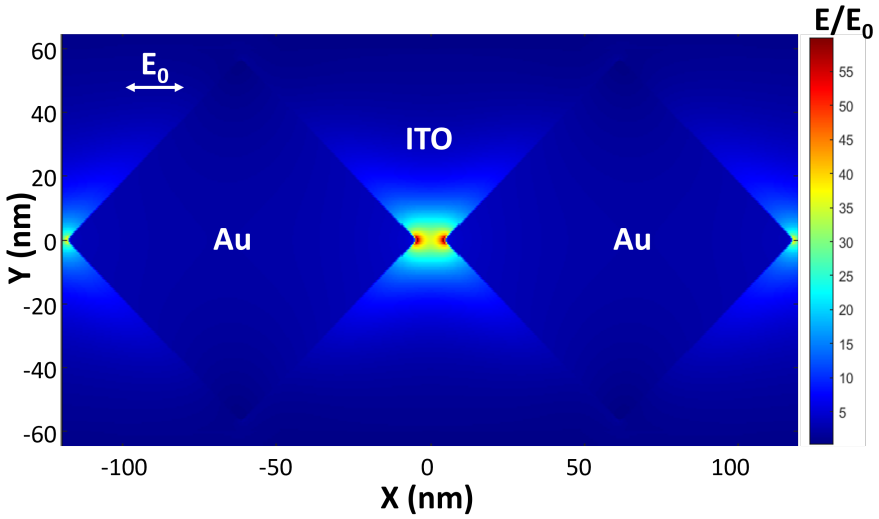

Figure 1.4: Simulated electric fields around a pair of Au nanodiamonds excited at their LSPR wavelength. The field enhancement can be seen to be at its strongest in the nanoscale gap between the nanodiamonds. The arrow marks the polarisation of the incident electric field, E_0.

near the surface of the nanoparticle that exhibit enhanced fields are known as plasmonic hot spots. Plasmonic hot spots are of great interest to researchers and to date have been exploited for applications in sensing, catalysis, and optical waveguides.[16,17]

Plasmonic hot spots are the basis for surface enhanced Raman scattering (SERS). The LSPR enhances both the incident laser field, as well as Raman scattered field. Consequently, the overall enhancement roughly scales as E^4, allowing this technique to detect single particles.[16] As mentioned previously, the absorption band of metallic nanoparticles is dependent on their LSPR, which is dependent on the geometry of the nanoparticle as well as the refractive index of the medium. The binding of an analyte to the surface of a nanoparticle can result in a change in the local dielectric function of the nanoparticle, resulting in a detectable shift of the LSPR wavelength.[18] It is also possible that the binding of an analyte can cause the coupling of the fields of multiple nanoparticles, or even aggregation as the analyte brings the nanoparticles into close proximity with each other. This causes a shift in the LSPR, which can be strong enough for detection as a colour change perceivable to the naked eye. For example, Lee *et. al.,*[19] used DNA-functionalised Au nanoparticles for the detection of Hg^{2+} ions. When Hg^{2+} is introduced to the system it selectively coordinates to the mismatched T-T base pair, resulting in an aggregated

nanoparticle system and allows the quantification of Hg^{2+} concentration based on the observed colour change.

Plasmonic hot spots can also be used in photocatalytic reactions. For example, Hou *et. al.*[20] demonstrated that the photocatalytic performance of TiO_2 films could be enhanced by Au nanoparticles. As the plasmonic hot spots of the Au nanoparticles overlaps directly with the TiO_2, the photoabsorption, and thus electron-hole pair generation in the TiO_2, is also enhanced. The authors reported a 9-fold improvement in the photocatalytic rate of decomposition of methyl orange when using the Au-TiO_2 composite compared to using TiO_2 only. The confinement of light at the metal-dielectric interface makes it possible for the diffraction limit to be broken and allows for the fabrication of subwavelength optical waveguides.[17]

1.1.3 Coupling Between LSPR and Quantum Emitters

The enhanced fields generated by a LSPR can also intensify the light-matter interaction with quantum emitters (QEs)[21] via the formation of a coupled system. QEs are systems where the light-matter interaction can be approximated as consisting of only two energy levels.[22] The QE can absorb a photon, thereby exciting an electron from the ground state to the higher energy excited state level. The relaxation of the excited electron can then result in emission of a photon with equivalent energy to the transition between the excited and ground states. Some examples of QEs include atoms, molecules, and excitons in semiconductors. To achieve enhanced emission, the QE must be placed in the hot spot of a plasmonic structure, such as a nanogap antenna.[23] Furthermore, the coupling relation between the LSPR and the QE must be well understood. From the Jayne-Cummings model,[24] the probability that a coupled system is in its excited state at a given time, t, is given by the equation

$$P_e(t) = cos^2(\Omega_R\sqrt{n\ +\ 1}t) \tag{1.20}$$

where n represents the number of photons in the system. It can be seen from this equation that there will be times when an electron is guaranteed to be found in the excited

state, $P_e(t) = 1$, when it has absorbed energy from the resonator, and times when it is guaranteed to be found in the ground state, $P_e(t) = 0$, when it transmits a photon back into the resonator. For $n = 0$, this periodic exchange of energy between the emitter and the resonator has a frequency of twice the value of Ω_R, the vacuum Rabi frequency given by

$$\Omega_R = \mu E_{LSPR} = 2\mu\sqrt{\frac{\hbar\omega}{2\epsilon_0 V_0}}. \tag{1.21}$$

Here, μ is the transition dipole moment of the emitter, and E_{LSPR} is the LSPR field strength, confined to the metal-dielectric surface. Two coupling regimes exist, with weak coupling occurring if $\Omega_R^2 \leq \frac{\gamma_{QE}^2}{2} + \frac{\gamma_{LSPR}^2}{2}$, and strong coupling occurring when $\Omega_R^2 \geq \frac{\gamma_{QE}^2}{2} + \frac{\gamma_{LSPR}^2}{2}$. Here, γ_{QE} and γ_{LSPR} are the dephasing rates of the QE and LSPR respectively.[25,26] In the weak coupling regime there is enhancement or suppression of radiative damping. In the strong coupling regime there is periodic energy transfer between the LSPR and the QE.

1.1.3.1 Weak Coupling Regime

In the weak coupling regime, also known as the Purcell regime, there are substantial changes in emitter dynamics, but the resonance frequency is only weakly affected.[27,28] The resonator relaxation rate is enhanced by a factor known as the Purcell factor given by

$$F_p = \frac{3}{4\pi^2}(\frac{\lambda_0}{n_0})^3\frac{Q}{V_0}, \tag{1.22}$$

where λ_0 is the free-space wavelength associated with the transition, n_0 is the refractive index, Q is the quality factor of the resonator, and V_0 is the mode volume.[29,30] In proximity to a plasmonic structure, the vacuum field near the LSPR resonance frequency is enhanced, increasing the mode density of states compared to that in free space. The Purcell enhancement factor reflects this increase in the density of states.[31] For a LSPR supported by a metallic nanoparticle, the optical fields can be confined to length scales comparable to the dimensions of the nanoparticles *i.e.* on the order of 10 nm. Mode volumes on the order of $10^{-6}(\lambda_0/n_0)^3$ are obtainable in the gap between two closely spaced nanoparticles.[32] Therefore, precise fabrication of metallic nanostructures with a

well-defined gap between them is required to fully exploit the Purcell enhancement of emission from QEs.

The weak coupling between plasmonic nanoparticles and a QE can modify both the excitation rate of the emitter, as well as its emission rate.[33] In both cases, good spectral overlap between the LSPR and the excitation (absorption) and emission spectra is required for the respective rates to be enhanced. The excitation enhancement strongly depends on the orientation of the emitter dipole with respect to the electric field polarisation of the LSPR. Höppener *et al.,*[34] demonstrated a 40-fold fluorescence enhancement of Nile blue molecules by the coupling of plasmonic Au trimer nanoparticles to the absorption spectrum of the fluorescent molecule. A photoluminescence (PL) enhancement of 300 was reported by Brolo *et al.,*[35] for the coupling of CdS quantum dots (QDs) to the surface plasmon (SP) modes of a nanohole array on a metal film. This high enhancement factor was attributed to coupling of the SP to both the excitation and emission fields of the QD. The direction and polarisation of the emitted light can also be modified by coupling of the LSPR to a QE,[36,37] allowing for greater control of light at the nanoscale. Ratchford *et al.,*[38] demonstrated the reversibility of the weak coupling of a single Au nanoparticle to a CdSe/ZnS QD. By using an AFM tip to position the Au nanoparticle, a reduction in the PL lifetime of the nanoparticle from 30 ns for an isolated QD to less than 1 ns for a coupled QD-Au NP system was observed. The Au nanoparticle was subsequently pushed far away from the QD to demonstrate that the coupling is reversible.

1.1.3.2 Strong Coupling Regime

When the Rabi frequency exceeds the sum of the damping frequencies of the optical excitations, the system can enter the strong coupling regime. In this regime, there is a periodic transfer of energy between the QE and LSPR. The energy levels associated with the energy transfer become hybridised. This hybridisation results in two new resonances, known as the upper polariton (UP) and lower polariton (LP). Their energies are given by[39]

$$\omega_{UP/LP} = \frac{\omega_{QE} + \omega_{LSPR}}{2} \pm \frac{1}{2}\sqrt{(\omega_{QE} - \omega_{LSPR})^2 + 4\Omega_R^2} \tag{1.23}$$

The energies of the UP and LP levels can be observed by probing the strongly coupled system optically. A key aspect of this hybridisation is that it occurs in the absence of any external field. This has been shown to have a significant effect on the chemical reactivity of molecules coupled to an optical cavity.[40] Such a system can be fabricated by spin coating a PMMA-toluene solution containing photochromic spiropyran (SPI) molecules onto a 35 nm Ag layer on a quartz substrate. The cavity is formed by sputtering another 35 nm Ag layer on top of the PMMA layer.[41] Large Rabi splitting values of up to 700 meV have been observed in such a system.[41] In this case the cavity is coupled to an electronic transition in the molecule. It is also possible to modify reactivity by coupling to a vibrational mode in a molecule. Vibrational coupling was demonstrated by Thomas *et al*.[42] In the work by Thomas *et al*, a Fabry-Pérot optical cavity mode was selectively tuned to the vibrational frequency of either the Si-C or Si-O bond of molecule **R** shown in Figure 1.5(b). The strong coupling of the cavity mode to the vibrational mode of one of the silyl bonds resulted in a reduced rate for the cleavage of this bond, without changing the rate of the cleavage rate of the other bond. This allowed the authors to selectively shift the potential energy curve of the reaction to favour either Product 1 or 2 as shown in Figure 1.5(c).

The previous examples have been concerned with coupling between either an electronic or vibrational mode of a molecule and a resonant Fabry-Pérot cavity *i.e.,* a cavity formed between two mirrors with a tunable gap size. Strong coupling between QDs and microcavities[25,43] was demonstrated many years ago, however theses experiments required liquid helium temperatures. Plasmonic structures offer a novel pathway to achieve room temperature strong coupling of QDs. One of the challenges facing strong coupling to plasmonic cavities was the small mode volumes required. Advanced techniques such as focused ion beam (FIB) milling and EBL have facilitated the fabrication of plasmonic cavities with reduced mode volumes and consequently strong coupling has been observed in a number of QD-plasmonic cavity systems at room temperature.[44–46] Santhosh *et al.,*[46] were the first to realise the strong coupling between a single QD and a plasmonic cavity. In their study, plasmonic cavities were formed by using EBL to fabricate Ag bowtie structures with a gap between the tip of a pair of nanotriangles maintained at $\sim$ 20 nm. An individual CdSe/Zn QD was placed in this gap using capillary forces and room tem-

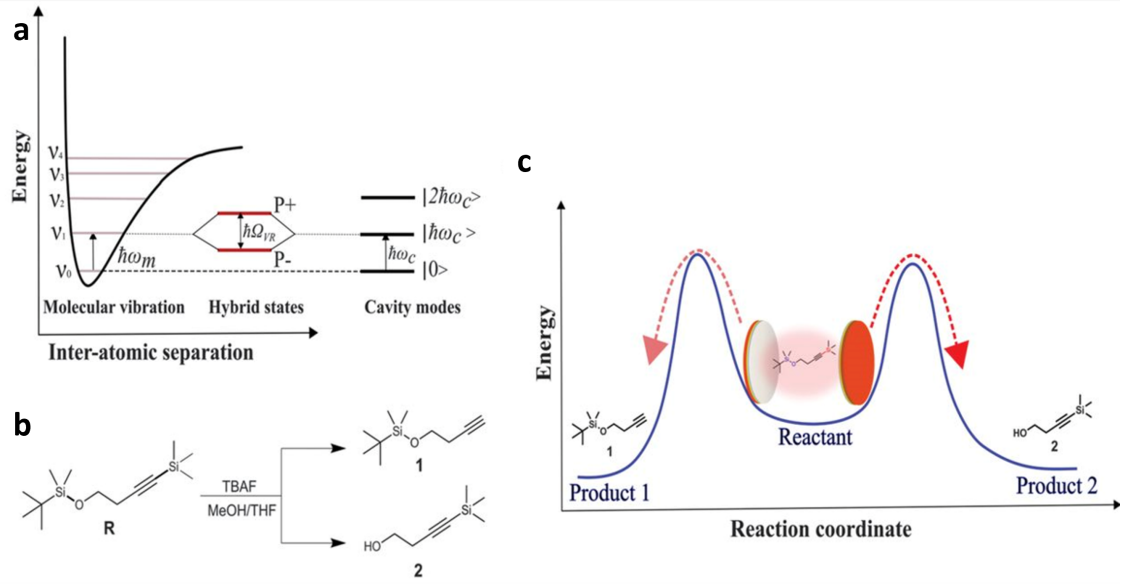

Figure 1.5: (a) Schematic illustration of the light-matter strong coupling of a vibrational transition in resonance with Fabry-Pérot cavity mode and the subsequent formation of hybrid polaritonic states P+ and P– separated by Rabi splitting energy, $\hbar\Omega_R$. (b) The two major silyl cleavage pathways (Si–C scission to form 1, Si–O scission to form 2) for the reaction of R with TBAF in a room-temperature mixture of methanol and THF. (c) Schematic representation of competing site-selective pathways upon VSC of the reactant.[42]

perature Rabi splitting of $\sim$ 200 meV was recorded for and individual QD-bowtie system.

Devices consisting of or featuring strongly coupled QE-LSPR systems could pave the way for a range of quantum optics applications such as single photon emitters,[47] switches,[48] and transistors,[49] as well as applications in quantum information processing[50] and low threshold lasers.[51] While the weak coupling regime has characteristics of irreversible spontaneous emission,[52] strong coupling has characteristics of reversible spontaneous emission.[53] This is the fundamental difference between the two regimes.[54]

1.1.4 Hot Carriers

It can be seen from the presence of the damping term, γ, in Equation 1.13 that the plasma oscillations of the LSPR will decay over time. These losses typically manifest themselves as absorption of the excited fields by the metallic particle supporting the resonance.[55] The simplified band structure of a metal with a Fermi level, E_F, included is

shown in Figure 1.6. There are multiple mechanisms by which a quantum of electromagnetic energy can be absorbed by a metal. For an electron to be excited far above E_F as shown in Figure 1.6(a) it can be seen that there is a large mismatch in momentum between the excited and ground state electron. Therefore a phonon or imperfection in the metal is required, and the absorption results in the generation of a 'hot' pair of carriers *i.e.,* electron and hole, that possess sufficient energy to drive various physicochemical processes. Electron-electron scattering can also lead to absorption, as shown in Figure 1.6(b). In this case however, the same amount of energy is used to generate two pairs of carriers, and therefore the carriers are less energetic than in the previous case. It is also possible for the SPP supported by the metal to assist in absorption via Landau damping, again resulting in a single pair of hot carriers being generated. Finally, it is possible for the photon to be directly absorbed via an interband transition as shown in Figure 1.6(d). It can be seen in this case that the excited electron is very near E_F, and therefore has little energy available to be harvested.

There has been much work done in both developing new plasmonic materials and in improving the quality of current plasmonic materials,[13,55,56] however losses will always be present. As a consequence, focus has shifted towards finding applications for these losses. As already mentioned, the absorption of light into the metallic nanoparticle can excite hot carriers in the metal. Energy transfer from these hot carriers can either occur via indirect transfer of an excited electron in the metal to the LUMO of an adsorbate molecule.[57] Transfer can also occur via direct excitation of the electron from the valence band of the metal to the LUMO of an adsorbate.[58] The energies of these electrons range from the Fermi energy, E_F to $E_F + \hbar\omega_0$, where $\hbar\omega_0$ is the energy of the exciting photon.[55] This corresponds to thousands of degrees Kelvin.[2] However, energy decays from these electron-hole pairs to the lattice on a sub-picosecond time-scale.[58,59] Thus, capturing these so-called 'hot carriers' is a challenging issue. It is possible for these hot carriers to escape the metal, thus transferring their energy to another particle, structure, solution, *etc.* in the locality. The energy distribution of these hot carriers can be measured by performing two-photon photoemission (2PPE) measurements. In these measurements, the first photon excites an electron from an occupied metal state to an unoccupied molecular resonance. The second photon ionises the molecule so that the electron then escapes into

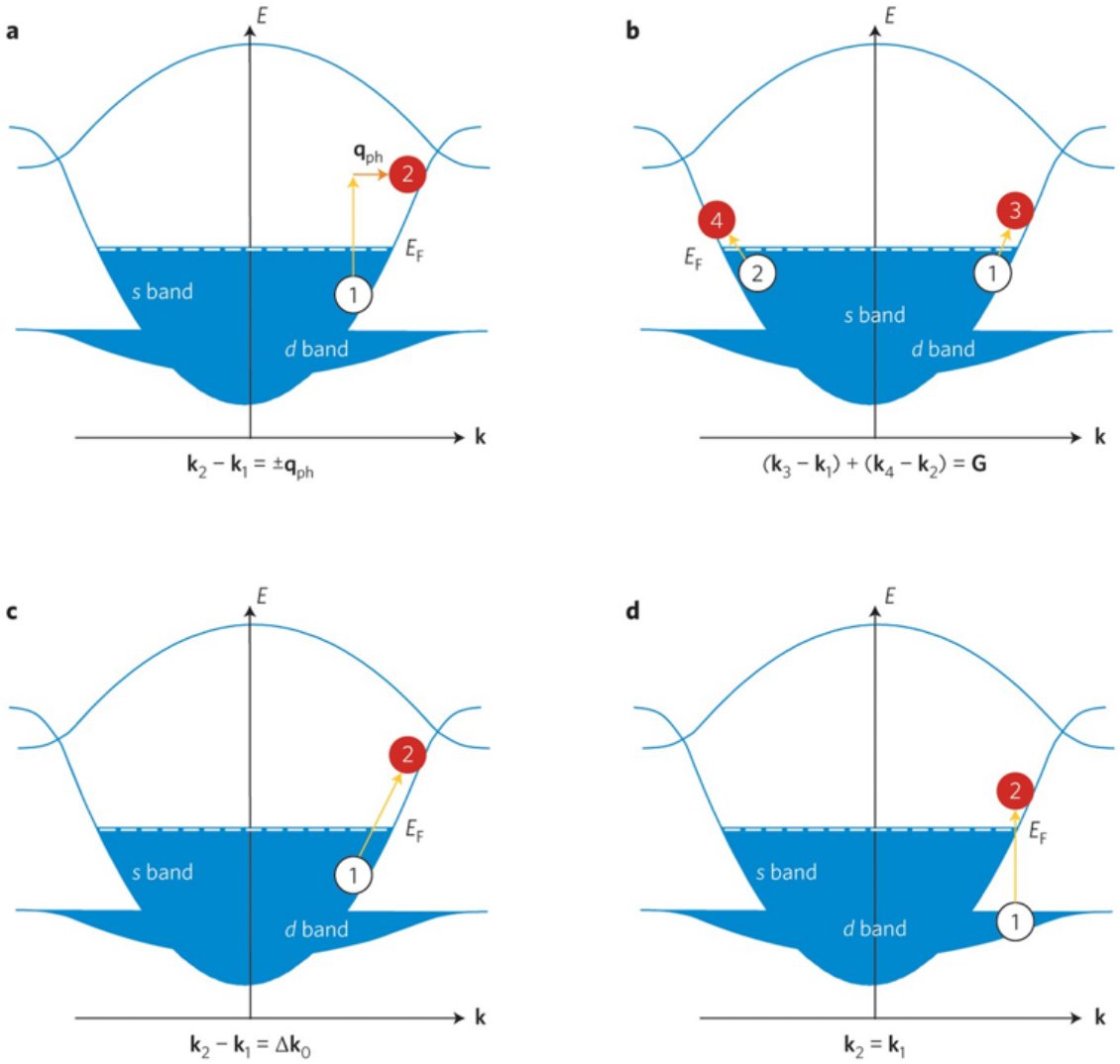

Figure 1.6: (a), Absorption assisted by a phonon with wavevector $\mathbf{q}_{ph}$ creates hot hole (1) with wavevector $\mathbf{k}_1$ and hot electron (2) with wavevector $\mathbf{k}_2$, with energy E_2 above the Fermi level, E_F. (b), Electron–electron scattering assisted absorption, an Umklapp process involving reciprocal lattice vector $\mathbf{G}$ creates four lukewarm carriers, two holes (1,2) and two electrons (3,4). (c), Direct absorption (Landau damping) assisted by the SPP momentum $\Delta\mathbf{k}_0$ creates hot hole (1) and hot electron (2). (d), Interband absorption from the d to s shell does not create hot carriers because hole (1) in the d band has low velocity and excited electron (2) is too close to the Fermi level.[55]

vacuum and can be detected, and information on the energy, momentum, and lifetimes of the electron can be obtained.[60]

As the hot carriers have short lifetimes and decay within $\sim$ 10 nm[61] it is imperative that structures can be fabricated on this length scale. Cortés *et al.*[4] used electron beam lithography to fabricate Ag bowties that were subsequently coated with a 4-nitrothiophenol (4-NTP) monolayer. When these coated antennas are illuminated at their resonant frequency in an acid halide medium, they are reduced to 4-aminothiophenol (4-ATP).[62]

Hot carriers can also be used in conjunction with semiconductors to catalyse photochemical reactions,[63] as well as to improve the performance of photovoltaic devices.[64] The mechanism for the transfer of hot carriers from a plasmonic structure to a semiconductor is shown in Figure 1.7.[5] Electrons near the Fermi level, E_{f}, of the plasmonic metal are excited to surface plasmon states by an incoming photon. The electrons are then transferred to the conduction band of a semiconductor particle. Electrons in this state can then be used to drive redox reactions, water splitting in this case. Electrons that have been injected into a semiconductor in this manner can also add to the photocurrent generated in the semiconductor, improving the performance of photovoltaic devices.[6]

1.1.5 Thermal Losses

Hot carriers generated by LSPRs have short lifetimes on the order of 100 fs - 1 ps.[65] The carriers decay and redistribute their energy to their surroundings as heat via inelastic electron-electron scattering. The heating is confined locally around the nanoparticle, and therefore allows plasmonic nanoparticles to act as nanoscale heat sources with temperatures of up to 220 °C being reported.[8,66]

These thermal losses first found use in the medical field when Pitsillides *et al.*[67] proposed using the localised heating, caused by illuminating gold nanoparticles with a laser, to target and kill cells selectively. Gold NPs are of particular interest in the medical field due to their biocompatibility,[68] and the fact that they can be tuned to be resonant with light in the near-IR region. Biological matter is typically transparent to light in

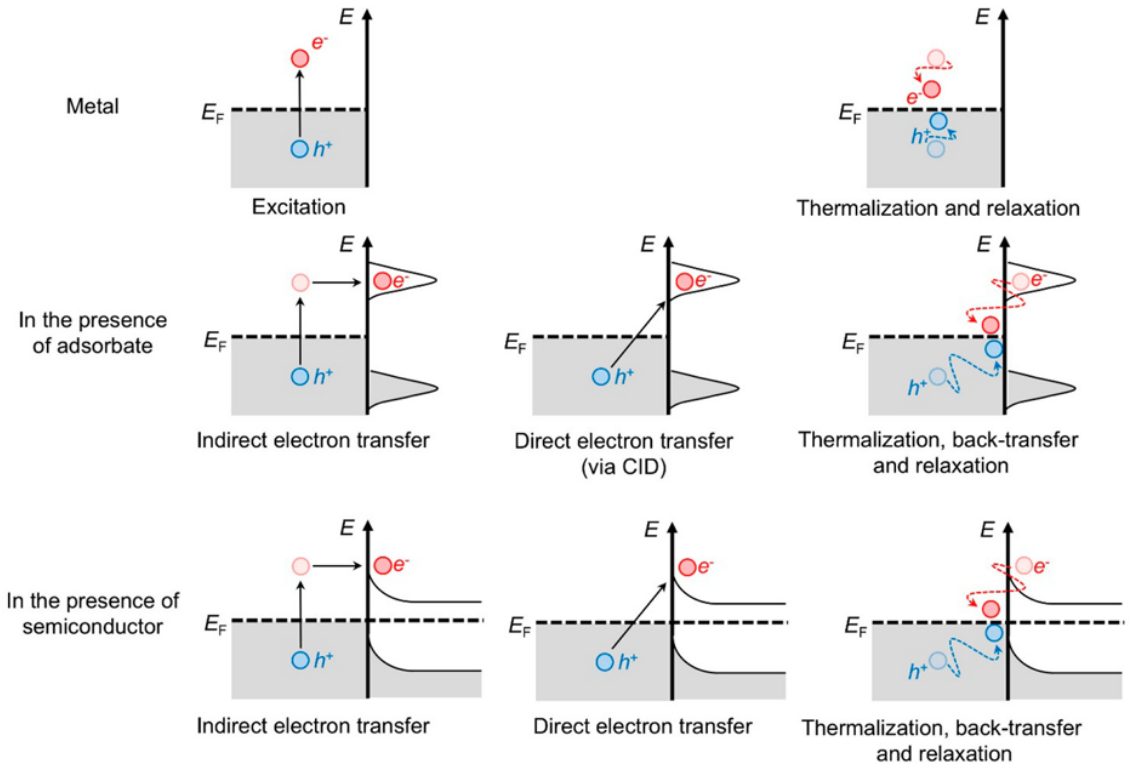

Figure 1.7: Plasmon-induced hot carrier generation and hot electron transfer/back-transfer processes in clean metal, metal/adsorbate, and metal/semiconductor systems. In each case, the left component (relative to energy y-axis) displays the Fermi level (E_F) of plasmonic metals and the right component (relative to energy y-axis) illustrates the highest occupied molecular orbitals (HOMOs) and lowest unoccupied molecular orbitals (LUMOs) for adsorbates, or the CB and VB positions for semiconductors. The gray parts represent the population of electronic states.[5]

this wavelength range, thus allowing for deep penetration. By utilizing optical fibres and endoscopes, most sites in the body can be probed by laser light in this wavelength range.[9]

Cao *et al.*[69] reported the growth of nanowires by passing a precursor gas over Au nanoparticles, and illuminating with a laser resonant with the Au NPs. The absorbed light resulted in the Au catalyst being heated such that the precursor gas could decompose. Heating is localised to the NP surface so the growth of single nanowires is initiated at the particle that is illuminated. This level of control is not achievable by macroscopically heating the particles, *e.g.* with a hot plate.

Heat generated by metal nanoparticles can change their structure. The surface melts at a lower temperature than the bulk, so sharp features will melt more easily. Light induced heating has been used to weld individual metal nanoparticles formed by chemical

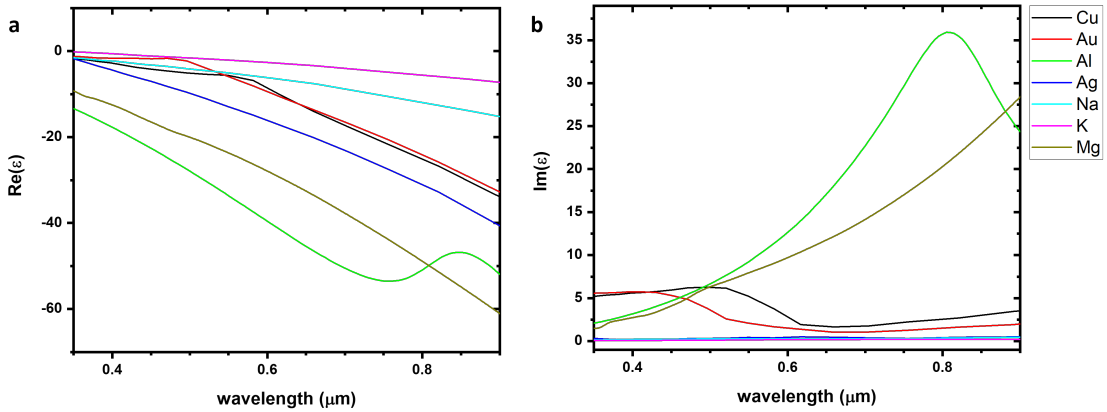

Figure 1.8: The real (a) and complex (b) components of the dielectric function in the visible and NIR region for metals commonly used for plasmonic applications. Data for Ag, Au, and Cu is taken from Johnson and Christy.[72] Data for Al is taken from McPeak *et al.*[73] Data for Na and K is taken from Smith.[74] Data for Mg is taken from Palm *et al.*[75]

synthesis to form chains,[70] and to weld silver nanowires.[71]

1.1.6 Plasmonic Materials

As mentioned in the Section 1.1.1, in order for a nanoparticle to support a LSPR, the particle must have a negative real part of the dielectric function that has a magnitude that is much larger than the imaginary part of the dielectric function. Figure 1.8 shows the real and imaginary parts of the dielectric function for a number of metals commonly used in plasmonics. Quality factors are a figure of merit used to compare the performance of different plasmonic materials. The form of the quality factor varies depending on the application in question. Generally the quality factor is given by the ratio of the resonance frequency, ω_p, to the resonator width, $\Delta\omega_p$, *i.e.,* the full width at half maximum (FWHM) of the plasmon peak.

$$Q_f = \frac{\omega_p}{\Delta\omega_p}. \tag{1.24}$$

The quality factor for a spherical nanoparticle in a homogeneous environment can also be expressed in terms of the real and imaginary parts of the complex dielectric function as:

$$Q_{LSPR} = \frac{-\epsilon'}{\epsilon''} \tag{1.25}$$

Figure 1.9 shows Q_{LSPR} for common plasmonic metals across the visible and NIR part of the spectrum as a function of ω. A log scale is used to highlight the variation in Q_{LSPR} with ω. It can be seen that Q_{LSPR} for Ag is far greater than all other metals for all wavelengths. Consequently Ag is the highest performing plasmonic material with the lowest losses. However, Ag is easily tarnished by S containing molecules in the atmosphere, as well as by oxidation, resulting in severe degradation in its plasmonic properties over time.[76] Au has a high Q_{LSPR} for wavelengths greater than 500 nm. The drop off in Q_{LSPR} below 500 nm is due to interband absorption and is reflected in the increase of ϵ'' in this region seen in Figure 1.8(b). The stability of Au as well as it's high performance above 500 nm make it a popular choice as a plasmonic material. Cu follows a similar trend to Au however under atmospheric conditions elemental Cu is readily oxidised to Cu_2O and CuO, making it less attractive than Au for applications in plasmonics.[13] Al possesses an interband transition near 800 nm. This is represented in Figure 1.8(b) as the sharp rise in ϵ''. However from Figure 1.9 it can be seen that below 550 nm its plasmonic properties surpass those of both Au and Cu, and it even surpasses the properties of Ag as we move into the UV region of the spectrum. These factors, along with the chemical stability of Al and its cost compared to Au and Ag make it a very attractive material for plasmonic applications.[77] Theoretical studies on alkali metals have indicated that Na and K may have plasmonic properties comparable or even superior to Ag, however these metals are highly reactive and these results have not been verified by experiment to our knowledge.[78] Recent work by Ringe *et. al.*[79] has proposed Mg as an alternative plasmonic material. From the values of Q_{LSPR} shown in Figure 1.9 it can be seen that Mg can support LSPRs across the UV, visible and NIR ranges, however Mg NPs faces challenges due to their chemical stability as well as the difficulty in controlling the dimension of the NPs.

Various non-metals such as transition metal nitrides,[80,81] transparent conducting oxides,[80,82] and doped metal oxides[83,84] have also gained attention recently as alternative plasmonic materials. TiN has displayed high carrier concentrations resulting in plasmon frequencies similar to those of Au, and its compatibility with CMOS processes make it an attractive choice as an alternative plasmonic material.[85,86] Unfortunately, optical losses are greater than those of Au for all nitrides.[85] Despite this, the high-temperature

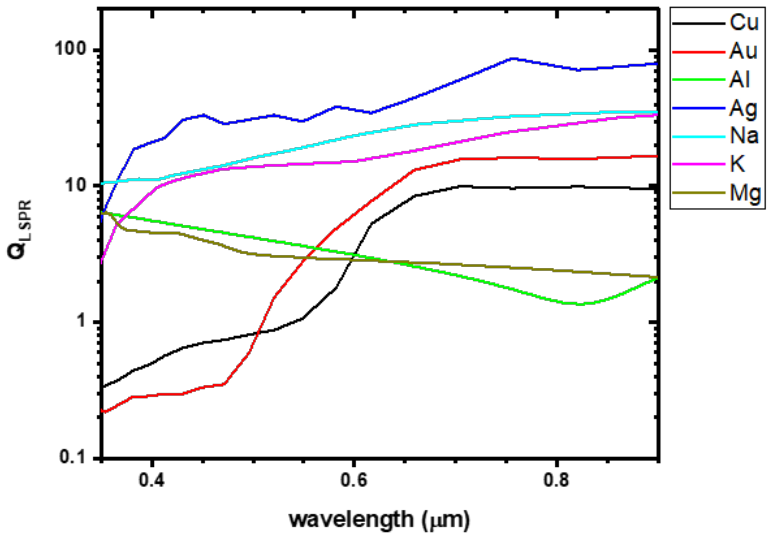

Figure 1.9: Q_{LSPR} for common plasmonic metals as a function of ω. Data for Ag, Au, and Cu is taken from Johnson and Christy.[72] Data for Al is taken from McPeak *et al.*[73] Data for Na and K is taken from Smith.[74] Data for Mg is taken from Palm *et al.*[75]

stability as well the ease of fabrication has led to plasmonic metal nitrides being used in applications such as nanophotonics,[87] photovoltaics,[88] and solar control filtering.[89] Transparent conducting oxides such as Al-doped ZnO (AZO) and Sn-doped In_2O_3 (ITO) have also been investigated as alternative plasmonic materials.[80] While materials such as AZO possess lower losses than even Ag, plasmon resonance occurs at frequencies in the mid and near-IR region of the spectrum, limiting the range of their applications.[80,84] Tungsten bronzes (M_xWO_3) are another family of metal oxides that have recently gained attention.[84] The plasmon frequency of this family is tunable by varying the stoichiometry, x, of the metallic species, M. LSPR frequencies and losses are comparable to those of Au suggesting that the tungsten bronzes could be used as a lower cost alternative to Au. However, plasmonic M_xWO_3 materials are challenging to fabricate, and further research into their chemical stability is required.[84]

1.1.7 Geometric dependence of LSPR

From Mie theory, the extinction cross section, σ_{ext}, of a spherical nanoparticle is given by[14]

$$\sigma_{ext} = \sigma_{abs} + \sigma_{sca}, \tag{1.26}$$

where

$$\sigma_{abs} = \frac{24\pi^2 R^3 \epsilon_1^{3/2}}{\lambda} \frac{\epsilon_2''}{|\epsilon_2 + 2\epsilon_1|^2}, \tag{1.27}$$

and

$$\sigma_{sca} = \frac{32\pi^4 R^6 \epsilon_1^2}{\lambda^4} |\frac{\epsilon_2 - \epsilon_1}{\epsilon_2 + 2\epsilon_1}|^2. \tag{1.28}$$

Here, R is the radius of the nanoparticle, λ is the wavelength of the incident light, and ϵ_1 and ϵ_2 are the complex dielectric functions of the metal and background medium respectively. If we consider the ratio of scattering to absorption we find that

$$\frac{\sigma_{sca}}{\sigma_{abs}} \propto (\frac{R}{\lambda})^3. \tag{1.29}$$

For small nanoparticles when $R << \lambda$ we can see that σ_{sca} becomes negligible and $\sigma_{ext} \approx \sigma_{abs}$. Therefore absorption dominates for small nanoparticles. Up until this point we have used the dipole approximation *i.e.,* each nanoparticle supporting resonance behaves as a dipole with a single positive and negative charge. As the nanoparticle increases in size, ($R > \lambda/20$) the field inside the particle cannot be assumed to be uniformly distributed and multipoles must be considered. Consequently the extinction spectra for the nanoparticle will show evidence of multiple resonances.[90] Mie theory provides the exact analytical solution for spherical and spheroid nanoparticles, however the solution for spheroids is sufficiently complex that they have rarely been used.[14] A number of numerical solutions have been developed to solve for the optical properties of spheroids,[91,92] as well as other more complex geometries.[93]

Kelly *et al.*[14] calculated plasmon resonances for Ag spheroids with a fixed volume, equivalent to a sphere with radius 80 nm, with varying aspect ratio. It was found that as the aspect ratio was increased, the plasmon resonance red shifted. If the polarisation of the incident light was set to be parallel to the minor axis, a second blue shifted resonance occurred. If the particle had a third distinct axis, a third resonance was also observed. The red shift in plasmon resonance due to increasing spheroid length arises because the dipole separation is increased, and consequently the restoring force on the displaced electrons is reduced.[94] Wiley *et al.*[95] used the Discrete Dipole Approximation (DDA) to calculate the plasmon resonance of a wide variety of Ag nanostructures. The authors report that a

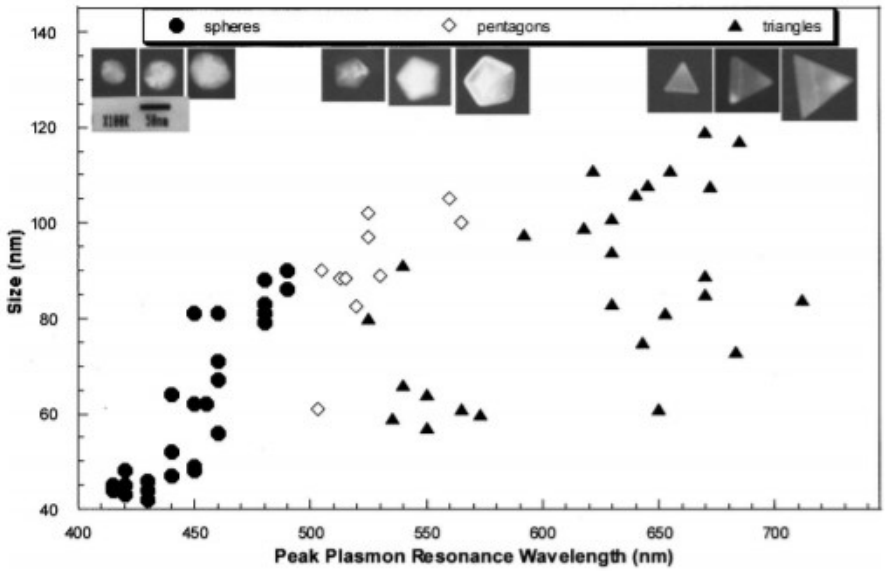

Figure 1.10: Plot of the TEM lateral size vs the spectral peak wavelength for a diverse collection of individual silver nanoparticles[99]

cubic nanostructure displays multiple extinction peaks compared to a spherical structure due to the presence of multiple distinct symmetries in the cubic structure. The shapes that result in the furthest red shift when compared to the spherical particle are those with the sharpest corners. Sharp metallic features on metallic nanostructures are well known to accumulate charge via a non-resonant effect known as the '*lightning-rod effect*'.[96,97] The accumulation of charge in a small region of the metallic nanostructure due to this lightning-rod effect results in further charge separation in the dipole, resulting in a decrease in the restoring force and a subsequent red shift of the resonance frequency.[95] The lightning-rod effect also results in a localised field enhancement that is superimposed on the field enhancement caused by the LSPR,[97] making sharp features desirable on structures designed for applications that utilise near field enhancement.[98]

Modern fabrication techniques allow for a wide variety of geometries to be fabricated on the nanometre scale. The LSPR of a particular structure can be calculated by solving Maxwell's equations. Thus, if a precise LSPR frequency is required for a process, the structure that supports the LSPR can be predicted, and then accurately fabricated. Mock *et al.*[99] provided a systematic study of the effect of shape and size on the plasmon resonances of spherical, pentagonal, and triangular silver nanoparticles. The colloids in solution were prepared by nucleating silver salts onto gold nuclei. Harra *et al.*[100] re-

ported that, for spherical Ag nanoparticles, the surface plasmon resonance was shifted from 398-448 nm as the particle diameter increased from 50-130 nm.

1.2 Nanofabrication Techniques

As mentioned previously, the LSPR frequency of metallic nanoparticles is strongly dependent on the geometry of the nanoparticle. There are a wide variety of methods for fabricating plasmonic nanostructures that can broadly be divided into bottom-up and top-down methods. Bottom-up techniques rely on synthetic chemical techniques to assemble atoms into nanoparticles. Complex geometries such as rods, stars, pentagons *etc.*, are attainable by varying reaction conditions such as temperature, solvent, precursors, and surfactants. The size of these structures can also be precisely controlled, with sizes of $<$10 nm possible with a narrow distribution.[9–11] Chemical techniques are easily scalable, however there is little control over the placement of the nanoparticles. This lack of precision makes building arrays of these nanoparticles a major challenge and thus limits their use in the production of microelectronics. Top-down techniques are based on starting with a bulk material and removing material in a step-by-step process to fabricate nanomaterials. This allows for precise control of the dimensions and on-chip location of the fabricated structures. In this thesis, we focus on the use of electron-beam lithography (EBL) and helium-ion-beam lithography (HIBL) for nanostructure fabrication.

The word lithography has its origin in the Greek words *lithos*, meaning 'stone', and *graphein*, meaning 'to write'.[101] The first lithography process was invented by the German artist Alois Senefelder in 1796 and was based upon the immiscibility of oil and water.[101] In this technique a grease-based ink is used to paint the image onto a black stone or plate. Weak nitric acid and gum arabic is applied to the surface, making the parts of the stone surface not protected by the greasy ink more hydrophilic. An oil-based ink is then applied to the surface, and only sticks to the areas treated with grease *i.e.,* the original image.[102] The stone is then pressed onto a blank sheet to transfer the image to the sheet. The first photolithographic process was developed by Nicéphore Niépce in the 1820s.[103] Niépce dissolved Bitumen of Judea, a naturally occurring asphalt, in lavender

oil and coated it onto a lithographic stone. After the coating dried, a test subject, typically and engraving, was laid over the surface of the stone, and the pair were placed in direct sunlight. After exposure, the solvent could be used to rinse away only the unhardened bitumen that had been shielded from the light by the test subject. The bare parts of the surface could be etched with acid, or the remaining bitumen could be used as the water-repellent material in lithographic printing. It is by this process that Niépce created what is believed to be the world's first photographic image.[103]

Within the US electronics industry in the early 1950s, it was generally accepted that replacing vacuum tubes with transistors would satisfy all need for the shrinking of electronics for both commercial and military applications. Two fields that required further miniaturization of electronics were the manufacture of hearing aids and proximity fuses for mortars. It was James Nall and Jay Lathrop who first incorporated photolithography into the fabrication of circuits, while working on the miniaturization of proximity fuses in 1957.[104,105] In the state-of-the-art at the time the base region of a transistor was a mesa-like structure that protruded from the device. The structures were fabricated by chemically etching Ge. The area that was selected to make up the base region was coated in a wax that protected the region from chemical etching. During etching, the Ge material around the wax was removed, leaving behind a region that resembled a geological mesa. This method of wax coating could not reproducibly achieve the alignment and small sizes that Nall and Lathrop required so they shifted their attention towards the use of a photoresist instead of the wax. By modifying a trinocular microscope, they were able to project a reduced image photographic negative of the required pattern onto a wafer coated with the photoresist. Despite this technically being a photoetching process, Nall and Lathrop chose the term 'photolithography' as they believed it sounded 'higher tech'.[105]

In the early days of industrial photolithography (1970s-1980s) contact and proximity printers were used. In contact lithography the mask is in direct contact with the resist during exposure. This greatly reduced the lifetime of the mask due to degradation by the resist over time. This technique has been used for dimensions between 5 and 10 μm.[106] Proximity printers maintained a gap between the mask and resist, however maintaining the gap size was a challenge as resolution worsened with increasing gap size. Dimen-

sions between 3 and 5 μm could be patterned with proximity printers. Following these methods 1× projection printers were developed. These allowed for the mask to be projected onto the photoresist at large distances so degradation of the mask was not an issue. 1× projection printers have been used for dimensions between 0.7 and 3 μm.[106] In the late 1980s lithography tools using reduced projected images known as 'steppers' were introduced. In previous tools the mask was designed to pattern an entire wafer at a time. The fabrication of masks to expose an entire wafer was becoming more challenging as the complexity of the masks as well as the wafer sizes increased. It was decided that a single mask would pattern a single or a few dies to be printed simultaneously. This allowed the masks to be magnified with a factor of 4 or 5 compared to the image required on the wafer. The masks were kept at a fixed distance above the wafer and then 'stepped' across the wafer to pattern the entire wafer. Steppers have been used to pattern features with sizes from 0.25 to 0.7 μm.[106] Following steppers, step and scan systems, known as 'scanners' were developed.[107] Scanners further reduced the complexity of the optics by only projecting one slit of the mask onto the wafer and scanning the wafer and mask simultaneously to pattern the full image. The mask is then stepped to the next position where a new scan operation could proceed.

1.2.1 Resolution of Photolithography Systems

In 1965 Gordon Moore famously posited that the number of components per individual integrated circuit would double every year until 1975.[108] In 1975 Moore revised this rate of growth, predicting that the number of components would continue to double every year until 1980, after which the rate would slow to a doubling of components every two years.[109] It became a goal of the semiconductor industry to maintain Moore's Law, and remarkably the constant rate of doubling every two years has been upheld into the 2020s.[110] Photolithography has played a huge role in the sustained miniaturization of integrated circuits. The minimum feature size that can be projected onto a wafer is limited by the diffraction limit of light that can pass through the smallest slit of the mask.

An Airy disk is the diffraction-limited spot formed using a perfect lens and a circular aperture. Ernst Karl Abbe recognised that images of samples viewed through a micro-

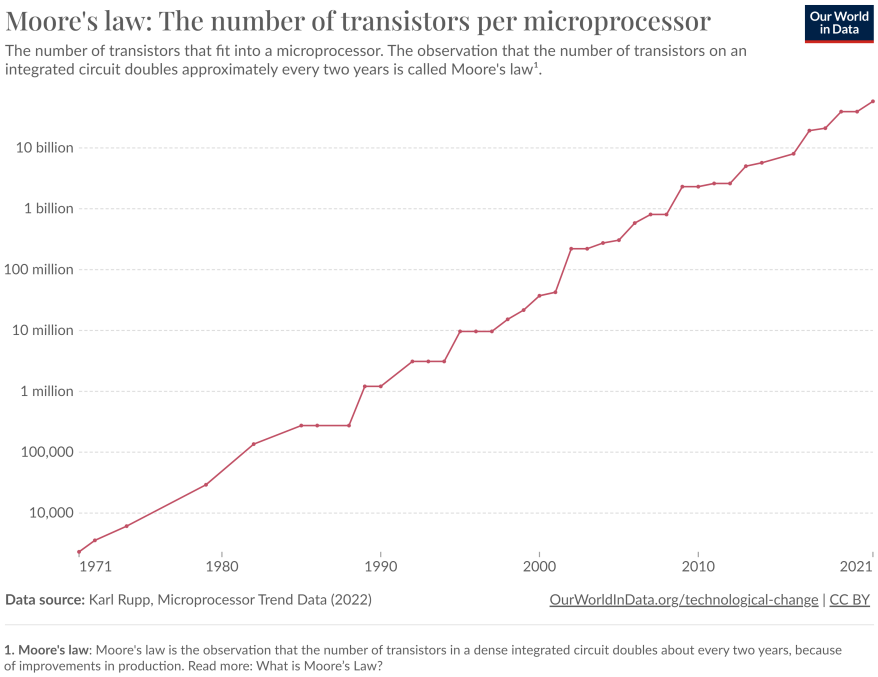

Figure 1.11: Moore's Law: A plot of the number of transistors on microchips as a function of year.[110]

scope are composed of overlapping Airy discs. He defined the diffraction limit, and thus the resolution of an imaging system as[111,112]

$$d = \frac{\lambda}{2NA}, \tag{1.30}$$

where λ is the wavelength of light and NA is the numerical aperture $= nsin\theta$, where n is the refractive index of the medium and θ is half the angular aperture of the objective lens. Lord Rayleigh expanded on the work of both Airy and Abbe and invented the theory of the 'Rayleigh criterion'.[112,113] He determined that when the diffraction pattern from two separate Airy disks do not overlap, they are well resolved and satisfy the Rayleigh criterion. When the centre of one Airy disk is directly overlapped by the first minimum of the diffraction pattern of another, they are considered to be 'just resolved' and still distinguishable from one another.[112,113] If the disks are closer than this, they do not satisfy the Rayleigh criterion, and thus are not resolved as two distinct points of light. The formula for the Rayleigh criterion is a slightly refined form of Abbe's formula and is

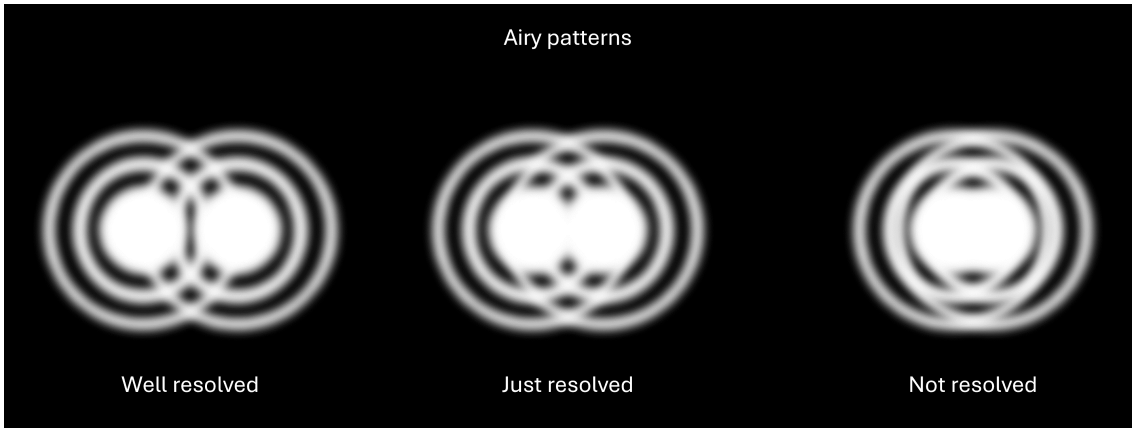

Figure 1.12: Airy diffraction patterns from two point sources of light. Points far apart (left) and meeting the Rayleigh criterion (middle) can be distinguished from each other. Points closer than the Rayleigh criterion (right) are difficult to distinguish.

given by

$$R = \frac{1.22\lambda}{NA_{obj} + NA_{cond}}, \tag{1.31}$$

where NA_{obj} and NA_{cond} are the numerical apertures for the objective and condenser lenses respectively.[112,113] The factor of 1.22 comes from Rayleigh's work on Bessel functions. It can be seen from these equations that in order to reduce the diffraction limit of an imaging system either the wavelength of imaging light can be reduced, or the *NA* can be increased. The *NA* can be increased by using a higher index medium such as oil for imaging. Consider a system with an oil-immersion objective with an *NA* of 1.45 and a condenser with an *NA* of 0.95. If light with a wavelength of 400 nm is used, from the Rayleigh criterion, the maximum resolution of the system is 203 nm. The critical dimension, *CD*, that can be printed by an optical lithography system is derived from the Rayleigh criterion and given by

$$CD = k_1 \cdot \frac{\lambda}{NA}, \tag{1.32}$$

where k_1 is a coefficient that accounts for factors related to the manufacturing process. The physical limit is $k_1 = 0.25$,[114] therefore for a system with $NA = 1$ features with sizes a quarter of the wavelength of the light used should be achievable.

Historically, the reduction of the wavelength of the light used for exposure has driven the decrease in the smallest feature size achievable by photolithography. Initially UV

light from gas-discharge lamps using Hg were used for photolithography. These lamps produce a broad spectrum, which was filtered to select a single spectral line for exposure.[115] These lamps were used until the 1980s, however the industry's need for higher resolution and higher throughput led to the development of new light sources. In 1982 excimer laser lithography was proposed and demonstrated.[116] Excimer lasers typically use a combination of a noble gas and a reactive gas. Noble gases are typically inert, however under certain conditions of high pressure and electrical stimulation these molecules can exist in an excited state and form temporary compounds. These compounds release their excess energy via spontaneous emission, and it is by this action that excimer lasers could be used as light sources.[117] Commonly used excimer lasers in photolithography include KrF, which has a wavelength of 248 nm, and ArF, which has a wavelength of 193 nm. Photolithography using excimer lasers has been used to produce features with sizes below 50 nm.[118]

The latest development in photolithography sources has been the advent of extreme ultraviolet (EUV) sources. Laser-driven light sources have been developed that produce 13.5 nm light, paving the way for the fabrication of features with sizes down to 10 nm.[119] The challenge that faces EUV is the high energy of the light rather than diffraction of the light. All materials absorb EUV meaning that only reflective optics can be used. For 13.5 nm radiation, EUV uses mirrors consisting of 6.79 nm Mo/Si bilayers. As the performance of the mirror is strongly dependent on this bilayer thickness, the tolerance for defects and roughness in the reflecting optics is extremely low. Furthermore, the entire optical path must be contained under vacuum due to absorption of the EUV light by air.[120] The absorption of EUV light by the photoresist can result in the excitation of secondary electrons within the resist. These secondary electrons can possess enough energy to expose the resist, reducing the resolution of the process. This effect is known as secondary electron blur and is a further challenge facing EUV lithography.[121]

1.2.2 Scanning Probe Lithography

Scanning probe lithography (SPL) is a nanofabrication technique that involves the use of a sharp scanning probe to produce local modifications on a surface.[122] This technique

has been used to manipulate single atoms and create atomic scale patterns,[123] however this requires cooling to liquid helium temperatures, as well as ultra-high-vacuum conditions, thus limiting the suitability of SPL for high-throughput nanofabrication processes. Nevertheless, recent advances have been made to develop SPL techniques operational at ambient conditions with a higher throughput.[122,124] Dip-pen nanolithography (DPN) uses the tip as a pen to first absorb 'ink' molecules. The tip is then operated in contact mode and the water layer capillary forces are used to transfer the molecules from the tip to the surface of the sample.[125] Low-energy field-emission SPL is a technique that applies a high voltage to the tip, leading to electron emission from the tip. These electrons can then interact with the sample to induce fracturing or cross-linking similar to the photolithography process.[126] Thermal SPL involves heating the tip to locally heat a liquid resin, inducing a phase change. This phase change allows for three-dimensional structures to be written using SPL.[127] SPL techniques have been used to pattern features with a resolution of 10 nm however the throughput remains too low to be used in industrial nanofabrication processes.[122]

1.2.3 Electron Beam Systems

As previously mentioned, the resolution of an optical microscope is limited by diffraction. This led to the idea that the diffraction-limited resolution of optical microscopy could be broken by using a beam of charged particles such as electrons or ions as the imaging probe, rather than photons. The de Broglie wavelength of 10 keV electron is 0.01 nm, far below the diffraction limit of visible light. As electrons can easily be accelerated to energies of hundreds of keV, they were an ideal candidate for a new type of imaging system. In 1926, with the publication of Hans Busch's theory of the first electromagnetic lens capable of focusing charged particles, the idea of a microscope using electrons to image a sample instead of photons became a possibility. In 1931 the first transmission electron microscope (TEM) was invented.[128] As the name would suggest, this technique forms an image from the electrons that have passed through the sample. The first scanning electron microscope (SEM) was proposed by Manfred von Ardenne in 1938.[129] Here, the electron beam is focused into a fine probe, and then rastered across the

sample. The interaction of the electron beam with the sample results in the generation of electrons by the sample. These electrons are known as secondary electrons (SEs) and they are collected and counted by a detector placed inside the microscope. A greyscale image is formed by counting the number of SEs generated at each point in the image scan.

In his famous 'There's Plenty of Room at the Bottom' talk in 1959 Richard Feynman proposed that the entire Encyclopaedia Britannica could be written on the head of a pin by reversing the lenses on an electron microscope to demagnify the beam into a fine probe. This probe could subsequently be used to write by depositing material directly onto a surface.[130] He also predicted that directly writing on the surface of a metal may not work and proposed a yet to be realised electron beam resist.[130] In the early 1960s electron beam systems were first used to deposit silicone and hydrocarbon material.[131,132] In 1967 Larkin and Matta fabricated a planar bipolar transistor with an emitter contact with a reduced size of 1 μm^2 by using an electron beam to expose the resist material, in a process that resembles electron-beam lithography (EBL) methods used today.[133] In this work, a SEM was modified by attaching a pattern generator to allow the beam to scan in specific patterns. The advent of laser interferometer stages allowed for larger wafer sizes to be processed with EBL, improving the throughput of the method.[134] By the 1980s dedicated EBL systems were being produced with systems capable or writing 25 nm structures across an 80 μm field. These systems also possessed accurate field stitching allowing for large patterns to be fabricated.[135] In recent years EBL has been used to fabricate features with sub-10-nm dimensions,[136,137] however the throughput of this method remains a limiting factor for EBL.

Electron guns can generate electron beams via either thermionic emission or field emission. Thermionic emission, involves the heating of a filament (tungsten or LaB_6) such that the electrons in the filament gain sufficient energy to overcome the work function and are emitted into the vacuum.[138,139] During field emission, a strong electric field is applied to the tip of the gun. The application of the field allows electrons to be emitted via tunnelling through the tip, or by reducing the work function for electrons to escape the tip, known as the Schottky effect.[138,140,141] Guns using the tunnelling effect do not

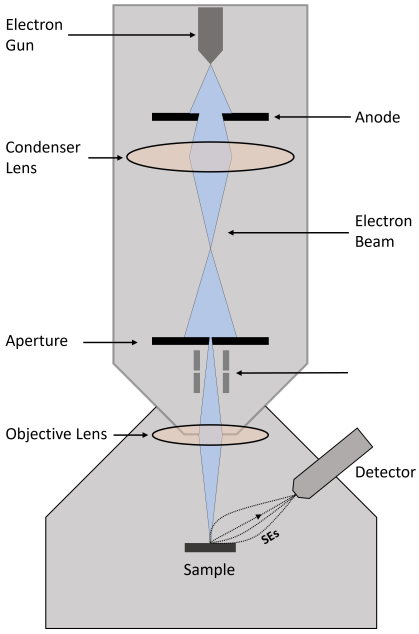

Figure 1.13: Schematic of a standard scanning electron microscope (SEM). The electron beam is generated by emission of electrons by the electron gun. The electrons are accelerated down the column by the anode, and focused by the condenser lens. The beam is passed through an aperture to reduce aberrations in the beam as well as overall beam current. The objective lens focuses the beam onto the sample. SEs generated by the interaction of the beam with the sample are collected by the detector for image formation.

heat the source at all and thus are known as cold FE guns. Cold FE guns are superior to Schottky FE guns with respect to brightness, source size, and energy spread, however Schottky guns can emit a higher and more stable current, making them superior for applications such as EDX, EBSD etc. Both types of field emission guns (FEGs) have very high brightness i.e., current emitted per unit area per solid angle, while also having a source size below 10 nm and energy spread of less than 1 eV. The emitted electrons are accelerated down the column by the anode. The condenser lens focuses the electrons to form the initial beam. The aperture is used to limit the beam current, as well as to help reduce aberrations in the beam. The scanning coils are used to deflect the beam so that it can be rastered over the sample. The objective lens focuses the beam on the sample.

Figure 1.14 depicts the interaction volume of an incident electron beam with a sample, as well as the various signals produced by this interaction. The signal that is typically of primary interest to researchers is the secondary electron (SE) signal. The incident electron beam can ionise atoms in the sample, and the loosely bound electrons produced by

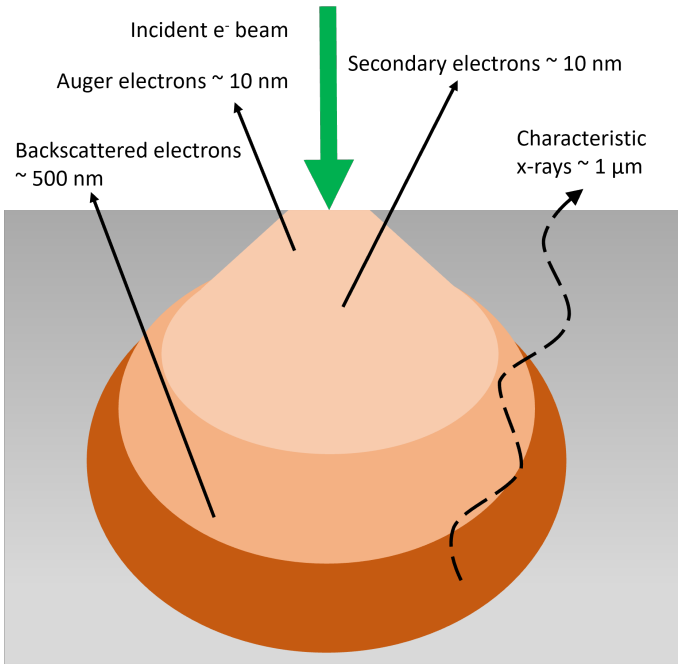

Figure 1.14: Illustration of the interaction volume of a beam of electrons with the surface of a sample as well as the different types of signals produced by the incident electrons. The lengths in the figure represent the escape depth of the corresponding signal.

this interaction can escape from the surface of the sample. These SEs have low energies of around 3-5 eV[138] and therefore can only escape from a region near the surface of the specimen, and provide topographic information with good resolution. The emitted SEs can easily be collected by a detector carrying an applied bias. The most commonly used SE detector is the Everhart-Thornley (ET) detector.[142] This detector consists of of a scintillator within a Faraday cage. A low positive voltage is applied to the Faraday cage to collect only the low energy SEs in the chamber. The scintillator has a high positive voltage to convert the collected SEs to photons. A photomultiplier tube converts the photons back to an electrical signal, which is then output as brightness modulation on the display screen of the SEM.[138] It is also possible that incident electrons can be scattered elastically by the sample *i.e.,* with negligible energy loss. These elastic collisions between electrons and the nuclei of atoms within the sample can result in the back-scattering of these electrons towards their source, hence they are known as back-scattered electrons (BSEs). The rate at which electrons are back-scattered is related to the atomic number of the atom involved in the collision with the electron. Collisions with heavier nuclei are more likely to produce BSEs, therefore images formed using BSEs have much better

contrast between different elements in a sample.[138,143]

The incident beam can excite a core electron in an atom in the surface. This excited atom can relax either via the emission of an electron or by the emission of an x-ray photon.[144] The electrons that are emitted are known as Auger electrons and have low energies. Because of their low energies, Auger electrons can only escape from a distance a few nanometres and thus they are principally used for surface analysis.[138] X-rays can escape from much deeper within the sample ($\sim$ 1 μm). As these x-rays are the result of an electron transition, different elements can only release characteristic x-rays with specific energies. Consequently, the collection of these x-rays can be used to perform elemental analysis of the sample. These x-rays are the basis of energy dispersive x-ray spectroscopy (EDX).[145]

1.2.4 Helium Ion Beam Systems

The helium ion microscope (HIM) is a modified version of a field ion microscope (FIM) developed by Erwin Müller over 50 years ago.[146,147] The operation of such a tool involves a sharp tip, that is biased at a positive voltage with reference to an extraction electrode. The tip is cryogenically cooled, and an imaging gas is administered near the tip. At the very edge of the tip the field strength is high enough to cause field ionisation of the imaging gas, which then can be accelerated away from the tip by the extractor. Ions are an attractive imaging probe as their large masses mean that they will have a much shorter de Broglie wavelength than electrons with equivalent energy. This would allow for ions to be focused to a smaller probe size than electrons as the probe size in a SEM is fundamentally limited by diffraction.[147] Furthermore, the interaction volume of ions is much smaller than for electrons. This means that SEs generated by the interaction of the ion beam with the sample should originate from an area nearer to the point of incidence of the beam, resulting in improved resolution of the system.[147]

A FIM using He as the imaging gas is a relatively modern development, thanks to the development of a stable, high-brightness He^+ source.[147,148] The HIM source consists of a sharp tungsten needle with a roughly parabolic cross-section and a pyramidal structure at

the tip. Typically at the apex of this faceted pyramid a stable configuration of three close-packed atoms can assemble, known as a 'trimer'.[149] Atomic He gas is ionised by the tip to form He^+ ions. As the fixed total He supply is now shared between the three atoms in the trimer, the emission of ions per atom is greatly increased compared to an unsharpened, spherical tip.[148] One of these atoms is selected to produce the beam for image formation by placing apertures in the beam path and by aligning the optic axis to a specific atom. The emission from the other two atoms is directed to a beam dump.[148,150] The negatively charged extractor accelerates the ions down the column, where they are focused by electrostatic lenses. When the He^+ ions interact with the sample, SEs are formed similarly to SEM, however He^+ ions do not scatter as much as electrons due to their larger mass. Consequently, SEs are emitted from a narrow region around the beam.[147] In a SEM, incident electrons are scattered further away from the point of incidence before producing SEs. These SEs can also have sufficient energy to produce further SEs, known as secondary secondary electrons or SE2s. Consequently, the region from which the SEs that form the image in a SEM originate is much larger than that for HIM. The escape depth of electrons from the surface of a solid is material dependent, but is typically on the order of a few nm.[147] This shallow escape depth, as well as the lower spread of scattered He^+ ions in the sample lead to HIM having a much greater surface sensitivity than SEM.

Another advantage of HIM is the ability to image electrically insulating samples. Imaging with electrons is typically limited to samples that can conduct charge. The reason for this is that if an electron beam is focused on a small region, and the sample is non-conducting, there will be a build up of charge at the surface. This build up of negative charge can deflect the incident electron beam, causing distortion of the image. There are various methods to help to reduce this charging effect. Coating the sample in a thin layer of Au or some other conductive material can make the sample conductive, however there will be a loss in some of the surface detail due to the coating. Operating the SEM at low voltages reduces charging by altering the SE yield such that it can approach unity. By operating the SEM at a voltage where the incident dose of electrons is equivalent to the SE yield, the incoming and outgoing charge to the sample is balanced, reducing the effects of charging. Charging can also be mitigated by using an environmental SEM (ESEM). An ESEM is a type of SEM that operates with a gaseous environment in the

sample chamber. This gas can help to dissipate the charge built up on a non-conducting sample.[151] A drawback to ESEM is that collisions of electrons with the gas in the chamber reduces the signal-to-noise ratio of the image produced.[151] In a HIM, charge accumulates at the surface of the sample in the same manner as in a SEM. A key difference is that He^+ ions are positively charged. This positive charge can be neutralised by use of an electron flood gun inside the chamber, allowing for high resolution imaging of non-conductive samples in the HIM.[152,153]

1.2.5 Electron and He^+ Ion Beam Lithography

A schematic showing a typical electron (EBL) or helium ion beam lithography (HIBL) process is shown in Figure 1.16. First, a suitable substrate is chosen. Substrates are typically conductive materials such as Si to avoid accumulation of charge on the surface, which can result in the deflection of the beam during exposure and distortion of target patterns. However, removable conductive polymer coatings are available that can dissipate the charge building up on the surface, allowing non-conducting substrates to be patterned. The substrate is cleaned and then coated with a beam sensitive material, known as a resist. Resists are typically organic or inorganic polymers. During electron or ion-beam exposure, bonds in the polymer are broken, leading to fragmentation into small molecular weight fragments (positive-tone resist) or leading to cross-linking of fragments into extended networks (negative-tone resist). The solubility of the exposed regions is altered upon exposure such that those regions become more (positive-tone) or less (negative-tone) soluble in an appropriate solvent. Thus, patterns can be 'drawn' in the resist by using a focused beam of electrons or ions. Figure 1.16 depicts a positive-tone resist process. During the metallization step, metal is evaporated across the full surface of the substrate. The final step is the removal of the remaining resist using a suitable solvent. This is known as lift-off. The result for a positive-tone process is metal remaining in only the region that was exposed during the exposure step. The inverse is true for a negative-tone process *i.e.,* gaps in the metal surface are left in the regions that were exposed by the beam.

The feature size that can be created is limited by a range of factors such as beam

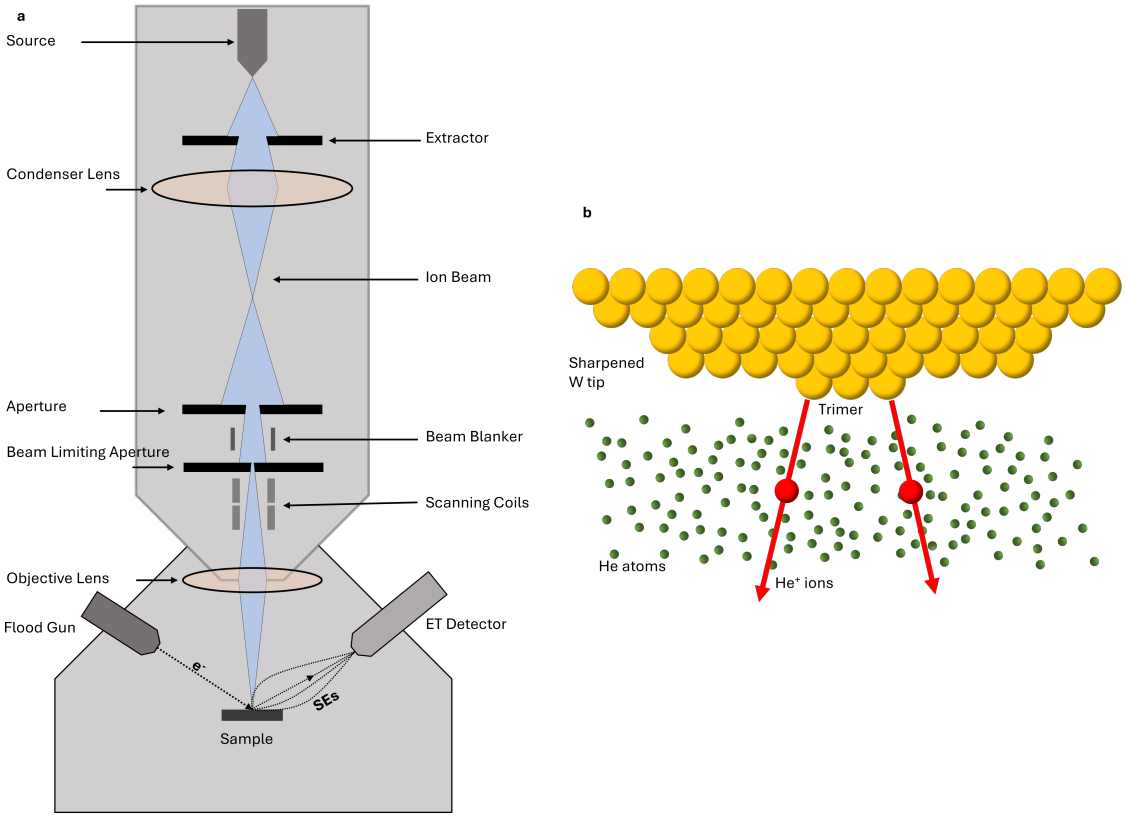

Figure 1.15: (a) Schematic of a helium ion microscope (HIM). He^+ ions are generated at the source and accelerated down through the column by the extractor. The condenser lens focuses the beam, which is then passed through an aperture to reduce aberrations as well as overall beam current. Scanning coils allow for the beam to be rastered across the sample. The objective lens focuses the He^+ beam onto the sample. SEs generated by interaction of the beam with the sample are collected by the detector for image formation. An electron flood gun can be used to balance the build up of positive charge on a non-conducting sample. (b) Schematic of the HIM tip. The tungsten tip is sharpened to an atomically sharp tip, usually consisting of three atoms, known as a trimer. He gas is flowed across the tip. The high field strength caused by the atomically sharp tip is sufficient to ionise the He gas. The He^+ ions can subsequently be accelerated away from the tip.

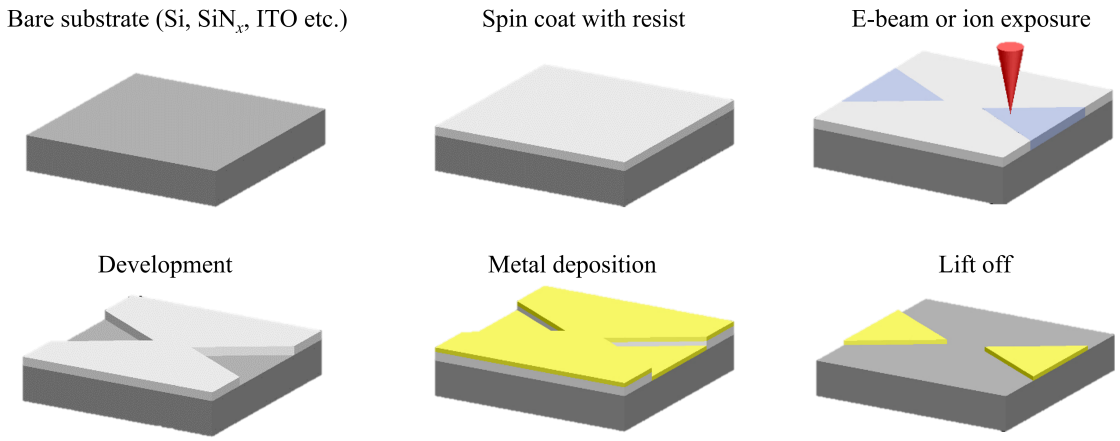

Figure 1.16: Schematic of a positive-tone EBL or HIBL process. A bare substrate is cleaned and then spin coated with the desired resist material. An e^- or He^+ ion beam is then scanned across the desired regions of the resist. During development, the exposed resist is removed using a suitable solvent. Metal is deposited over the entire sample. During lift off, the remaining resist material is removed using a suitable solvent, leaving metal only in the regions exposed by the beam.

diameter, beam current, resist sensitivity, scattering of the electrons or ions within the resist, and minimum pixel size, as well as drift of the stage and the beam. The beam current is the number of electrons passing through the beam spot per second. High beam currents mean faster exposure times, however the maximum beam current is limited by the timing control of the lithography system *i.e.,* the resist will be over exposed before the beam can be deflected away from the sample. High beam currents can also affect resolution due to charging effects in the resist. Low beam currents mean longer exposure times, however this can allow for greater control of the dose. The sensitivity of the resist indicates the amount of energy the resist needs to be exposed to for scission or cross-linking to occur. It is typically reported in units of C/cm^2. The energy of the beam per unit area is known as the area dose and it can be calculated from:

$$\frac{(Beam\ current) * (Area\ dwell\ time)}{(Area\ step\ size,\ U * V)}$$

where U and V are the step size in the X and Y directions respectively. If the resist is exposed to too low of a dose, cross-linking or scission will not occur. If too high a dose is used, unwanted exposure of the region surrounding the desired exposure area can occur.

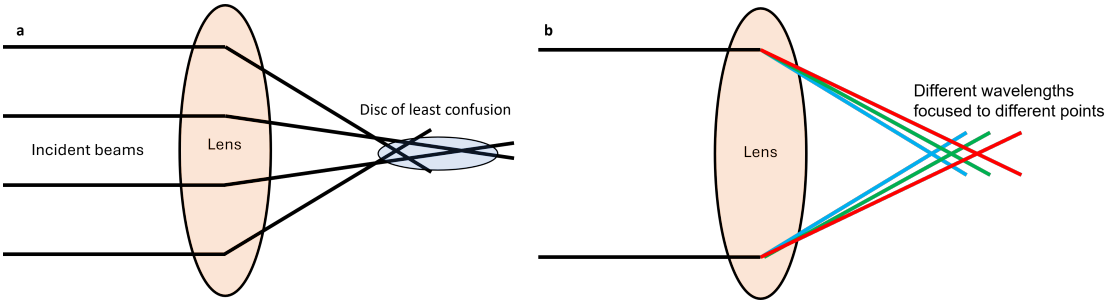

Figure 1.17: (a) Schematic of spherical aberrations in a lens system. Due to imperfections in the lens, rays that are focused by the outer part of the lens are focused to a different plane than rays that pass through nearer the centre of the lens. (b) Chromatic aberrations in a lens system. The incident beam consists of electrons or photons with a distribution of energies. Electrons and photons with different wavelengths are focused to different planes.

1.2.6 Beam Diameter and Aberrations

The beam diameter is the spot size of the focused beam. As mentioned previously, the de Broglie wavelength for 15 keV electrons is on the order of tens of picometres. The larger mass of He^+ ions means they have a much lower velocity than equivalent energy electrons, and therefore have de Broglie wavelengths on the order of tens of femtometres. However, the minimum beam diameter is limited by spherical and chromatic aberrations of the lenses as well as diffraction. Spherical aberrations occur because the beam has a finite width, so the outer rays will be focused to a plane nearer to the lens than the inner rays in an electron lens.[154] The contribution of spherical aberration to the beam diameter is given by

$$d_{sph} = \frac{1}{2} C_{sph} \alpha^3, \tag{1.33}$$

where C_{sph} is the spherical aberration coefficient, and α is the maximum convergence angle for any ray travelling through the lens.[155] Chromatic aberrations occur because there is a distribution of electron energies and velocities within the beam. Electrons of different energies are deflected to different extents by the magnetic focusing lenses, as the Lorentz force experienced by an electron is dependent on the velocity of the electron.[156,157] The contribution of chromatic aberrations are given by

$$d_{chr} = C_{chr} \cdot \alpha \frac{\Delta E}{E_0}, \tag{1.34}$$

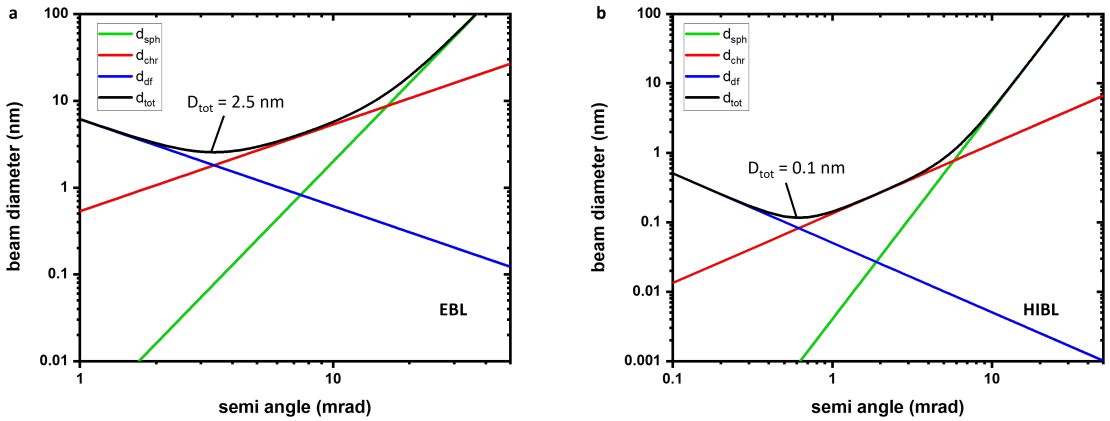

Figure 1.18: A plot of beam diameter vs semi angle in (a) SEM under operating conditions for an EBL process and (b) HIM under operating conditions for a HIBL process. (a) C_{sph} = 4 mm, C_{chr} = 4 mm, ΔE = 1 eV, E_0 = 15 keV. (b)C_{sph} = 8 mm, C_{chr} = 8 mm, ΔE = 0.25 eV, E_0 = 30 keV.

where C_{chr} is the chromatic aberration coefficient, E_0 is the energy of the beam, and ΔE is the energy spread of the beam. The contribution of diffraction to the beam diameter is given by

$$d_{df} = 0.61\frac{\lambda}{\alpha}. \tag{1.35}$$

Summing these terms in quadrature yields an approximation of the minimum beam diameter as a function of α. The spherical and chromatic aberration coefficients, C_{sph} and C_{chr}, are usually assumed to be equal to the focal length of the microscope and are therefore given by the working distance of the microscope (4 mm for EBL and 8 mm for HIBL). The energy spread, ΔE, is typically on the order of 1 eV for SEM and 0.25-0.5 eV for HIM.[155,158] It can be seen from Figure 1.18(a) that the minimum beam diameter in for a SEM operating at a working distance of 4 mm and accelerating voltage of 15 keV is approximately 2.5 nm. The advent of aberration-corrected tools has allowed beam diameters below 1 nm to be realised in modern scanning transmission electron microscopes.[159] For a HIM operating at a working distance of 8 mm and accelerating voltage of 30 keV the minimum beam diameter is approximately 0.1 nm. In reality the beam diameter of a HIM has been measured as approximately 0.25 nm.[147]

1.2.7 Proximity Effect

Proximity effect is the name given to the unwanted exposure of resist between intentionally exposed features because the features have been patterned too close to each other.[160] In an ideal imaging system, there would be no scattering of the incident beam. Consequently, the minimum feature size achievable by the lithographic technique would be equal to the diameter of the beam. In practice, however, electrons and ions are scattered as they penetrate a surface. The scattered electrons and ions can produce SEs some distance away from the point of incidence of the beam. These SEs can be further scattered by the resist, so the area that experiences some dose from a single point exposure from the beam is significantly larger than the diameter of the beam. The dose required for exposure of the resist to occur is known as the dose to clear. The radial spread of dose in a resist means that resist farther from the point of exposure will experience some dose, but not enough to cause exposure. If two separate features are patterned too close to one another these residual doses can sum together to reach the dose required for exposure. This can lead to the unwanted exposure of the region between the two features. This is known as the proximity effect, and it is of particular concern when patterning dense arrays of features. This can result in the interaction and thus exposure of the resist at a significant distance away from the point on the resist at which the direct exposure occurs. A point-spread function (PSF) measures the response of an imaging system to a single point of exposing radiation *i.e.,* it measures the radial spread of energy deposited in a resist by a point exposure from an incident beam. Local dose modification can be used to achieve proximity effect correction, however, to do this an accurate model of the PSF for a beam-resist system is required. One of the main advantages of using HIBL over EBL is the reduced proximity effect for HIBL, owing to the reduced scattering of the incident He^+ ions compared to electrons.[149,161]

1.2.8 Resists

Resists are typically made up of long chain polymer materials and can be divided into positive-tone and negative-tone resists. In positive-tone resists, lithographic action

is achieved when resist exposure leads to scission of bonds along the backbone of the polymer chain resulting in lower molecular weight species in regions where the resist has been exposed to the incident particle beam. The lower weight material can be removed using a suitable solvent, leaving only the unexposed material. Pattern transfer can be performed via either an additive or subtractive process. In an additive process, a metal, or other material, can be deposited on the resist. The remaining resist can be removed in a lift-off process that leaves metal only on the substrate in the region where the resist was exposed. In a subtractive process, the portion of the substrate left bare after the EBL process can be removed via techniques such as reactive-ion etching. In this case the remaining resist also acts as a protective layer for the substrate it coats, and therefore etch-resistance is often an important consideration for electron beam resists.

A negative-tone resist exposure to the beam results in the cross-linking of smaller resist fragments, so the exposed region has a higher molecular weight than the unexposed region. The unexposed resist can be removed leaving only the higher weight material. For pattern transfer, metal can be deposited on the sample, and the remaining negative-tone resist can subsequently be removed. This leaves behind holes in the metal only in region exposed by the beam.

1.2.8.1 Resist Sensitivity

Resists that require a lower dose for lithographic exposure to occur are said to have a higher sensitivity. Higher sensitivities are desired because lower doses lead to lower exposure times, which results in faster processing times overall. However, if the resist is too sensitive, problems with shot noise can occur. Shot noise refers to when intrinsic fluctuations in the beam current have a noticeable effect on the yield of features exposed by the beam. When trying to pattern the smallest possible features, the lowest possible doses are required. This can be a particular problem for HIBL as He^+ ions are much more efficient at exposing resists than electrons. Small feature sizes can potentially only require tens of ions to result in lithographic exposure of the resist. Doses this low would be on the same order of magnitude as the noise of the beam, meaning that there could be a large inconsistency in the feature sizes achieved *i.e.,* yield, at a low dose.

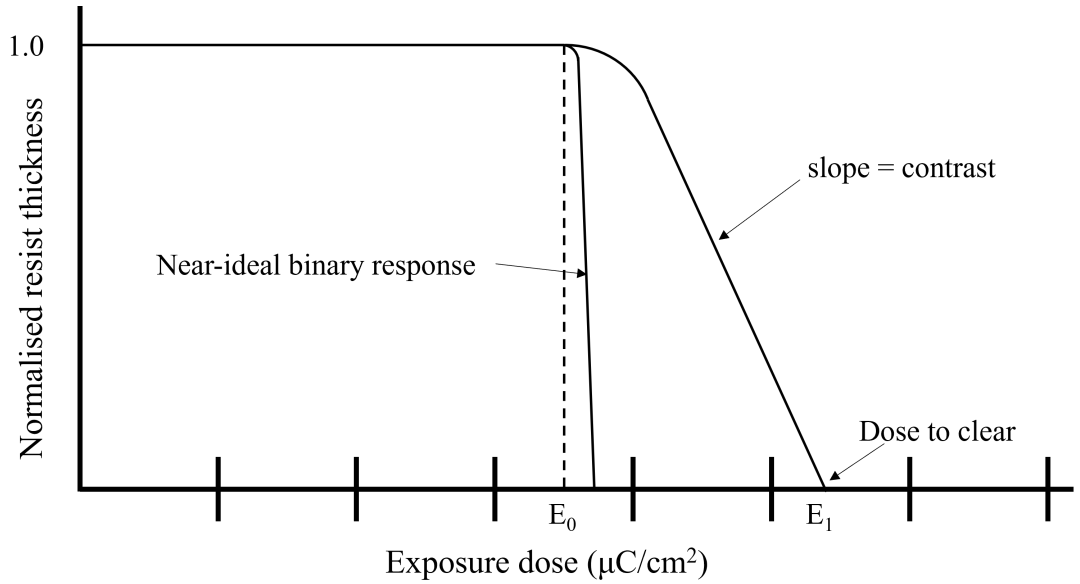

Figure 1.19: Sketch of exposure dose versus normalised resist thickness remaining *i.e.,* the negative-tone case. The near vertical line represents a near-ideal binary response. The second curve represents a more realistic case with a transition between unexposed, E_0, and fully exposed resist, E_1.

1.2.8.2 Resist Contrast

When contrast is discussed in relation to resists, it refers to the steepness in the drop-off between the exposed and unexposed regions of the resist. The ideal case is a binary response as shown in Figure 1.19. In the real case, there is a transition region between the lowest dose that doesn't cause exposure, E_0 and the dose to clear E_1 as shown in Figure 1.19. The slope of this transition region is defined as the resist contrast. The dose to clear is not an intrinsic property of a given resist, rather it is dependent on the parameters of the lithography process such as resist thickness, the choice of developer as well as development time and temperature, and accelerating voltage used during exposure.

1.2.8.3 Resist Processing

EBL and HIBL resists are typically applied to the chosen substrate via spin coating *i.e.,* drop casting the resist cased in solvent onto the surface and then spinning the substrate at a high speed. The centrifugal force and the surface tension of the solvent cause the resist to spread out across the surface evenly to form a uniform layer of resist. The

thickness of the resist layer is typically inversely proportional to the spin speed, and thus can be controlled by varying the spin speed. After spin coating the resist is softbaked to remove any remaining casting solvent. When solvent is removed during the softbake, it can leave behind voids in the resist film. These voids cause stress in the film and can affect the performance of the resist. Softbaking a resist above its glass transition temperature, T_g, allows for the resist to relax after the evaporation of the casting solvent, and improve overall film quality.

After exposure, the resist is developed in a suitable solvent. Typically, for a positive-tone process, the sensitivity and resolution of the resist increase as the temperature of the developer is reduced.[162–164] Cold temperature development has the effect of 'freezing out' the polymer chains that have been partially exposed.[164] These partially exposed chains are readily developed at room temperature, however during cold development they become locked in place and do not get developed. This improves both the contrast and resolution of the resist, but has the drawback of lowering the sensitivity of the resist, thereby increasing the exposure times needed for bond-scission to occur.[164] Cord *et al.,*[164] found that the optimal developer temperature for positive-tone PMMA using a 1:3 MIBK:IPA developer solution was approximately -15 °C. Below this temperature, the doses required become sufficiently high that PMMA begins to enter the negative-tone mode, reducing the resolution.

1.2.8.4 Poly (Methyl Methacrylate) (PMMA)

Poly (methyl methacrylate) (PMMA) is one of the most widely used EBL resists.[165] PMMA is a dual-tone resist *i.e.,* it can be used as both a positive or negative-tone resist. Under exposure from electrons or ions, molecular chains within the PMMA molecule are fragmented. Mostly it is the side groups of the polymer that are sheared, however in some cases the main backbone is broken.[165,166] The shorter chains produced from this fragmentation can be preferentially dissolved in weak solvents such as methyl isobutyl ketone (MIBK). The fragmentation of the polymer results in the formation of free radicals. At lower doses bond-scission is dominant and PMMA acts as a positive resist. However as the dose increases, so too does the generation of free radicals. Larger chain-

fragments can then cross-link with each other to form a hard insoluble material, and thus at large doses PMMA acts as a negative-tone resist.[167] To date, PMMA has been used to pattern sub-10-nm features in both the positive and negative-tone modes.[136,168]

1.2.8.5 Hydrogen Silsequioxane (HSQ)

Hydrogen silsequioxane (HSQ) is a popular negative-tone resist that has been used for the patterning of sub-10-nm features in both EBL and HIBL.[169–171] HSQ has a cubic structure ($HSiO_{3/2}$) and upon exposure there is scission of the Si-H bond and the formation of Si-OH bonds due to the presence of absorbed moisture in the resist. These silanol groups are unstable and condense to break the caged molecule to form a linear network.[172,173] Despite the high performance, HSQ is often difficult to work with due to its sensitivity to moisture in the atmosphere and polar aprotic solvents.[174,175]

1.2.8.6 Chemically-Amplified Resists

Chemically-amplified resists (CARs) are resists that have been designed to undergo a specific chemical reaction during exposure that modifies their sensitivity to the beam. A resist is typically modified by the addition of a photoacid generator (PAG). During exposure the PAG generates an acid that catalyses further exposure of the resist without receiving additional dose from the beam, therefore increasing the sensitivity of the resist.[175,176] The substrate is then subjected to a post exposure bake to allow the released photoacid to catalyse transformations involving functional groups in the polymer component of the resist *i.e.,* bond-scission or cross-linking, thus exposing the resist.[173,176] Unfortunately, non-uniform migration and diffusion of the acid within the resist during post exposure baking limits the overall resolution of CARs.[177] Furthermore, CARs exhibit poor line-edge roughness (LER) due to diffusion of the acid. One method to solve the diffusion problem has been to bond PAG units directly to the polymer chain of the resist.[178] Several polymer-bound PAG resists have been developed, however more traditional resists such as PMMA and HSQ remain the preferred choice of resist for most EBL or HIBL processes.[175,178]

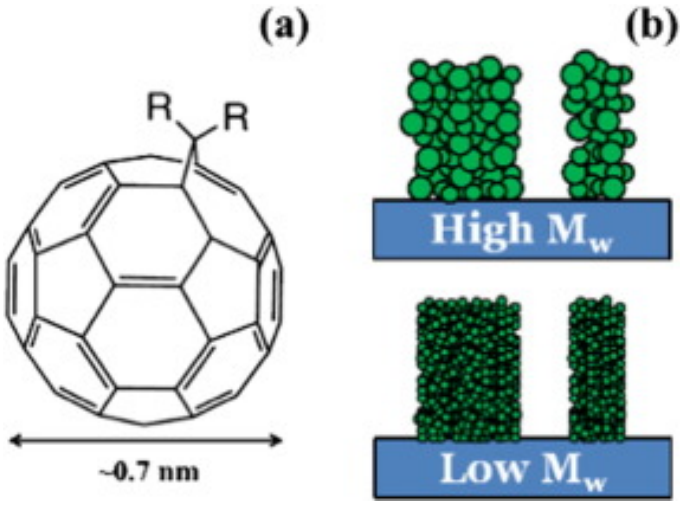

Figure 1.20: (a) Molecular diagram of generic fullerene resists. R represents the attached side chains to the C_{60} molecule. (b) Schematic showing the comparison between patterns formed from a high molecular weight resist and those from a low molecular weight resist after development.[1]

1.2.8.7 Fullerene Derivative Resists

Fullerene derivative resists incorporate fullerene, C_{60}, directly into the resist polymer and have emerged as a new class of negative-tone resists in recent years.[179–181] Fullerene derivative resists belong to a class of resist known as molecular-based resists. Fullerene has a small molecular size ($\sim$ 0.7 nm) and it has been theorised that fragmentation of the resist during exposure will yield smaller feature sizes and a reduced LER.[1] To date, sub-10-nm structures have been fabricated with HIBL using a fullerene resist.[1,182] Furthermore, non-chemically amplified fullerene derivative resists have demonstrated a high etch resistance, owing to the high carbon content of the resist.[183] Fullerene based resists are therefore an attractive resist candidate for next-generation lithography processes.

Chapter 2

Experimental Techniques

2.1 Numerical Methods

Electromagnetic simulations of the interaction of light with plasmonic nanostructures depends on solving Maxwell's wave equations numerically. The optical response of plasmonic nanostructures is based on the metal used, the geometry of the nanostructure, and the medium of the environment. The ability to determine the optical response of a given nanostructure before fabrication is of vital importance as fabrication can be both time and cost intensive. Therefore, the simulation of metal nanostructures plays an essential role in the design of plasmonic devices.

Several numerical methods are available for calculating solutions to Maxwell's equations such as Mie theory, discrete-dipole approximation (DDA), finite-element method (FEM) and finite-difference time-domain (FDTD) simulations. Mie theory is a solution of Maxwell's equations applicable to the scattering of an incident plane wave by a spherical, isotropic, and non-magnetic particle in a non-absorbing isotropic medium.[184] Mie theory remains an important tool today as it is the only simple, exact analytical solution to Maxwell's equations that is relevant to particles.[14] Furthermore, most colloidal preparations of nanoparticles consist of approximately spherical nanoparticles that can be modelled by Mie theory. The advent of modern lithography techniques such as electron-beam lithography (EBL) has made it possible to fabricate nanoparticles with more complex ge-

ometries. Mie theory is limited to spheres and particles that possess rotational or axial symmetry. In addition to this Mie theory does not consider the effects of electromagnetic coupling between particles in a periodic array. Therefore other numerical techniques are required to simulate the optical properties of nanoparticles with non-spherical geometries and within arrays or clusters.

The discrete dipole approximation (DDA) can be used to calculate the optical response of arbitrary geometries by approximating each particle as a finite array of polarisable points.[93] Each point acquires a dipole moment in response to the local electric field and the dipoles also interact with each other via their individual electric fields. This reduces the solution of Maxwell's equations to an algebraic problem of many coupled dipoles.[93,184] While the DDA is suitable for evaluating two or more particles of arbitrary geometries, it is impractical for simulating periodic arrays with large numbers of particles. This is due to the fact that the total number of dipoles included in the calculation is proportional to the total number of particles in the array. Therefore the time required to perform the calculation limits the scalability of the DDA.

The finite element method (FEM) and finite-difference time-domain (FDTD) techniques divide the simulation region into a mesh structure (tetrahedral for FEM, and cubic for FDTD), and calculate the electric field distribution at each mesh unit. The FEM technique discretises the Helmholtz equations in space and then solves them numerically to find fields that satisfy the boundary conditions for each mesh cell. The FDTD method discretises the spatial and temporal derivatives in the Maxwell curl equations. A plane wave is then injected at an initial time and new field components are calculated using the field components that applied during the previous time interval.[184] Both FEM and FDTD techniques are preferable to the DDA when performing simulations for periodic arrays of nanoparticles. However, there is a trade-off between increasing accuracy (reducing mesh size) and calculation time for both techniques. In this thesis the FDTD method is used for all electromagnetic calculations.

2.1.1 Finite-Difference Time-Domain Method

The FDTD method, first introduced by Yee in 1966,[185] solves Maxwell's equations by replacing them with a set of finite difference equations. Maxwell's curl equations in a linear, isotropic, lossy, nondispersive medium are:[186]

$$\frac{\delta \boldsymbol{H}}{\delta t} = -\frac{1}{\mu}\nabla \times \boldsymbol{E} - \frac{1}{\mu}(\boldsymbol{M}_{source} + \sigma^* \boldsymbol{H}), \tag{2.1}$$

$$\frac{\delta \boldsymbol{E}}{\delta t} = \frac{1}{\epsilon}\nabla \times \boldsymbol{H} - \frac{1}{\mu}(\boldsymbol{J}_{source} + \sigma \boldsymbol{E}), \tag{2.2}$$

where $\boldsymbol{E}$ and $\boldsymbol{H}$ are the electric and magnetic fields respectively, $\boldsymbol{J}_{source}$ and $\boldsymbol{M}_{source}$ are the electric current density and equivalent magnetic current density respectively. In this case both of these current densities are acting as independent sources. The electric conductivity and equivalent magnetic loss are given by σ and σ^* respectively, and ϵ and μ are the electric permittivity and magnetic permeability respectively.

If we consider a structure that extends to infinity in the z-direction, and that the incident wave is also uniform in the z-direction, all partial derivatives with respect to z must equal zero. Under these conditions, the full set of Maxwell's curl equations in Cartesian coordinates are reduce to two modes; the transverse-magnetic mode with respect to z (TM$_z$) and the transverse-electric mode with respect to z (TE$_z$). The TM$_z$ mode equations involving only $H_x,\ H_y$, and E_z are given by:

$$\frac{\delta H_x}{\delta t} = \frac{1}{\mu}\left[-\frac{\delta E_z}{\delta y} - (M_{source_x} + \sigma^* H_x)\right], \tag{2.3}$$

$$\frac{\delta H_y}{\delta t} = \frac{1}{\mu}\left[\frac{\delta E_z}{\delta x} - (M_{source_y} + \sigma^* H_y)\right], \tag{2.4}$$

$$\frac{\delta E_z}{\delta t} = \frac{1}{\epsilon}\left[\frac{\delta H_y}{\delta x} - \frac{\delta H_x}{\delta y} - (J_{source_z} + \sigma E_z)\right]. \tag{2.5}$$

The TE$_z$ mode equations involving only E_x, E_y, and H_Z are given by:

$$\frac{\delta E_x}{\delta t} = \frac{1}{\epsilon}\left[\frac{\delta H_z}{\delta y} - (J_{source_x} + \sigma E_x)\right], \tag{2.6}$$

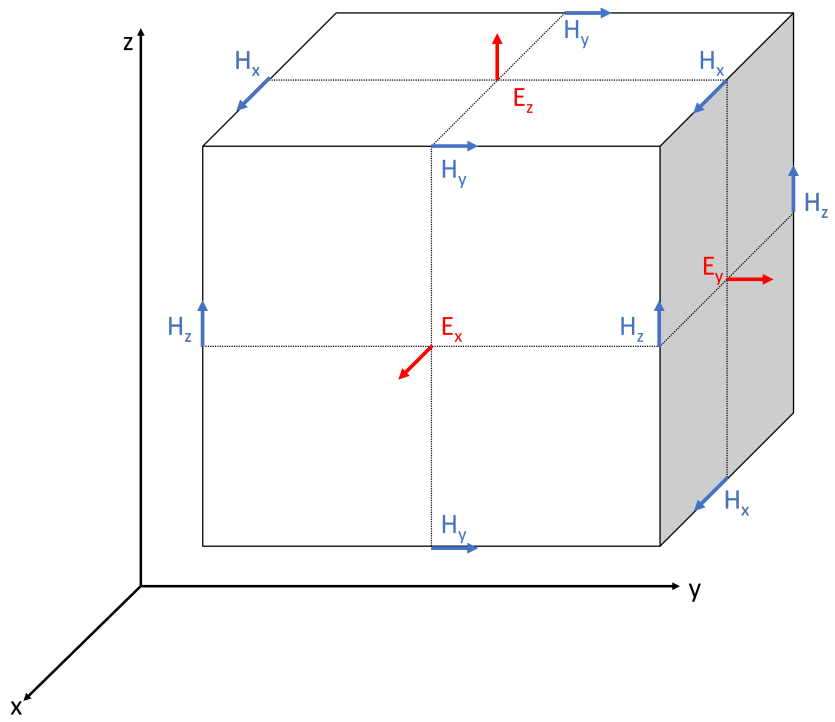

Figure 2.1: Position of the electric and magnetic field vector components about a cubic unit cell of the Yee space lattice.

$$\frac{\delta E_y}{\delta t} = \frac{1}{\epsilon}\left[-\frac{\delta H_z}{\delta x} - (J_{source_y} + \sigma E_y)\right], \tag{2.7}$$

$$\frac{\delta H_z}{\delta t} = \frac{1}{\mu}\left[\frac{\delta E_x}{\delta y} - \frac{\delta E_y}{\delta x} - (M_{source_z} + \sigma^* H_z)\right]. \tag{2.8}$$

The Yee algorithm divides the simulation volume into "Yee-cells" and centres the $\boldsymbol{E}$ and $\boldsymbol{H}$ components in three-dimensional space such that every $\boldsymbol{E}$ component is surrounded by four perpendicular $\boldsymbol{H}$ components and vice-versa, as shown in Figure 2.1. The Yee algorithm also centres the $\boldsymbol{E}$ and $\boldsymbol{H}$ components in time in what is known as a leapfrog arrangement as shown in Figure 2.2. The $\boldsymbol{E}$ components are solved at a given instant in time using the stored values for the $\boldsymbol{H}$ components. The simulation is then shifted forward in time by the half the specified finite time difference, Δt/2, and the next set of $\boldsymbol{H}$ components are calculated using the stored values for the $\boldsymbol{E}$ components that have just been calculated. The simulation continues until the specified time length, or steady-state field condition has been reached.

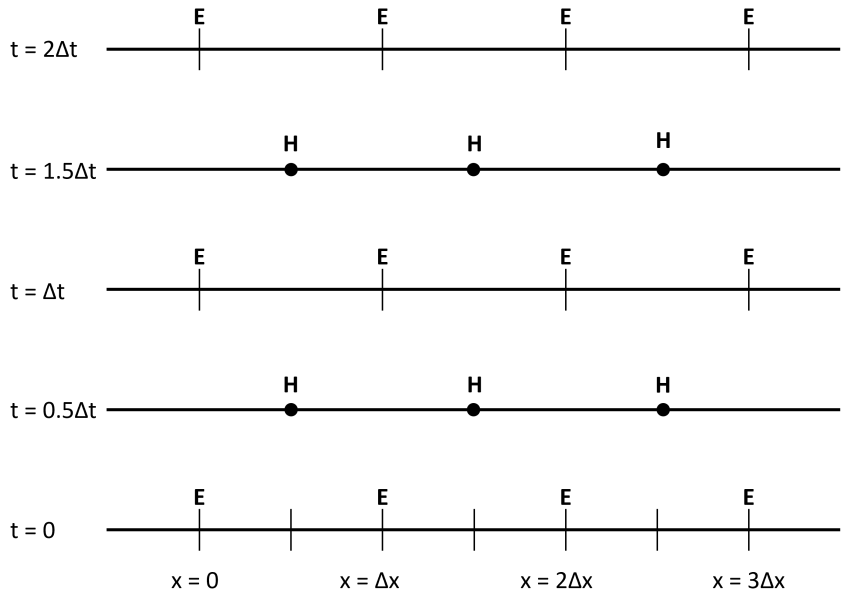

Figure 2.2: Position of the electric and magnetic field vector components in space and time for a one-dimensional Yee cell.

2.1.2 FDTD Simulations

Simulations for the near-field distributions and extinction spectra of plasmonic Au nanoantennas in this work were performed using the commercially available *ANSYS Lumerical FDTD Solver* from *ANSYS Inc*.

In order to calculate the optical properties using FDTD methods, accurate knowledge of the complex refractive index over the frequency range of the simulation is required for all materials used in the simulation. Values for the refractive index of Au in the visible and mid-IR ranges of light were taken from Johnson and Christy, and Palik respectively.[72,187] Values for the refractive index of Ti and SiO_2 in the visible and mid-IR range of light were taken from Palik.[187] Values for the refractive index of SiN_x in the visible and mid-IR ranges of light were taken from Philipp and Kischkat *et al.* respectively.[188,189] Values for the refractive index of ITO in the visible and mid-IR ranges of light were taken from König *et al* and Tamada *et al.* respectively.[190,191]

When simulating the optical properties of Au nanoantennas in this thesis, 20-nm-thick Au on top of a 1-nm-thick Ti layer were placed on the relevant substrate. For nanoantennas on ITO substrates, a 100-nm-thick ITO layer on top of a bulk SiO_2 substrate was

used. For nanoantennas on SiN_x TEM membranes, a 10-nm-thick SiN_x layer was used as a substrate. The FDTD simulation unit cell is designed to match with the period of the nanoantennas fabricated using EBL *i.e.,* 400 nm in the *y*-direction for both bowtie and nanodiamond structures, 400 nm in the *x*-direction for bowtie nanoantennas, and 230 nm in the *x*-direction for a pair of nanodiamonds. The choice of appropriate boundary conditions for the FDTD unit cell is of high importance for FDTD calculations. To simulate individual nanoantennas, perfectly matched layers (PML) are used as boundary conditions. The PML is an absorbing layer designed to absorb without reflection all electromagnetic waves in the simulation region.[192] As the nanostructures in this thesis are fabricated in periodic arrays, it is essential to used boundary conditions that account for this periodicity and account for interactions between neighbouring nanoantennas. Symmetric and anti-symmetric boundary conditions were used in the FDTD simulations in this thesis as they account for the periodicity of the arrays while exploiting the symmetry of the nanoantennas to reduce the overall simulation time by a factor of 4.

A total-field scattered-field (TFSF) source polarised in the *x*-direction was used as the light source for these FDTD simulations. For mid-IR simulations, spectra were also simulated with the light source polarised in the *y*-direction as well. The TFSF source is often used for the study of the scattering of light from small particles. The source consists of a plane wave that propagates along the *z*-axis. The source encloses a user-defined 3D geometry. The light within this region consists of the sum of the incident wave and the scattered field *i.e.,* the total field. The light outside this region consists of only the scattered field. Therefore, the absorbed light can be determined as the difference between the total and scattered fields. The source was specified to have a wavelength of 600-900 nm in all simulations for Au nanoantennas designed to be resonant in the optical and near-IR part of the spectrum. For simulations involving mid-IR antennas, wavelengths from 4-7 μm were used.

The FDTD simulation region is divided into a cubic mesh. Only one material can be assigned to each mesh cell. The material that makes up the majority of the volume of a unit cell is chosen as the material for that cell. Ideally there should be at least 10 mesh cells per wavelength in the simulation, however it is possible that a smaller mesh size is

required in order to accurately approximate small feature sizes. A mesh size of 0.5 nm $\times$ 0.5 nm $\times$ 0.5 nm was used in the simulations in this thesis for antennas designed to be resonant in the near-IR. For the large antennas, A1,A2, and A3, designed to be resonant in the mid-IR region of the spectrum, a mesh-size of 10 nm $\times$ 10 nm $\times$ 5 nm was used.

2.2 Optical Spectroscopy

UV-vis spectroscopy was used throughout this work to probe the plasmon resonances of fabricated structures. Due to the microscopic sizes of the structures fabricated, an in-house microscope connected to a spectrograph was used to measure these extinction spectra. An extinction spectrum is typically composed by collecting three individual spectra. The background or "dark" spectrum is the signal recorded when the illumination in the system is switched off *i.e.,* it is the signal from any sources of light already present in the room. Next, the extinction spectrum of a suitable reference is used. For example, we commonly fabricate our structures on an ITO substrate. To collect the reference spectrum, we collect a spectrum from a location on the ITO substrate that doesn't possess any fabricated structures. Finally the sample spectrum is collected by moving the desired structures into the beam path. The reference and background spectra are subtracted from this spectrum to give the extinction spectrum of just the desired structures.

In general, it is the power before and after illumination that is recorded by the spectrometer. Transmittance is defined as the ratio of the power of the illuminating light before passing through the sample, P_0, to the power of the transmitted light P.

$$T = \frac{P}{P_0}. \tag{2.9}$$

The absorbance, A, is related to the transmittance by

$$A = log(\frac{P_0}{P}) = log(\frac{1}{T}). \tag{2.10}$$

Optical spectroscopy in this thesis was performed using a *CRAIC QDI 1000* microspectrophotometer. The samples were imaged using a 15$\times$ reflecting objective lens

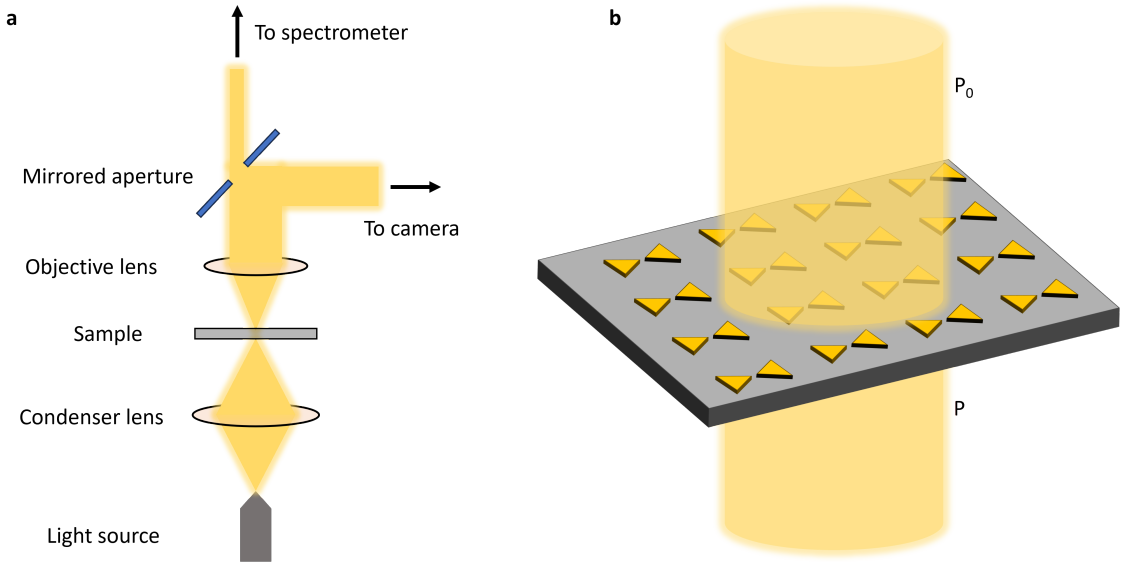

Figure 2.3: (a) Schematic of the setup used to record optical spectra in this thesis. (b) Schematic illustration of change in transmitted radiant power as the light passes through a resonant nanoantenna array.

with a NA of 0.28. The microscope features a 10×10 µm pinhole that can be aligned to features on a given sample to collect the spectrum from this pinhole.

2.3 FTIR Spectroscopy

Like optical spectroscopy, IR spectroscopy is based on illuminating a sample with radiation and measuring the absorbance of the sample at each wavelength. Absorbance in the IR region of the spectrum typically corresponds to molecular vibrations. These vibrations occur at frequencies that are unique to the chemical bond and compound, therefore IR spectroscopy can be used to confirm the presence of specific chemical species.[193,194]

Traditional dispersive IR spectroscopy involves scanning the illuminating light across each IR wavelength, which is quite time-consuming. Fourier-transform IR (FTIR) spectroscopy involves using an interferometer to illuminate the sample with multiple wavelengths of light at once. Applying a Fourier-transform to the resulting interference pattern allows the frequencies of light absorbed by the sample to be extracted, resulting in the collection of an IR spectrum that is much less time-consuming than dispersive IR spectroscopy.[194]

IR spectra from segmented plasmonic antennas were collected using a *PerkinElmer Spotlight 200i FT-IR with Spectrum Two System*. Spectra were recorded using either 128 or 32 $\times$ 1 s accumulations.

2.4 Raman Spectroscopy

Inelastic light scattering describes the phenomenon by which a light beam is scattered by an optical medium resulting in a change in the energy, and thus wavelength, of the light. C.V. Raman discovered the inelastic scattering of light by molecules in 1928,[195] however the signal of the scattered light was very weak, so there was little interest in the practical effects of this scattering at the time of discovery. As the phonon or molecular vibration that causes the inelastic scattering has a quantised energy, the energy of the scattered signal is dependent on the initial wavelength of the light. Therefore if the exciting light has a broad dispersion, the wavelength of the inelastic scattered light could overlap with the wavelength of the elastically scattered light, due to the small shift in the wavelength of the inelastically scattered light. The invention of lasers meant that monochromatic light sources with high powers were available, making the inelastically scattered signal much easier to detect. This led to an increase in the popularity of Raman spectroscopy.

Inelastic scattering can occur via scattering of incident photons by phonons or by molecules as shown in Figure 2.4(a). In the case of phonon scattering, incident light with energy $\hbar\omega_1$ and momentum k_1 is scattered to new energy $\hbar\omega_2$ and momentum k_2 resulting in the emission of a phonon with energy $\hbar\Omega$ and momentum q, where

$$\omega_1 = \omega_2 \pm \Omega, \tag{2.11}$$

and

$$k_1 = k_2 \pm q. \tag{2.12}$$

The signs in equations 2.11 and 2.12 correspond to the emission or absorption of a phonon. If a phonon is emitted during the scattering process, the energy and momen-

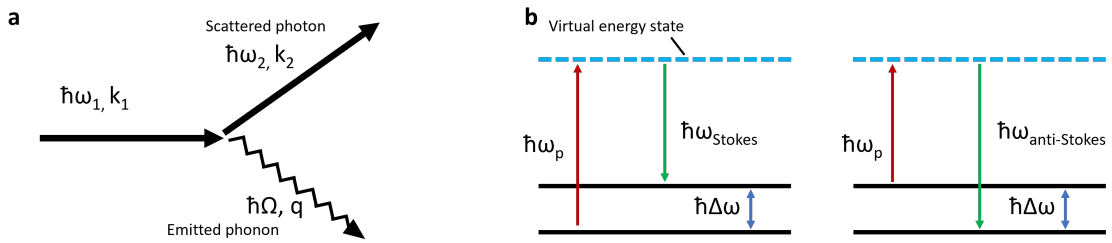

Figure 2.4: (a) Inelastic scattering of light by a phonon. Incident light with energy $\hbar\omega_1$ and momentum k_1 is scattered to new energy $\hbar\omega_2$ and momentum k_2 resulting in the emission of a phonon with energy $\hbar\Omega$ and momentum q where $\hbar\omega_1 > \hbar\omega_2$ and $k_1 > k_2$ (Stokes scattering). In the case for phonon absorption (anti-Stokes scattering) $\hbar\omega_2 > \hbar\omega_1$ and $k_2 > k_1$. (b) Inelastic scattering of light by a molecule. Light with incident energy $\hbar\omega_p$ excites an electron to a virtual energy level in a molecule. The relaxation of the electron results in the emission of a photon. If the electron relaxes to a higher energy level than it originally occupied, the emitted photon will have lower energy than the incident photon (Stokes scattering). If the electron relaxes to a lower energy level than it originally occupied, the emitted photon will have a higher energy than the incident photon (anti-Stokes scattering).

tum of the scattering light will be lower than the incident light and thus the signs will be negative, this is known as Stokes scattering. If a phonon is absorbed during the scattering process, the energy and momentum of the scattered light will be greater than the incident light and the signs will be positive, this is known as anti-Stokes scattering. Light can also be inelastically scattered by molecules as shown in Figure 2.4(b). Incident light excites an electron to a short-lived 'virtual' energy state. The electron quickly relaxes to a ground state energy level resulting in the emission of a photon. If the final energy level is higher in energy than the initial energy level, the scattered photon will be lower in energy than the incident photon (Stokes scattering). If the final energy level is lower in energy than the initial energy level, the scattered photon will have higher energy than the incident photon (anti-Stokes). It can be seen from above that in order for anti-Stokes scattering to occur, the scattering medium must already possess either phonons or excited electrons. Therefore the probability for anti-Stokes scattering decreases at low temperatures. Conversely, Stokes scattering can occur at any temperature. The ratio of anti-Stokes to Stokes scattering is given by:

$$\frac{I_{anti-Stokes}}{I_{Stokes}} = \exp(\hbar\Omega/k_B T), \tag{2.13}$$

where Ω is the frequency of the transition, and k_B is the Boltzmann constant. The signal

from Stokes scattering is therefore typically much stronger than the anti-Stokes signal, and it is the Stokes scattering that is usually measured during Raman spectroscopy. Light can also be scattered elastically *i.e.,* absorbed and then emitted without a change in photon energy. Elastic scattering, known as Rayleigh scattering, has a much larger probability of occurring than inelastic scattering, and therefore Raman spectra feature an intense Rayleigh scattering peak around 0 cm^{-1}.

Multiple Raman microscopes were used to collect Raman spectra throughout this thesis. The Raman signal from bulk Ge nanowires was collected using a *RamanFlex 400* coupled to an *Olympus* upright microscope via a *Perkin Elmer Raman Micro 200* module. A 785 nm laser magnified by a 50× objective lens was used to collect the spectrum. The number of acquisitions was 2, and the exposure time for each acquisition was 10 s. Raman signal from isolated Ge nanowires was collected using a *Renishaw Qontor* system. A mapping spectrum was collected using a 785 nm laser magnified with a 100× objective lens. At each point on the map 50 acquisitions of 1 s each were collected. The mapping step size was 500 nm, and the total area mapped was 6.5×5.5 μm. The Raman signal from a carbon nanodot was collected using a *Horiba* Raman system (*LabRam* ARAMIS HORIBA Jobin Yvon). A 785 nm laser polarised parallel to the plasmonic bowties was used with a 100× (0.53 NA) objective. The spectrum was collected using a 4 × 4 map, with a step size of 200 nm, aligned optically to the centre of the plasmonic bowtie. 5 × 1 s accumulations were collected at each point.

2.5 Transmission Electron Microscopy

Transmission electron microscopy (TEM) is an imaging technique whereby a beam of electrons is transmitted through a specimen to form an image. Electrons that pass through the specimen possess valuable information about the internal structure of the specimen such as crystal structure and morphology. Furthermore, the resolution achievable using TEM is much higher than that possible using SEM, owing to the higher accelerating voltages used in TEM ($\sim$ 100 keV). Specimens being studied by TEM are typically $<$ 100 nm thick suspended on a thin membrane or grid in order for electrons to be able to

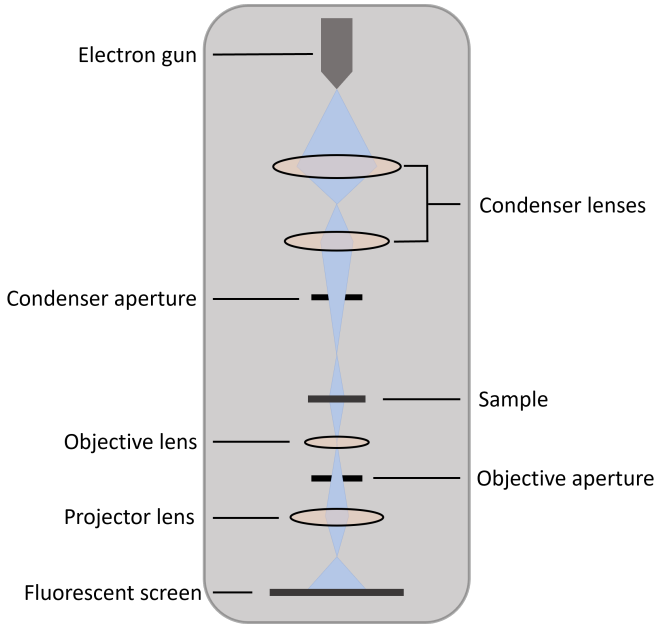

Figure 2.5: Schematic of a transmission electron microscope (TEM). The electron beam is emitted from the electron gun, and is then focused and accelerated through the column. The condenser aperture reduces aberrations as well as the overall beam current. The beam is transmitted through the sample and the resulting signal is focused by the objective lens through the objective aperture. The projector lens projects the transmitted signal onto a fluorescent screen where it can be viewed.

pass through. The image from the transmitted electrons is then magnified and focused onto an imaging device such as a phosphorescent screen or an electronic detector. A *JEOL 2100* TEM operating with an accelerating voltage of 200 kV was used in this thesis to obtain TEM images of negative-tone PMMA and fullerene-derivative structures fabricated using HIBL. A *FEI Titan* TEM operating with an accelerating voltage of 300 kV was used to obtain high resolution images of Ge grown on Au nanoantennas, and to probe the structure and elemental composition of the grown Ge.

2.6 Energy Dispersive X-Ray Spectroscopy

Energy dispersive x-ray spectroscopy (EDX or EDS) is an analytical technique used to provide elemental analysis of a sample by analysing the x-rays produced via the interaction of an electron beam with the sample. Sample interactions with the incident electron beam can result in the emission of a core electron from the sample. This results

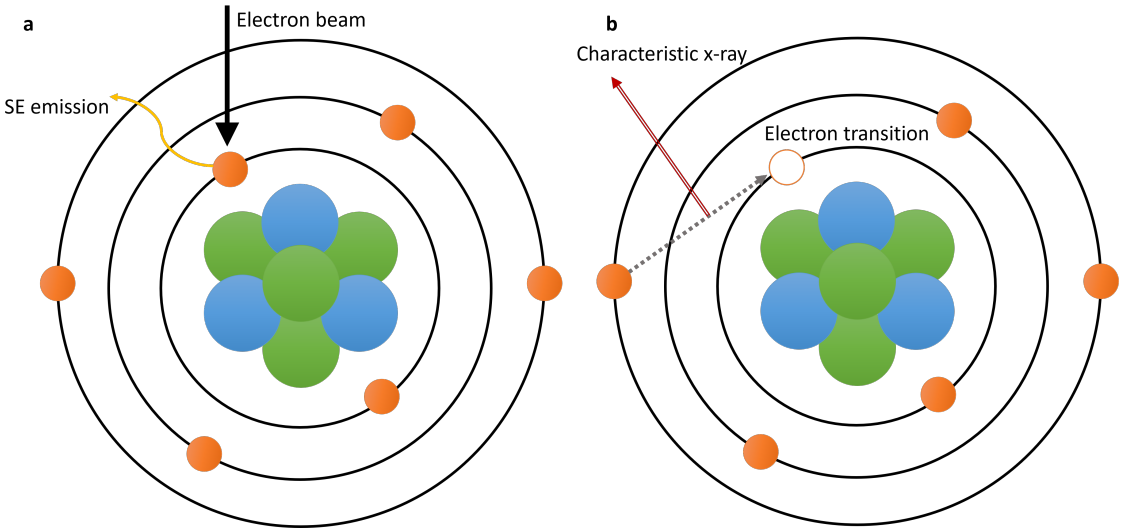

Figure 2.6: Schematic showing the generation of characteristic x-rays in an electron microscope. (a) The incident electron beam excites an inner core electron, giving it enough energy to escape the atom. (b) A higher energy electron drops down to fill the vacancy left behind by the excited electron, resulting in the generation of an x-ray.

in the transition of an electron from a higher energy level to the core energy level in order to fill the vacancy left by the excited electron. This transition generates a characteristic x-ray that can be collected by an appropriate detector. As each element has discrete energy levels, the x-rays produced have fixed characteristic energies. Therefore, the energy of the x-rays produced can provide information about the element that produced them. EDX is an excellent complementary analysis tool to SEM or TEM as the electron beam used to image the sample also produces the x-rays used for EDX analysis.

In this thesis, EDX was used during both SEM and TEM to confirm the presence of Ge in the grown material after the laser-induced Ge growth process. A SEM (*Zeiss Ultra Plus* with an integrated 20 mm^2 *Oxford Inca* EDX detector was used to analyse characteristic x-rays from samples supported by bulk substrates. The SEM was operated in the high-current mode using the in-lens secondary electron detector at a working distance of approximately 11 mm. An accelerating voltage of 5 keV was used with an objective aperture of 60 µm. EDX analysis during TEM was carried out using a *Bruker* 6-30 SDD in a *FEI Titan* TEM operated at 300 keV.

2.7 Fabrication of Nanostructures using Electron and Helium Ion Beam Lithography

2.7.1 Fabrication of Au Nanoantennas on ITO Substrates

100-nm-thick tin-doped indium oxide (ITO) on bulk glass substrates were purchased from *Ossila Ltd.*. To clean these substrates they were first immersed in 1% *Hellmanex* surfactant solution and sonicated for 5 min at 25 °C to remove particulate contaminants, followed by rinsing with deionised water and isopropyl alcohol (IPA). The substrates were then plasma-cleaned with an oxygen plasma using a *Diener PICO Barrel Asher* for 5 min at 0.3 mbar with a plasma power of 100 W to remove organic residues and aid wetting of PMMA resist. PMMA (2% 950k PMMA in anisole purchased from *EM Resist Ltd.*) was spun onto each substrate at a rate of 2 krpm with an acceleration rate of 2 krpm/s for 60s to give a resist thickness of approximately 70 nm. After spin-coating the substrates were baked at 180 °C for 2 min on a hot plate in order to remove any excess casing solvent and relax stress in the resist film. EBL was performed using a *Zeiss SUPRA 40* scanning electron microscope modified with a *Raith Elphy Quantum* pattern generator. The resist was exposed using an accelerating voltage of 15 kV and an area dose of 1300 μC/cm^2. Following electron-beam exposure, the resist was developed in a 1:3 methyl isobutyl ketone (MIBK):IPA solution at 0 °C for 30 s using a thermoelectric cold plate. Low temperature development was used for positive-tone lithographic processes as it improves both contrast and resolution.[164] The developed sample was coated with metal using a *Temescal FC-2000* electron-beam evaporation system. A 1-nm-thick layer of Ti was first deposited at a rate of 0.2 Å/s as an adhesion layer, followed by a 20-nm-thick layer of Au deposited at a rate of 0.5 Å/s. This rate was used for Au as McPeak *et al.* found that Au films deposited at 0.5 Å/s had better optical properties in the IR region than films deposited at higher deposition rates.[73] The EBL pattern was transferred to the substrates via a lift-off process by immersing the sample in n-methylpyrrolidone (NMP) at 60 °C for 45 min. The sample was then rinsed with acetone then IPA before being oxygen plasma-cleaned using a *Diener PICO Barrel Asher* for 5 min at 0.3 mbar with a plasma power of 100 W.

2.7.2 Fabrication of Au Nanoantennas on TEM Membranes and X-Ray Windows

10-nm-thick and 50-nm-thick silicon nitride (SiN_x) membranes supported on a Si carrier wedge, were purchased from *SiMPore* via *TEMwindows.com*. The substrates were first plasma-cleaned with an oxygen plasma using a *Diener PICO Barrel Asher* for 5 min at 0.3 mbar with a plasma power of 100 W. PMMA (2% 950k PMMA in anisole purchased from *EM Resist Ltd.*) was spun onto each substrate at a rate of 5 krpm with an acceleration rate of 8 krpm/s for 60s to give a resist thickness of approximately 70 nm. Higher spin speeds and acceleration rates are required for the small (3 mm for TEM windows and 5 mm for x-ray windows) chips in order to reduce edge-beading of the resist, and to yield a uniform resist film. The subsequent electron-beam exposure and metallization steps were the same as outlined in the previous section.

2.7.3 Fabrication of Negative-Tone Structures for Point-Spread Function Measurements

5-nm-thick SiN_x membranes supported on a Si carrier wafer were purchased from *SiMPore Inc.* via *TEMwindows.com* The substrates were first plasma-cleaned with an oxygen plasma using a *Diener PICO Barrel Asher* for 5 min at 0.3 mbar with a plasma power of 100 W. PMMA (1 wt.% 950k molecular weight PMMA in anisole purchased from *EM Resist Ltd.*) and a fullerene-derivative e-beam resist (supplied by *Irresistible Materials Ltd.* was spin coated onto ultrathin membranes with a spin speed of 5 krpm and acceleration of 8 krpm to achieve a thickness of approximately 15 nm for both resists. Experimental PSFs were measured by exposing square arrays of single-pixel exposures at various ion doses using a pitch of 100 nm. Exposures were performed using a *Zeiss Orion NanoFab* with a He^+ ion landing energy of 30 keV. Point exposures were made within a 50 μm writefield using a *Raith Elphy Multibeam* pattern generator. Typical experiments used a beam current of 0.3-1.0 pA, working distance of 8 mm and a helium pressure of 2×10^{-6} Torr. An aperture size of 5 μm was used to obtain the smallest possible probe size, a large depth of field, and achieve higher patterning resolution. The spot number,

which is used to balance the trade-off between probe size and beam current, was set to a value of 4. Ion dose per pixel was varied, and plotted vs measured feature radius. PMMA samples were developed by immersion in room-temperature acetone for 30 s followed by a rinse with IPA. Fullerene-derivative samples were developed by immersion in room-temperature cyclohexanone for 30 s followed by a rinse with IPA. Exposed structures were characterized by scanning electron microscopy (*Zeiss Supra 40*) and bright-field transmission electron microscopy (*JEOL 2100* operating at 200 keV).

2.8 Simulation of Point-Spread Functions

A full description of the simulation methods used to calculate the PSF is given by Winston *et al.*[196] In order to calculate the PSF, the escape depth, λ_d, the effective energy required to produce an SE, ϵ, the density, ρ, for both the resist and substrate, and the energy and number of the incident He^+ ions must be specified. Ramachandra *et al.*[197] performed simulations to calculate these parameters for a wide range of elements. The values used to calculate the PSF for PMMA are λ_d = 10.8 Å and ϵ = 59 eV. These are the values the authors calculated for elemental carbon, and were selected as there is no data available for PMMA or elemental hydrogen or oxygen. Densities of 1.18 g/cm^3, 1 g/cm^3, and 3.17 g/cm^3 were used for PMMA, the fullerene-derivative resist, and SiN_x respectively. As no data could be found for the fullerene-derivative resist, data for fullerenol from Vraneš *et al.* was used as this molecule is similar to the fullerene-derivative resist.[198] The energy of the He^+ ions was set as 30 keV, and the number of ions was 100,000.

2.9 Laser-Induced SLS Growth of Semiconductors

Diphenylgermane (DPG) was purchased from *Fluorochem Ireland Ltd*. Zinc nitrate hexahydrate ($ZnN_2O_6{\cdot}6H_2O$) and hexamethylenetetramine (HMTA) and were purchased from *VWR Chemicals*. The ZnO precursor solution consisted of a 1:1 mixture of aqueous 75 mM HMTA and aqueous 75 mM $ZnN_2O_6{\cdot}6H_2O$. Cells for laser exposure were made-up as shown in Figure 1.7. For nanoantennas on bulk ITO substrates, a silicone

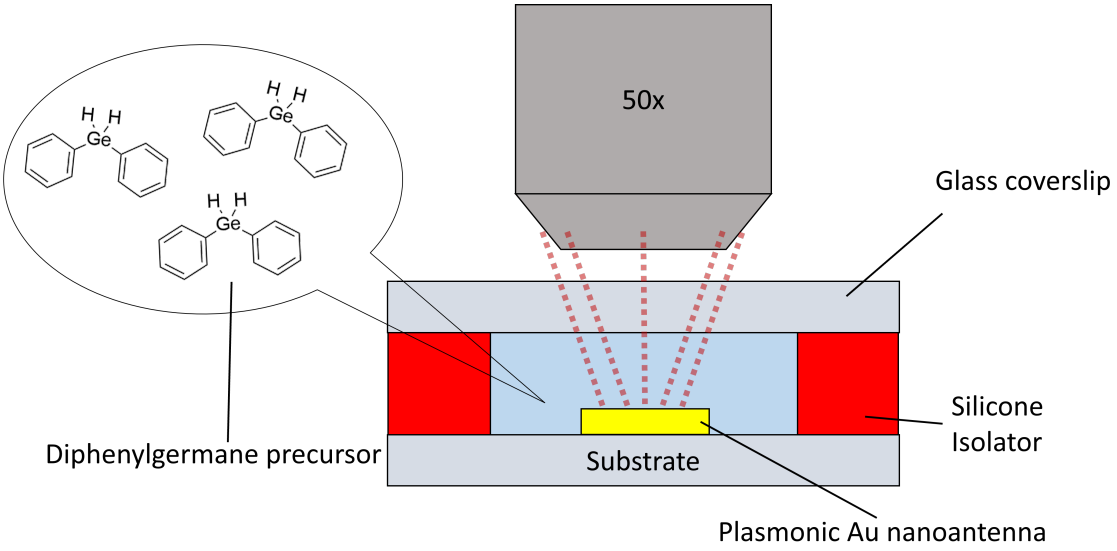

Figure 2.7: Schematic of the setup used for the LSPR growth of Ge and ZnO.

isolator (aperture diameter = 7 mm) was placed directly onto the substrate such that the nanoantenna arrays were located in the centre of the isolator. The well was filled with DPG or ZnO precursor and sealed with a glass cover slip, ensuring that no air bubbles were present in the sealed cell. For growth of Ge, laser exposure was performed using a 785 nm wavelength laser magnified via a 50× objective lens with a NA of 0.53, yielding a spot size with diameter of approximately 2 µm. Laser power was varied from 30-60 mW resulting in laser intensities of 0.96-1.9 MW/cm^2. Exposure times ranged from 1 s to 5 min. For growth of ZnO, laser exposure was performed using a 785 nm wavelength laser magnified with a 20× laser with a NA of 0.53, yielding a spot size of approximately 5 µm. A laser power of 60 mW was used for all exposures, corresponding to a laser power of 306 kW/cm^2. Exposure times ranged from 2 - 200 s. Following laser exposure, the glass cover slip and silicone isolator were removed from the sample, and the sample was subsequently rinsed with acetone followed by IPA.

Chapter 3

Measurement of the Point-Spread Function of a Focused Helium Ion Beam on Ultrathin Membranes

3.1 Introduction

Helium-ion-beam lithography (HIBL) offers significant advantages over electron-beam lithography (EBL) for the fabrication of dense arrays of nanostructures on surfaces. The probe size, or beam diameter, in a helium-ion microscope has been reported to be as small as 0.25 nm, and the convergence angle of the beam at the sample is typically lower than that of an electron beam of equivalent energy in a scanning electron microscope.[147,148] Thus He^+ ion beams have a larger depth of field than equivalent electron beams.[147,148,199,200] He^+ ions typically produce a larger secondary electron (SE) yield than electrons of equivalent energy, resulting in more efficient lithographic exposure due to improved resist sensitivity.[171,201,202] He^+ ion beams also exhibit a reduced proximity effect relative to electron beams of equivalent energy.[1,149] Here, we calculate and measure the point-spread function (PSF) of 30 keV He^+ ions in poly (methyl methacrylate) (PMMA) and a fullerene-derivative resist on ultrathin silicon nitride membranes. We compare the PMMA PSF to similar work by Manfrinato *et al.*[136] measuring the PSF of

200 keV electrons in PMMA using an aberration-corrected scanning transmission electron microscope (STEM). PSFs were calculated using the method developed by Winston *et al.*[196]

3.1.1 Proximity Effect

Proximity effects arise from the fact that the region exposed by an incident beam of charged particles is larger than the diameter of the beam. This is due to scattering of incident ions/electrons within the resist and substrate, resulting in SE generation, and thus exposure of the resist some distance away from the point of incidence of the beam. This is of particular importance when determining the smallest point-to-point distance resolvable by charged-particle lithography. When two features are in close proximity to each other, the dose tails of exposed regions can overlap and sum, resulting in unwanted indirect exposure of the region between directly exposed areas. This indirect exposure is known as the proximity effect. A good understanding of the proximity effect is important as it allows for corrections to be made to exposure dose in a lithographic process, facilitating the fabrication of denser arrays of nanostructures and the fabrication of sharper features having lower radii of curvature.

3.1.2 Sample Interaction

Close to the sample surface, He^+ ion beams typically exhibit lower scattering angles relative to electron beams of equivalent kinetic energy.[149] For example, Cohen-Tanugi *et al.*[203] estimated an interaction radius of 1 nm for 30 keV He^+ ions at a depth of 10 nm beneath the surface of a silicon substrate. For electrons and Ga^+ ions of the same energy, the interaction radii at this depth were 2 nm and 15 nm respectively. While the interaction radius of electrons was estimated to be only slightly larger than that for He^+ ions, there are still secondary electrons (SEs) generated outside of this radius. This is because SEs can be generated via multiple direct and indirect pathways.

Type 1 secondary electrons (SE1s) are generated directly by inelastic scattering of the incident charged particle beam close to the sample surface.[204] There are multiple routes

for the indirect production of type 2 secondary electrons (SE2s). One mechanism for SE2 generation is via inelastic scattering of backscattered particles as they return toward the sample surface. A second mechanism is the generation of SE2s by SE1s, however, given the low energy of SE1s generated in helium-ion microscopy, this mechanism is a negligible contributor to SE production.[150] A third route to SE2 generation is via the recoil of atoms in the sample following interaction with an incident energetic particle. Recoiling atoms can kinetically excite electrons provided that the atom velocity is greater than the Fermi-velocity of electrons in the target material.[150] Moreover, electron energy-loss spectroscopy studies of the interaction of energetic electron beams with resist layers have suggested that volume plasmons play a role in lateral energy spread in EBL resists via the production of SEs at radial locations of up to 10 nm from the incident beam.[205] The lower velocity of helium ions relative to electrons of the same kinetic energy may mean that electrons in the resist can respond to screen the charge of a slow moving helium ion thus reducing the probability of plasmon excitation.[206]

Ramachandra *et al.*[197] performed numerical calculations to determine the SE2:SE1 ratio for a range of materials and found that a higher ion energy (>10 keV) yields a lower SE2:SE1 ratio, and thus yields higher resolution. The escape depth, λ_d, of SEs varies for different materials. Ramachandra *et al.*[197] performed a theoretical study to determine λ_d for the interaction of He^+ ions with a wide range of elemental targets. In their work, Ramachandra *et al.* found that the value for λ_d typically fell within a range of 0.75-1.2 nm. SEs generated by the He^+ ion beam thus escape from a shallow region with an area not much greater than the size of the probe. For an electron-beam exposure, SE2s can be generated some distance away from the incident probe. Consequently, in EBL one can expect resist exposure over an area greater than the area of the probe.[149,161]

A PSF describes the response of an imaging system to a point source of radiation. In the case of HIBL and EBL, the PSF describes how energy from the incident beam is distributed laterally in the resist.[171,205] An accurate description of the PSF for HIBL and EBL is of particular importance for the fabrication of dense arrays of nanostructures. As mentioned previously, overlapping dose tails of neighbouring point exposures can result in unwanted exposure of regions between directly exposed features. Thus, an accurate

description of the PSF can determine how closely structures can be printed and resolved, and can also be used to calculate corrections for the local dose when patterning smaller features.[207,208]

3.1.3 Fabrication on Ultra-Thin Membranes

In recent decades, nanofabrication on freestanding ultrathin membranes has gained significant interest. The ability to fabricate nanostructures on ultrathin membranes with control over size, shape and position on the nanometre length scale is key to a variety of emerging research fields such as matter wave optics for studying foundations of quantum physics, plasmonics, nanopore sensors for DNA sequencing and molecule detection, and mask-based matter wave lithography.[209–214] Fabrication of nanostructures and nanoscale devices on ultrathin membranes enables characterization of these materials and devices with atomic scale resolution by (scanning) transmission electron microscopy ((S)TEM) techniques including atomically-resolved imaging, electron energy-loss spectroscopy and energy-dispersive x-ray analysis. TEM techniques are important for the development of plasmonic nanostructures,[215,216] nanoelectronic devices,[217] quantum devices,[218,219] nanopores for DNA sequencing[220] and enable characterization of nanomaterials such as catalysts at close to the atomic scale.[221] To date, TEM has been used to directly visualise the interaction volume resulting from a spot irradiation of a He^+ beam on a hydrogen silsesquioxane (HSQ) resist supported by a 20-nm-thick SiN_x membrane.[222,223] To our knowledge, similar work using PMMA as a resist has not been conducted, nor has a direct comparison to high-resolution aberration-corrected EBL.

Fabrication on ultrathin membranes reduces scattering of ions or electrons by the substrate, thus reducing the proximity effect and allowing for higher lithographic resolution. EBL has been performed previously on ultrathin membranes using aberration-corrected STEM.[136,159,205] A high beam energy of $\sim$ 200 keV results in reduced scattering angles for the transmitted electrons, leading to a reduced proximity effect.[159] A spot size of 0.15 nm has been achieved previously for aberration-corrected EBL,[159] compared to the spot size of 0.25 nm achievable in HIBL mentioned previously.[147] The advanced optics of aberration-corrected STEM, as well as the use of an ultrathin membrane, minimises

scattering in the resist-substrate stack. This approach has been used to determine the ultimate resolution of EBL.[136,159,205] Ultrathin membranes are also of benefit for HIBL because in addition to reduced scattering due to a thinner substrate, most He^+ ions that become embedded in the sample do so at a depth of >100 nm below the surface of the sample.[224] Consequently, by fabricating features on a thin substrate, damage caused by helium accumulation in the substrate can be avoided, and SE generation in the substrate can be minimised. This should further reduce the proximity effect, and help reduce any defects in fabrication caused by damage to the sample, potentially allowing for the ultimate resolution of HIBL to be explored. Here, we compare the resolution limits of HIBL with a PMMA resist on a freestanding ultrathin membrane to previous reports of the resolution limits of aberration-corrected EBL.[136,205]

3.1.4 HIBL Resists

PMMA is a popular EBL resist and is also often used as a resist for HIBL. At lower beam doses, fragmentation of the polymer chain dominates and PMMA operates as a positive-tone resist. As the dose is increased cross-linking of the polymer chains dominates and PMMA acts as a negative-tone resist. Shi *et al.,* found that for positive-tone PMMA with a molecular weight of 4.95×10^5 g/mol the sensitivity to HIBL exposure was 60 times greater than the sensitivity to EBL exposure.[225] Furthermore, the authors determined that the range of backscattered He^+ ions was 67.1 nm compared to 3.26 μm for backscattered electrons, indicating that proximity effects would be greatly reduced in PMMA exposed with a He^+ ion beam. The sensitivity of negative-tone PMMA to HIBL has been reported as 68 $\mu C/cm^2$ whereas the sensitivity to EBL has been reported as 5.8 mC/cm^2.[168,226]

In recent years, molecular based resists, in particular fullerene derivatives, have gained attention as a new family of resists for charged particle lithography.[1,227] Rao *et al.,* found that irradiating fullerene C_{60} films with visible or ultraviolet light resulted in cross-linking between molecules in the film and a reduction in solubility in toluene.[228] Tada *et al.,* were the first to describe the use of a fullerene as an electron beam resist, and recently there has been a push to develop a new class of negative-tone fullerene-based molecular re-

sists.[1,227,229] The exposure mechanism of fullerene derivatives is thought to involve the fragmentation of the fullerene cage, followed by cross-linking of the remaining fragments to form an insoluble deposit. The small molecular size of these resists ($\sim$ 0.7 nm) leads to the expectation that the fragmentation of the resist during exposure will yield smaller feature sizes and reduced line edge roughness (LER).[1] To date, sub-10 nm features have been achieved in fullerene derivative resists using HIBL.[1,182] Furthermore, owing to their high carbon content, non-chemically amplified fullerene derivative resists have demonstrated high etch resistance.[183] Fullerene derivatives are therefore an attractive candidate for next generation lithography processes.

In this work, we calculate the PSF for both PMMA and a fullerene molecular resist on thin SiN_x membranes (5 nm), and compare the calculated PSFs to experimental results. Winston *et al.* developed a model to calculate the HIBL PSF for HSQ on a bulk silicon substrate.[196] In the model, the simulation software *Stopping and Range of Ions in Matter* (SRIM), developed by Ziegler *et al.* is first used to simulate the trajectories of incident ions in a target sample.[230] A schematic depicting the interaction of these incident He^+ ion beam with the sample is shown in Figure 3.1. The incident beam is scattered at random scattering sites. The initial position, direction, and energy of SEs generated by the incident ions are determined using a Poisson process that traces along the He^+ ion trajectories.[231,232] The SE trajectories were calculated using a Monte Carlo method developed previously for EBL.[232] Finally, the model returns the spatial distribution of energy deposited into the sample.

3.2 Experimental

1 wt.$\%$ 950k molecular weight PMMA in anisole (purchased from *EM Resist Ltd.*) and a fullerene-derivative resist (supplied by *Irresistible Materials Ltd.* were spin coated (resist thickness $\sim$ 15 nm) onto ultrathin SiN_x membranes (5-nm-thick SiN_x membranes were purchased from *SiMPore Inc.* via *TEMwindows.com*). Experimental PSFs were measured by exposing square arrays of single-pixel exposures at various ion doses using a pitch of 100 nm. Exposures were performed using a *Zeiss Orion NanoFab* with a He^+

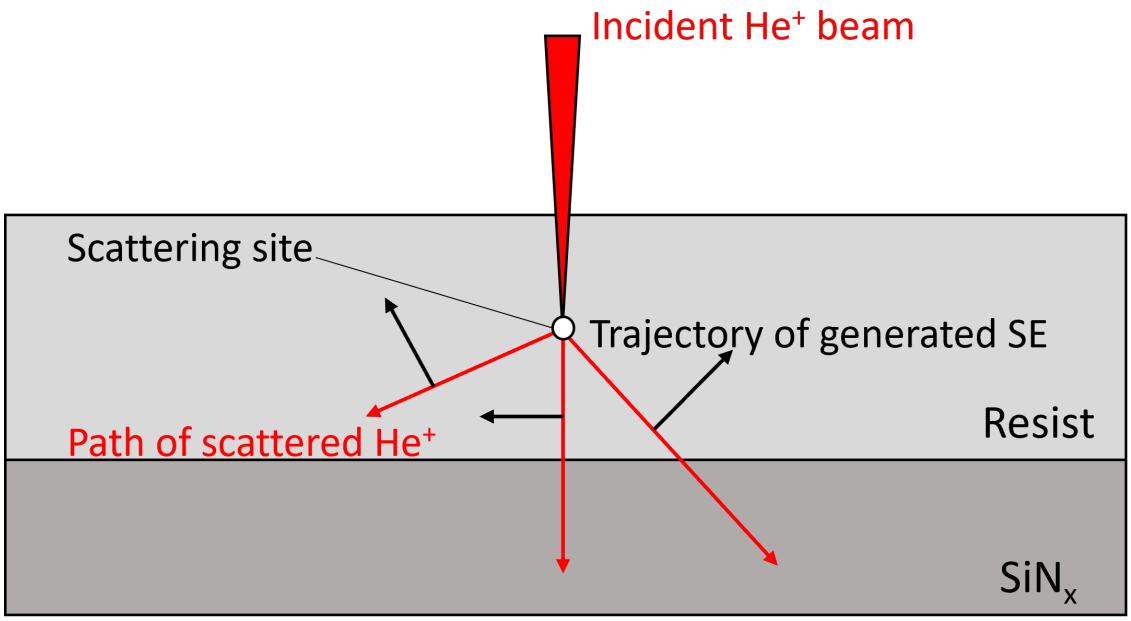

Figure 3.1: Schematic of interaction of He^+ ion beam with the sample. Red arrows indicate the path of scattered He^+ ions. Black arrows indicate the trajectories of SEs generated by He^+ ions. The beam is scattered in various directions by the sample. SEs are generated with paths perpendicular to the beam at points along the path of a He^+ ion.

ion landing energy of 30 keV. Point exposures were made within a 50 µm writefield using a *Raith Elphy Multibeam* pattern generator. Typical experiments used a beam current of 0.3-1.0 pA, 5 µm aperture, spot number of 4, working distance of 8 mm and a helium pressure of 2×10^{-6} Torr. Ion dose per pixel was varied as shown in the PSF plots included in Figure 3.4. Samples were developed by immersion in acetone followed by a rinse in isopropyl alcohol. Exposed structures were characterized by scanning electron microscopy (*Zeiss Supra 40*) and bright-field transmission electron microscopy (*JEOL 2100* operating at 200 keV). A full description of the simulation methods used to calculate the PSF is given by Winston *et al.*[196] In order to calculate the PSF, the escape depth, λ_d, the effective energy required to produce an SE, ϵ, the density, ρ, for both the resist and substrate, and the energy and number of the incident He^+ ions must be specified. Ramachandra *et al.*[197] performed simulations to calculate these parameters for a wide range of elements. The values used to calculate the PSF for PMMA are λ_d = 10.8 Å and ϵ = 59 eV. These are the values the authors calculated for elemental carbon, and were selected as there is no data available for PMMA or elemental hydrogen or oxygen. Densities of 1.18 g/cm^3, 1 g/cm^3, and 3.17 g/cm^3 were used for PMMA, the fullerene-

derivative resist, and SiN_x respectively. As no data could be found for the fullerene-derivative resist, data for fullerenol from Vraneš *et al.* was used as this molecule is similar to the fullerene-derivative resist.[198] The energy of the He^+ ions was set as 30 keV, and the number of ions was 100,000.

3.3 Results and Discussion

3.3.1 Negative-tone Structures Fabricated on Ultra-Thin Membranes

TEM images of negative-tone PMMA and fullerene-derivative structures fabricated via He^+ exposure are shown in Figure 3.2. Multiple arrays were fabricated with different pitches and exposure doses. The smallest resolvable negative-tone PMMA features were fabricated using a dose of 5.5 aC and had a radius of 3.2 $\pm$ 0.2 nm, as shown in Figure 3.2(a). Figure 3.2(b) shows a lower magnification image of an array of point exposures exposed with a high dose of 10 fC. The radius of the smallest resolvable negative-tone fullerene-derivative features was measured to be 2.7 nm $\pm$ 0.4 nm. The thickness of the resist films used during these exposures was estimated by measuring the thickness of collapsed negative-tone structures. The lowest dose that yielded observable negative-tone PMMA structures was 5.5 aC. For a point exposure with a beam current of 0.5 pA this corresponds to an exposure time of 11 µs *i.e.,* shorter than the time scale that any effects of drift would be observable. For doses in this range the resulting structures are expected to be circular in shape. As the average diameter of structures exposed at this dose is 6.4 nm and the resist thickness is expected to be $>$ 10 nm, oblong shaped structures are assumed to have collapsed. Therefore, by measuring the major axis of these collapsed structures the resist thickness can be estimated. Examples of collapsed structures for both resists are shown in Figure 3.3. The thickness of the PMMA resist was found to be approximately 15 nm and the thickness of the fullerene-derivative resist was found to be approximately 16.5 nm when measured using this method.

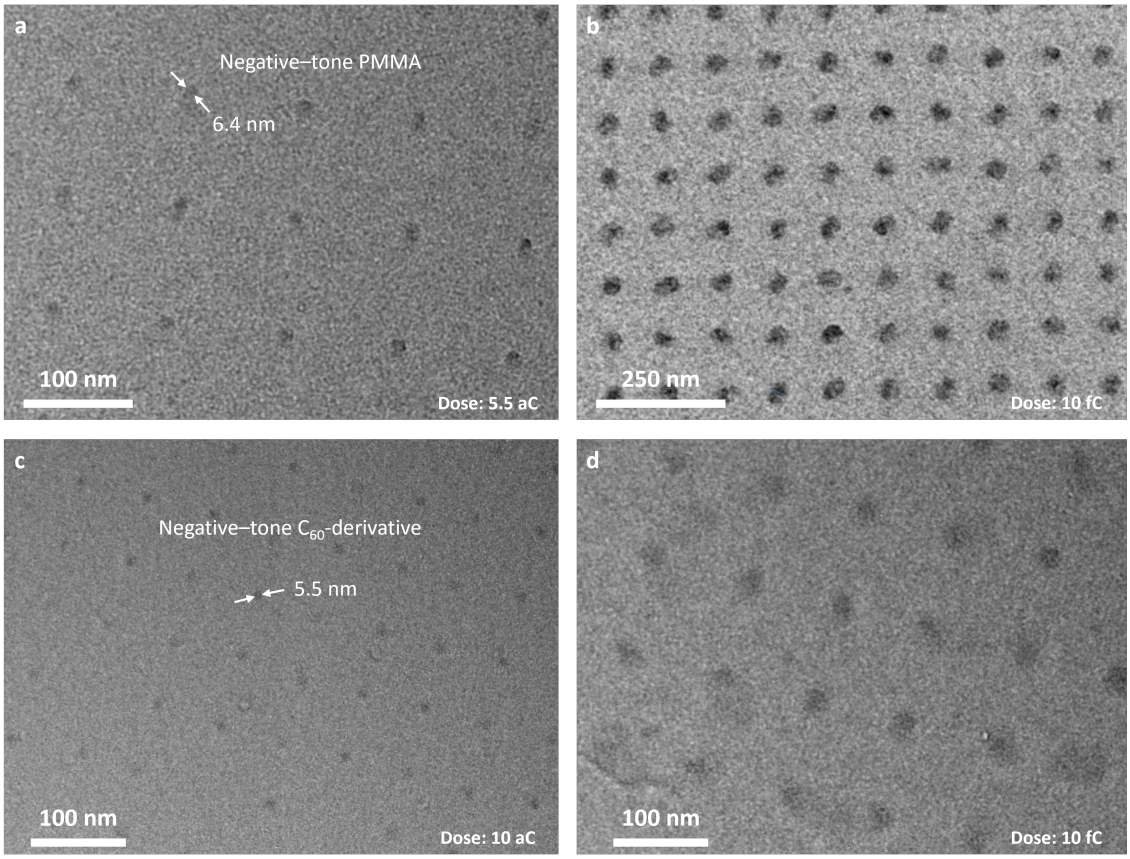

Figure 3.2: (a) TEM micrograph of smallest resolvable negative-tone PMMA structures fabricated with a dose of 5.5 aC. The mean radius of the structures was measured as 3.2 ± 0.2 nm. (b) TEM micrograph of negative-tone PMMA structures fabricated with a dose of 10 fC. (c) TEM micrograph of smallest resolvable negative-tone fullerene-derivative structures fabricated with a dose of 10 aC. The mean radius of the structures was measured as 2.7 ± 0.4nm. (d) TEM micrograph of negative-tone fullerene-derivative structures fabricated with a dose of 10 fC. A pitch of 100 nm was used for all exposures.

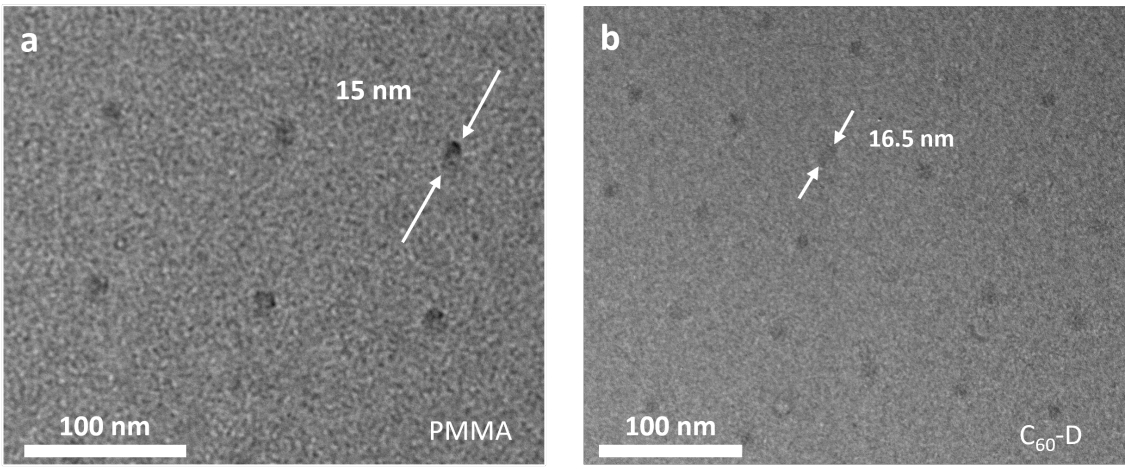

Figure 3.3: Measurement of the thickness of the (a) PMMA and (b) fullerene-derivative resists. The oblong shape of the highlighted structure indicates that it has collapsed and therefore the thickness of the film can be determined by measuring its length.

3.3.2 Determination of PSF

The experimentally measured He^+ PSFs for both PMMA and a fullerene-derivative resist are shown in Figure 3.4 alongside the calculated PSF for each resist. The simulation was scaled to the experimental data by equating data points with $r \sim 12.5$ nm for PMMA and $r \sim 13$ nm for the fullerene resist, as there is a trade-off between experimental uncertainty and statistical uncertainty in the simulation for features of this size as per Winston *et. al.*[196] It can be seen from Figure 3.4, that the calculated results match well with experiment for both resists. The fitting function below was adapted from the function developed by Winston *et al.* for their simulated data to fit our results:

$$PSF(r) = A((\frac{1}{\sigma_1^2})e^{-(\frac{r}{\sigma_1})^2} + \eta(\frac{1}{\sigma_2^2})e^{-(\frac{r}{\sigma_2})^2}) + Be^{-\frac{r}{r_e}} + C\sqrt{\frac{1}{1+(\frac{r}{r_f})^p}}, \tag{3.1}$$

where r is the radius of the feature produced by a given dose. In this expression, σ_1 indicates the beam spot size and lateral extent of forward scattering, and σ_2 represents the lateral extent of backscattering. The exponential term may indicate Beer-Lambert-like absorption of SEs with r_e as the mean free path as has previously been reported.[196] The final term is a filter function featuring a threshold radial value, r_f. When r is less than r_f, the square root in this term has a value near 1. Consequently, the filter function term effectively sets a minimum exposure dose equivalent in value to *C*, below which

	A	σ_1	η	σ_2	B	r_e	C	r_f	p
PMMA	8×10^4	0.7 nm	0.02	75 nm	2×10^4	0.6 nm	2000	0.5 nm	4
Fullerene-derivative	4500	0.7 nm	0.02	40 nm	8000	0.5 nm	100	0.5 nm	5

Table 3.1: Parameters for Equation 3.1. for both PMMA and Fullerene-derivative.

lithographic exposure is not produced. When r exceeds r_f, the value of this function drops off, scaling with a power-dependence defined by the exponential term, p, in the denominator. Table 1 shows the parameter values for Equation 3.1 for both PMMA and the fullerene-derivative.

It can be seen from Figure 3.4 that the inverse dose required for exposure is predicted by the model used here to increase rapidly as the feature size drops below approximately 3 nm for both resists. The exposure of features on these short length scales is driven by short-range secondary electrons.[233,234] It is difficult to accurately model the contribution of these short-range SEs as they do not leave the sample by definition. It is possible that smaller feature sizes are achievable, but are not seen here due to the thickness of the resist layer. As exposure by He^+ ions is highly surface sensitive, it is possible that for low doses, the region near the surface of the resist layer is receiving enough dose to allow for sufficient cross-linking to form negative-tone structures, but that this exposure does not extend fully through the resist layer. Consequently, when the unexposed resist is removed, these features are washed away. The thickness of each resist was found to be $\sim$ 15 nm. It is possible that with the use of a thinner resist layer smaller feature sizes could be achieved, however, we were unable to generate uniform films with thickness below 10 nm in this work.

3.3.3 Comparison of HIBL to Aberration-Corrected EBL

The experimental data was also fitted to a filter function given below, per previous work by Manfrinato *et al.*[136]

$$PSF(r) = A\sqrt{\frac{1}{1+(\frac{r}{r_f})^b}} \tag{3.2}$$

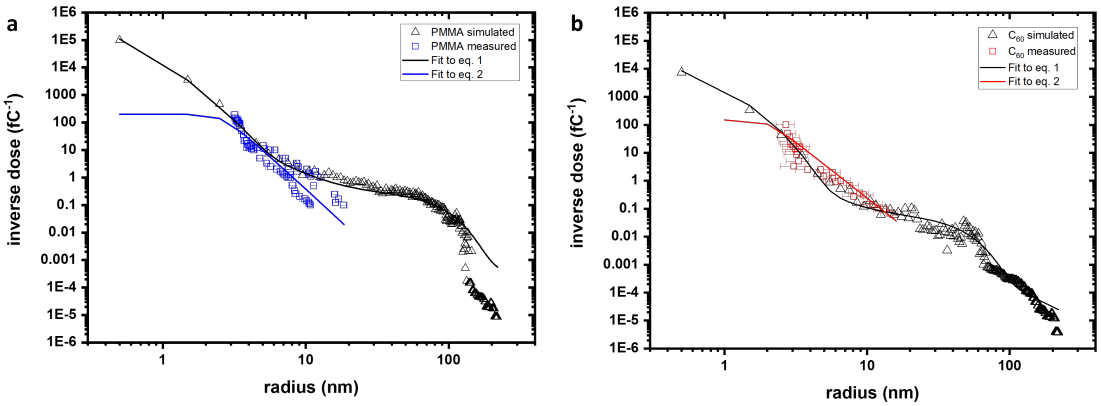

Figure 3.4: Experimental and simulated PSFs for (a) PMMA and (b) a fullerene-derivative resist on SiN_x, as well as the calculated fitting function to the simulation, and a fit to the experimental data using just a low-pass filter function. The multi-term fitting function was scaled to the experimental data by equating data points with $r \sim 12.5$ nm for PMMA and $r \sim 13$ nm for the fullerene-derivative resist. (a) Open blue square data points represent measured radii of the negative-tone PMMA dots exposed by HIBL. Open black triangular data points represent calculated radii of negative-tone PMMA dots. The black line represents the function that has been fitted to the simulated data. The blue line represents the filter function in Equation 3.2 fitted to the measured data with r_f = 3 nm. (b) Open red square data points represent measured radii of the negative-tone fullerene-derivative resist dots exposed by HIBL. Open black triangular data points represent calculated radii of negative-tone fullerene-derivative resist dots. The black line represents the function that has been fitted to the simulated data. The blue line represents the filter function in Equation 3.2 fitted to the measured data with r_f = 2 nm.

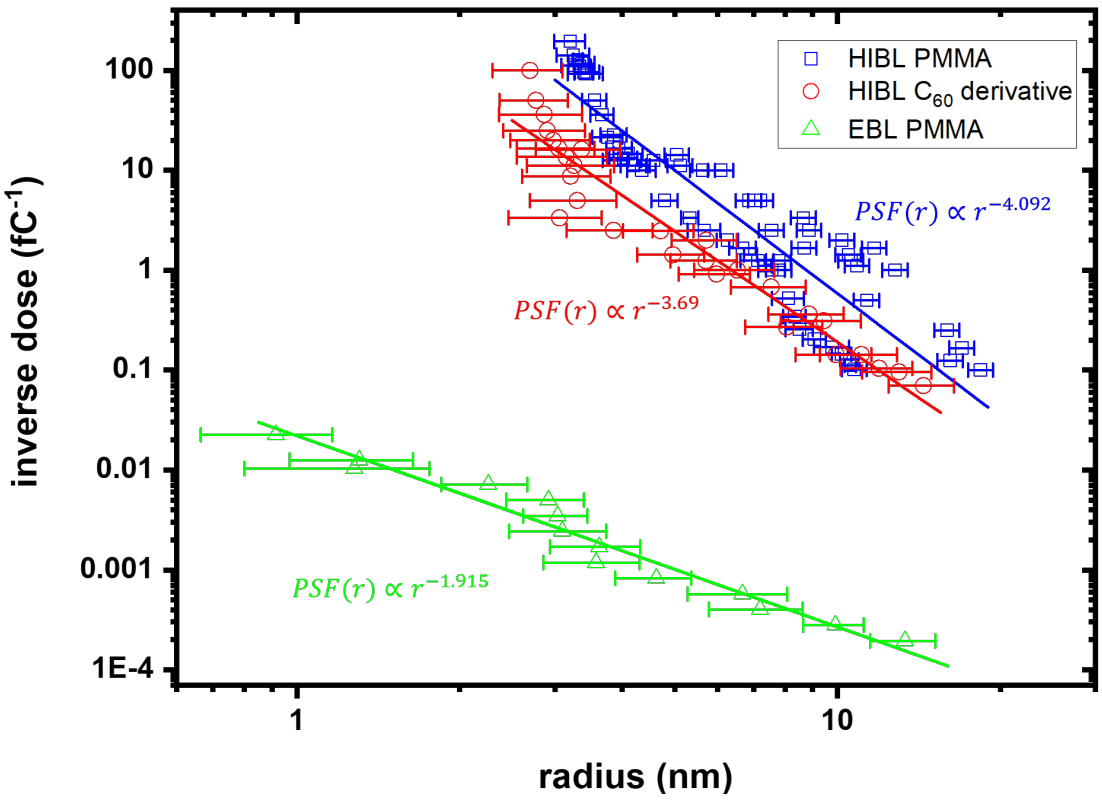

Figure 3.5: Comparison between experimental data from this work using helium-ion beam lithography and experimental data from the work of Manfrinato *et al.* using an aberration corrected STEM to perform electron-beam lithography. The fitting lines represent a power law fitted to each PSF.

The value of A is related to the lowest dose at which features are formed, while the value of r_f is the radius of the PSF and is related to smallest feature size that can be formed. The single term fitting function in Equation 3.2 is believed to be a better choice for this data than the multi-term function in Equation 3.1 as it provides a good fit to the experimental data while also being much simpler than Equation 3.1. As shown in Figure 3.4, Equation 3.1 implies that as doses get infinitely small, the minimum feature size also get infinitely small. Equation 3.2 allows a threshold dose and minimum feature size to be defined, which is more representative of what is observed experimentally. Using this function also allows us to compare our results for each resist directly with each other as well as the results from the aberration-corrected EBL work.[136]

Figure 3.5 compares the experimental data from this work and from the work by Manfrinato *et al.*[136] carried out on a similar PMMA-SiN$_x$ system, using an aberration corrected STEM. In their work, the smallest negative-tone PMMA structures fabricated

had a radius of 0.85 nm, while the smallest pitch obtained for negative-tone PMMA structures was 10.7 nm. An accelerating voltage of 200 keV was used, and the dose required to pattern the smallest features presented was approximately 100 fC. In contrast, the dose to pattern the smallest feature sizes observed had radii of 3.2 nm for PMMA and 2.7 nm for the fullerene-derivative with doses of 0.005 fC and 0.01 fC respectively. This corresponds to almost a 20,000 times difference in the sensitivity between a 30 keV He^+ ion beam and a 200 keV electron beam. For He^+ ion and electron exposures on PMMA at 30 keV, a sensitivity gain of 116 for He^+ ions has been previously reported.[226] In the EBL work, an accelerating voltage of 200 keV was used so a dose that is approximately 200/30 times higher would be expected. The additional difference in sensitivity we report here may arise because here we are comparing point exposures on ultrathin membranes, as opposed to area exposures on bulk substrates.

A PSF with a large negative slope indicates that the energy deposited in the resist falls off very quickly as the radial distance from the point of exposure increases *i.e.,* there is a reduced proximity effect. Consequently, there will be greater dose contrast between two closely-spaced structures. It can be seen from Figure 3.5 that the PSF for PMMA exposed by HIBL is slightly steeper than that of the fullerene-derivative, indicating that PMMA may be a better choice for the patterning dense arrays of nanostructures. However, the fullerene-derivative was able to produce smaller features than PMMA which is an obvious advantage for a next generation lithography resist. Fullerene also required a larger dose than PMMA to produce features with the same radius. This is a further advantage because as we move to lower doses to try produce the smallest features, shot noise can become an issue for consistent fabrication at low doses. The higher doses required for the fullerene-derivative will help to mitigate some of the problems introduced by patterning at very low doses. When comparing to the data from the aberration-corrected EBL work, it can be seen that both resists exposed with a He^+ ion beam have significantly steeper slopes than the corresponding PSF for the electron-beam exposure on PMMA. At present, there are no dedicated HIBL tools in production, but the results here indicate that HIBL supports high density pattern formation and that it may outperform EBL at ultra high densities.

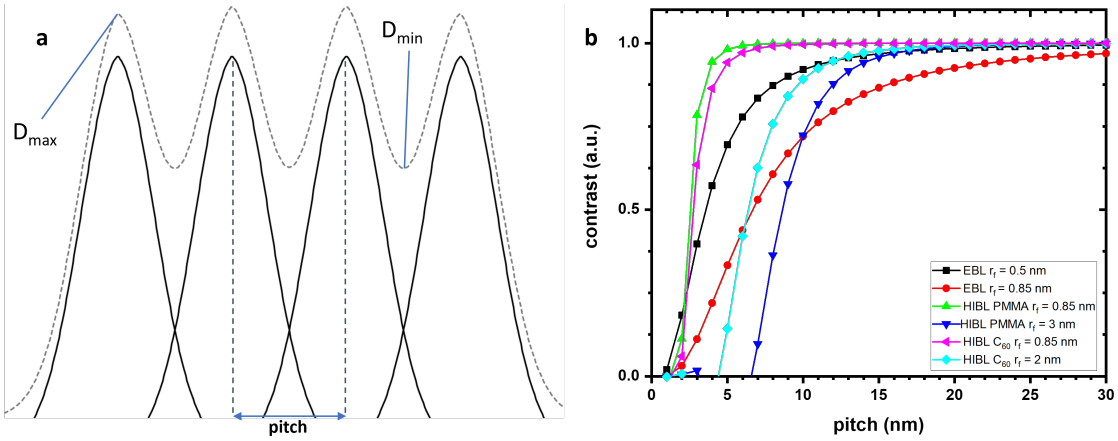

Figure 3.6: (a) To calculate dose contrast the PSF was used to generate an array of point exposures with a given pitch within a 2 µm × 2 µm area. The dose at any given point is equivalent to the sum of all doses from each point exposure. D_{max} is the total dose experienced at the centre of a single point exposure. D_{min} is the total dose experienced at a point that is equidistant between two independent dose exposures. (b) Plots of dose contrast versus pitch for PMMA on SiN_x calculated using the PSF predicted by Equation 3.2 for different values of r_f.

3.3.4 Dose Contrast

Figure 3.6 shows the dose contrast as a function of exposure pitch, calculated using Equation 3.3 below, for the experimental PSF. Dose contrast, *K*, is defined as:

$$K = \frac{D_{max} - D_{min}}{D_{max} + D_{min},} \tag{3.3}$$

where D_{max} is the dose delivered to the centre of an individual spot in a square array of point exposures, and D_{min} is the dose delivered to a point midway between two spots in the array, as shown in Figure 3.6(a). Dose contrast provides information about how close to one another features can be fabricated. In order to calculate the dose contrast a MATLAB script was written that first defines a 2 µm × 2 µm writefield consisting of point exposures with a specified pitch. The total dose is calculated at the centre of one point exposure (D_{max}) and at a point midway two point exposures (D_{min}) by evaluating the sum of all PSFs for each point exposure in the array at these locations. Dose contrast, *K*, can then be calculated using Equation 3.3. A plot of dose contrast versus pitch is shown in Figure 3.6(b). In the ideal scenario where *K* = 1, the region between two point exposures receives a dose of zero, so both structures can be fabricated with no unwanted

indirect exposure of the region between the structures. A value of K = 0 corresponds to zero dose contrast whereby D_{max} is equal to D_{min}. The region is overexposed, and thus no structures will be resolved. The true value of the radius of the PSF, r_f, is unknown so here we show the expected contrast for a range of values of r_f. The radius of the incident beam is assumed to be $\sim$ 0.25 nm,[148] however the smallest feature fabricated has a radius of 3.2 $\pm$ 0.2 nm for PMMA and 2.7 nm for the fullerene-derivative. This indicates that for an exposure with sufficient dose to fabricate a negative-tone feature, the energy deposited by the beam into the resist has a lateral spread that is significantly larger than the radius of the beam. Consequently, it is expected that the value of r_f is larger than the radius of the beam. The values of r_f used to generated the curves in Figure 3.6 were 3 nm for PMMA and 2 nm for the fullerene-derivative. These values were used as they are near to the size of the smallest feature produced for each resist and also provided good fits to the experimental data. The results from the aberration-corrected EBL indicate that for all pitches aberration-corrected EBL outperforms HIBL, for these values of r_f. In the case for the aberration-corrected EBL a beam radius of 0.1 nm was measured, and the smallest feature size produced was 0.85 nm[136] so it can be expected that the radius of the PSF in this case would be lower than the radius for the PSF of the He^+ beam in this work. For further comparison we have calculated the dose contrast for the aberration-corrected EBL system using a value of 0.85 nm for r_f as this is the smallest radius fabricated using this system. Further improvement to HIBL systems could result in smaller features being produced, thus lowering the value for r_f. In Figure 3.6(b) we have also included contrast curves for both PMMA and the fullerene-derivative with r_f set to 0.85 nm. Superior contrast than aberration-corrected EBL with $r_f = 0.5$ nm is expected for arrays with pitch down to 2 nm for both PMMA and the fullerene-derivative. Compared to aberration-corrected EBL with $r_f = 0.85$ nm, HIBL is predicted to yield superior contrast for all pitches below for both resists. To date, HIBL has been used to fabricate arrays of nanostructures with pitches as low as 8 nm.[235] The results presented here suggest that HIBL can be further improved to fabricate denser arrays of structures than those previously reported.

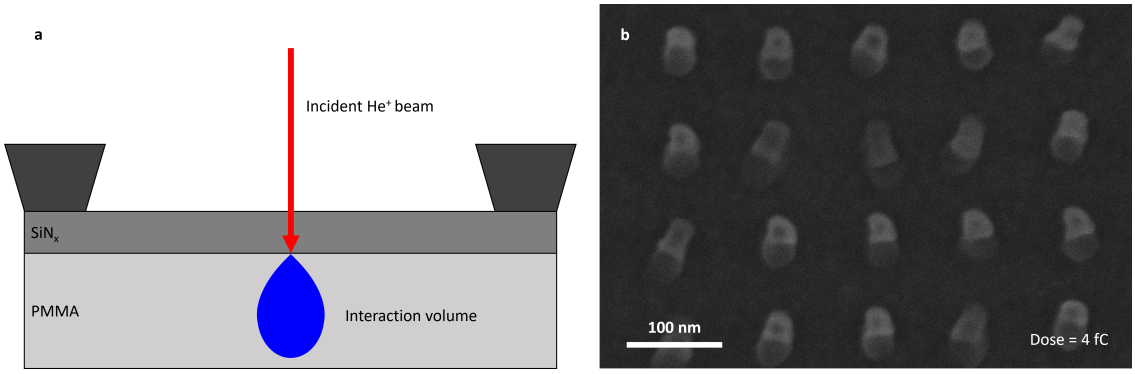

Figure 3.7: (a) Schematic showing the He^+ beam exposure of a resist film through the backside of an ultrathin membrane in order to directly image the interaction volume of the beam with the resist. (b) SEM micrograph of negative-tone PMMA structures exposed through the backside of the ultrathin membrane. The exposure dose was 4 fC and the pitch between exposures was 100 nm.

3.3.5 Direct Imaging of PMMA Interaction Volume

It is possible to directly image the interaction volume of an electron or ion beam with a resist by inverting the ultrathin membrane when placing it into the microscope and exposing the resist from the backside of the membrane as shown in Figure 3.7(a). To date, this method has been used to measure the He^+ ion interaction with HSQ.[222,223] Here, we present some preliminary results of the direct measurement of the interaction volume of the He^+ beam with PMMA.

From the SEM image in Figure 3.7(b) it can be seen that the interaction volume resembles the 'teardrop' shape that is expected and has been reported for the interaction volume of HSQ.[222,223] The structures appear to be collapsed, but this could not be confirmed via tilting the sample, as tilting the sample requires increasing the working distance and had a significantly reduced the resolution of the image. The brighter sections seen in the majority of the exposed structures indicates regions of thicker PMMA. This could occur due to partial collapse of the structures back onto the themselves. The resist thickness was therefore measured from a structure lacking in particularly bright features and was found to be 75 nm. An important observation is the significant increase in width of the interaction volume as the beam penetrates the resist. This highlights the advantages of patterning thin resist layers on ultrathin substrates to reduce the scattering of the beam by the resist and substrate.

3.4 Conclusions and Outlook

In conclusion, the PSF for the interaction of 30 keV He^+ ions with PMMA and a fullerene-derivative resist on an ultrathin membrane was calculated and measured experimentally. The model used by Winston *et al.*[196] was modified for thin layers of PMMA and a fullerene-derivative on an ultrathin SiN_x membrane and the resulting PSF was found to agree well with the experimental PSF that was measured. The fullerene-derivative yielded a minimum feature radius of 2.7 nm compared to 3.2 nm for PMMA, while also requiring higher doses, indicating that the fullerene-derivative could be a better choice as a next generation lithographic resist. The experimental results were compared to previous work using state-of-the-art aberration-correction electron beam lithography using the same type of resist and membrane. It was found that exposure of PMMA with 30 keV He^+ ions had a sensitivity approximately 20,000 times greater than exposure with 200 keV electrons. Dose contrast calculations predict that for He^+ ion exposure with a PSF radius of 0.85 nm superior contrast is achievable down to a pitch of 2 nm for both PMMA and a fullerene-derivative when compared to a similar exposure using an aberration-corrected electron beam with a PSF radius of 0.5 nm. When compared to an aberration-corrected EBL process with a PSF radius of 0.85 nm, it was found that HIBL predicts superior contrast for all array pitches. As the He^+ ion setup is also far simpler than the aberration-corrected electron-beam setup, we propose that, going forward, HIBL is a superior choice to EBL for the patterning of dense arrays of nanostructures.

A drawback of this method of measuring the interaction of the beam with the resist is that there will always be some information about the lateral spread of the beam into the resist lost during the development step. The advent of techniques such as AFM-IR could allow for the measurement of lateral spread of energy deposited by the beam into the resist without the need for development.[236,237] For example, negative-tone PMMA possesses a graphitic carbon quality that is not present in the unexposed resist. By monitoring the spatial distribution of an IR mode associated with graphitic carbon using AFM-IR, a direct map of the exposed region of the resist could be made without losing any information during the development step, yielding more accurate PSFs and subsequently allowing for more accurate proximity effect corrects during patterning. Furthermore, by

exposing resist films with varying thicknesses and measuring the lateral spread of beam energy at each thickness with AFM-IR a 3-D model of the interaction volume of the beam with the resist could be built, while reducing problems that occur due to resist collapse, or further exposure of the resist while imaging with the electron beam.

Chapter 4

Plasmonic Nanoantennas for Strong Coupling to Molecular Vibrational Modes and Surface Enhanced Raman Spectroscopy

4.1 Introduction

There has been much interest recently in the use of plasmonic materials in the formation of coupled systems with quantum emitters (QEs) and molecules with the aim of enhancing light-matter interactions.[21,31,33,238–240] Coupled systems are described as either weakly coupled or strongly coupled. The weak coupling regime is typically characterised by an enhancement in the emission rate of an emitter with little change to the resonance frequency.[27,28] The modification of the emission properties of a QE via weak coupling has exciting applications in improved photodetection devices as well as potentially paving the way for single-photon emitter devices.[37,241,242] In the strong coupling regime there is a periodic energy transfer between the QE or molecule and the plasmonic resonator, and it is characterised by the formation of hybrid modes with a frequency changed from the resonant frequency. Applications of the strong coupling between QEs and plasmonic res-

onators include fully optical devices, as well as quantum information processing.[31,243,244] Here, we focus on the strong coupling between molecular vibration and plasmonic cavities.

4.1.1 Underlying Physics

By matching the frequency of the LSPR to an electronic transition in a QE or a vibrational mode in a molecule and placing the QE or molecule in close proximity to a plasmonic resonator *e.g.* in the gap of a plasmonic bowtie, a coupled system can be formed. The strength of the coupling is determined by the Rabi frequency:

$$\Omega_{\mathrm{R}} = \mu E_{\mathrm{LSPR}} = 2\mu\sqrt{\frac{\hbar\omega}{2\epsilon_0 V_0}}, \tag{4.1}$$

where μ is the transition dipole moment of the QE or molecule, E_{LSPR} is the LSPR field strength, ω is the frequency of the transition, ϵ_0 is the permittivity of free space, and V_0 is the mode volume of the plasmonic cavity. The system is weakly coupled when $\Omega_R^2 \leq \frac{\gamma_{QE}^2}{2} + \frac{\gamma_{LSPR}^2}{2}$. The system is strongly coupled when $\Omega_R^2 \geq \frac{\gamma_{QE}^2}{2} + \frac{\gamma_{LSPR}^2}{2}$, where γ_{QE} and γ_{LSPR} are the dephasing rates of the QE and LSPR respectively.[25,26] The strong coupling of a plasmonic cavity and a vibrational mode in a molecule results in the formation of hybrid energy levels, thereby altering energy of the coupled bond. This change in bond energy changes the bond strength and therefore can modify the potential energy landscape of reactions involving the bond, paving the way for new pathways in chemical catalysis.[238]

Here we aim to design and fabricate plasmonic antennas capable of supporting two discrete modes; one designed to match with the frequency of a molecular vibration, and the other designed to match with the frequency of a laser to allow for the coupled system to be probed via SERS.

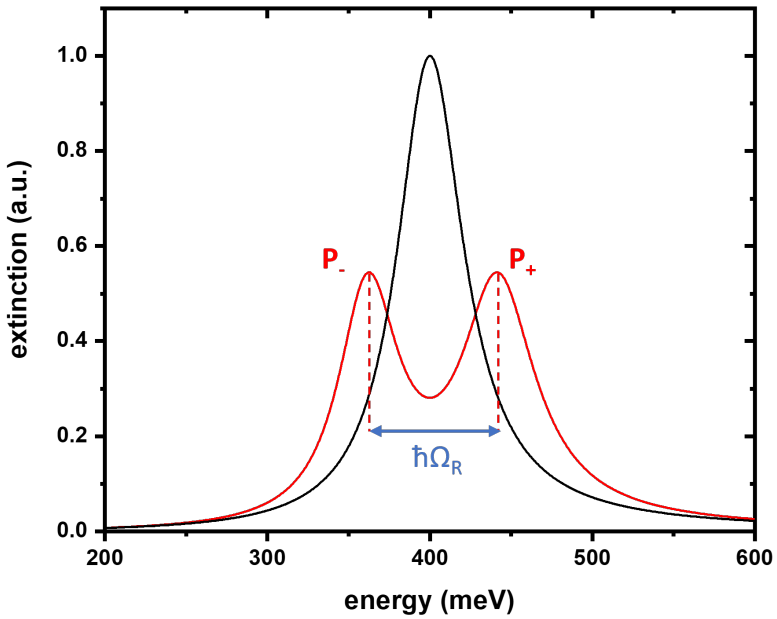

Figure 4.1: Simulated extinction spectrum of a strongly coupled system. The black line shows the extinction spectrum of a plasmonic resonator with a resonance at 400 meV. The red line shows the extinction spectrum of the coupled system with two peaks representing the lower (P_-) and upper (P_+) polaritons separated by the Rabi splitting energy $\hbar\Omega_R$.

4.1.2 Strong Coupling of Photonic Cavities to Molecular Vibrations

By placing a molecule within a photonic cavity, it is possible for a vibrational mode of the molecule to couple with one of the cavity modes as shown in Figure 4.2. As the wavelength of the cavity modes is dependent on the size of the cavity, L, the cavity modes can be tuned to match a desired molecular vibration. In the case of strong coupling between a molecule and photonic cavity, two hybrid modes can be observed, which are referred to as the upper polariton, P^+, and lower polariton, P^-. The strength of the coupling is dependent on the energy of the splitting of these hybrid modes given by $\hbar\Omega$, where Ω is known as the Rabi frequency. This coupling can be observed in the absorption spectrum of the system. The single peak representing the cavity and molecular resonance will split into two peaks separated by the Rabi frequency. These hybrid modes are of great interest because the formation of these hybrid modes indicates that the energy of the coupled bond has been modified, and therefore the reactivity of the molecule can be adjusted. Furthermore, these hybrid modes occur in the dark *i.e.,* in the absence of any excitation, and the coupling is reversible by simply removing the molecule from the

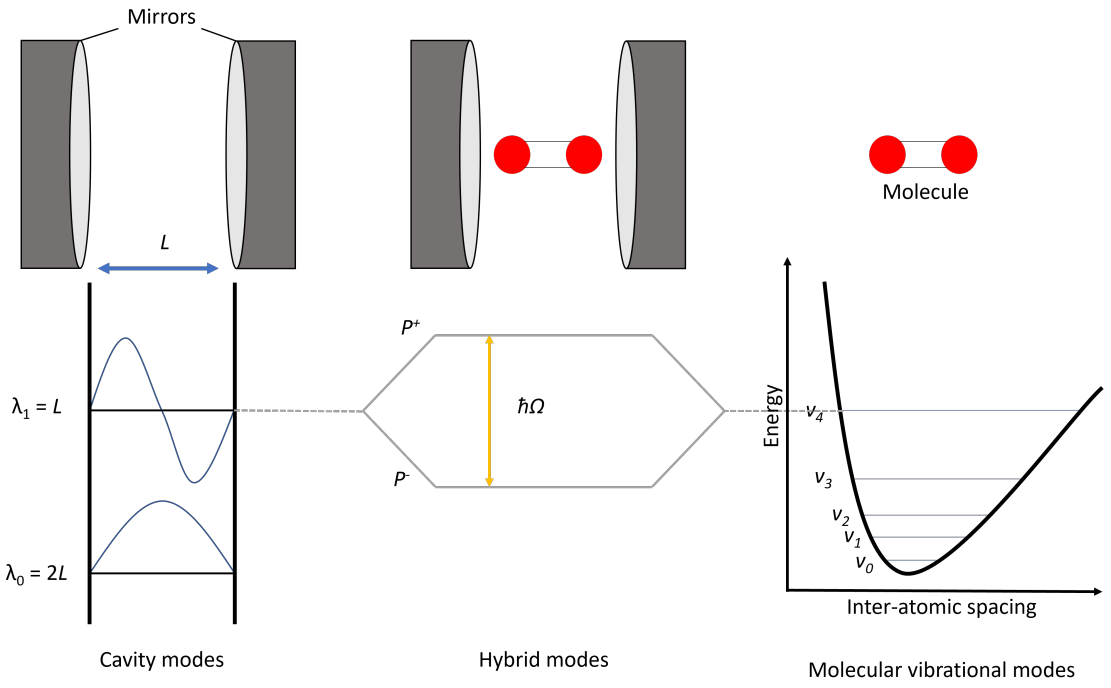

Figure 4.2: Schematic showing the strong coupling of a photonic cavity with a vibrational mode in a molecule. The strong coupling results in the formation of two hybrid polariton modes separated by $\hbar\Omega$.

cavity.

The first reported instance of the modification of ground-state chemistry via vibrational strong coupling (VSC) was by Thomas *et al.* in 2016.[245] In this work, the Si-C bond of a 1-phenyl-2-trimethylsilyacetylene molecule was coupled to a photonic cavity and it was found that the reaction rate of the silane deprotection reaction was reduced by a factor of up to 5.5 under strong coupling. Since this breakthrough, VSC has been used to modify the reaction rate of multiple different chemical reactions. VSC has also been used to increase the selectivity of bond scission during a reaction. By coupling to either the Si-C or Si-O bond, Thomas *et al.* found that the uncoupled bond could be favourably broken under the same reaction conditions, thereby improving the selectivity of the process.[42] It has also been shown that symmetry is an important factor in VSC. Pang *et al.* found that the equilibrium constant of a charge transfer reaction between mesitylene and iodine was increased or decreased depending on the symmetry of the molecular vibration being coupled to the cavity.[246] The influence of the vibrational-mode symmetry on this reaction indicates that other symmetry-dependent reactions could be adjusted using VSC. Sau *et*

al. found that the stereoselectivity of a cyclobutene derivative ring opening reaction that follows Woodward-Hoffman symmetry selection rules could be influenced using VSC.[247] It was determined that the transition states of reactions leading to symmetry-allowed or symmetry-forbidden products could be stabilised or destabilised via strong coupling to different vibrational modes of the cyclobutene derivative.

In the aforementioned examples a Fabry-Pérot cavity was used to achieve VSC. These cavities are formed using two parallel mirrors with a gap size that can be tuned to match with a vibrational mode of a molecule. Here, we aim to fabricate a plasmonic cavity to couple with a vibrational mode. The low mode volume V_0 of plasmonic cavities make them ideal candidates for achieving strong coupling. By strongly coupling a molecule to a plasmonic cavity, the enhanced fields within the cavity when the surface plasmon is excited could pave the way to new reaction pathways not typically possible under normal conditions. To date, there has been extensive work done on the strong coupling of plasmonic cavities to quantum dots and molecular emitters.[33,240] Recently there have been several reports of VSC to propagating surface plasmons in metal films, gap surface plasmons, surface lattice resonances.[248–250] In these studies VSC was achieved by coupling to a vibrational mode in a film of PMMA. Here we aim to achieve VSC between plasmonic antennas and graphitic carbon nanodots by using electron-beam lithography to fabricate the nanodots directly in the plasmonic hot spot of the antennas.

4.1.3 Surface-Enhanced Raman Spectroscopy (SERS)

Surface-enhanced Raman spectroscopy (SERS) is a spectroscopic technique that, with careful design and control, can enable detection of single molecules in the near field of plasmonic nanostructures.[16,251] When a surface plasmon is excited, there is a localised field enhancement. Raman scattering intensity scales with the square of the incident laser intensity and as such scales with the 4th power of the optical electric field. Consequently, a factor of 10 enhancement of the local field will lead to an enhancement of the Raman scattering signal by a factor of 10^4.[16]

SERS platforms should be well-defined and reproducible, making EBL an ideal tech-

nique for fabricating these surfaces. SERS platforms should be designed so that the analyte of interest can interact with the region of enhanced optical field, should provide a large field enhancement factor to maximise sensitivity and should be stable to allow reproducible SERS signals.[252] Tabatabaei *et al.*[252] were able to show that by tuning the size of Au nanoholes, they could increase or decrease the strength of the coupling between the gold nanoholes, and 4-nitrothiophenol molecules. A SERS limit of detection of 10^{-16} M was obtained, highlighting the sensitivity of this technique.

Here we aim to fabricate plasmonic Au nanoantennas capable of supporting two distinct modes; one in the near-IR region of the spectrum and one in the mid-IR region. The NIR mode is designed support a resonance that matches with a Raman laser, allowing us to probe the system using SERS. The mid-IR mode is designed to resonate with a molecular vibration, specifically the G band peak present in graphitic C. This mode is chosen because graphitic carbon nanodots can be fabricated with precise spatial control using electron-beam lithography (EBL). This allows carbon nanodots to be used to support location-dependent studies of both strong coupling and SERS.

4.2 Results

4.2.1 Design of IR Antennas

To fabricate plasmonic antennas capable of supporting both near- and mid-IR resonant modes, two designs were initially considered. The first design, hereby denoted as A1, consisted of a pair of mid-IR and a pair of near-IR antennas orientated perpendicular to each other as shown in Figure 4.3. The second design, hereby denoted as A2, consisted of a pair of near-IR antennas that were divided into two such that the larger segment could support resonances in the mid-IR region, while the smaller segment could support resonances in the near-IR region as shown in Figure 4.3.

FDTD simulations were performed to determine the dimensions required for Au nanoantennas fabricated on a bulk ITO substrate resonant in both the mid and near-IR region. A target resonance of 6.25 μm was selected for the mid-IR antenna as this matches

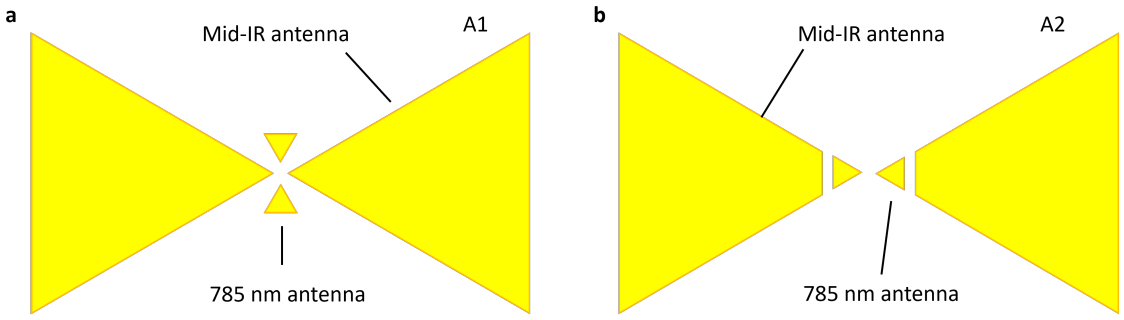

Figure 4.3: Schematic of geometry of antennas capable of supporting both mid- and near-IR resonances.

with the graphitic G band peak present in graphitic carbon nanodots fabricated using EBL. The target resonance for the near-IR antennas was 785 nm as this matches with the Raman laser that will be used to probe the system. Au was selected as the material for the nanoantennas as it is a good plasmonic material in both the near and mid-IR regions. Bowtie structures were selected for both near- and mid-IR antennas, as these types of structures possess broad resonances and should therefore be easier to couple with a vibrational mode or a Raman laser.[253] Furthermore, as the LSPR of bowtie antennas is dependent on the polarisation of the incident electromagnetic field, the bowtie structures will offer the possibility to probe polarisation-dependent coupling.

FDTD simulations predicted that a side length of 8 µm for the large antenna will yield a broad resonance around 6.25 µm. As can be seen from Figure 4.4(a) that this broad peak is present for light polarised parallel and perpendicular to the large bowtie antennas, indicating that further refinement of this design is required for polarisation dependent coupling to be investigated. A side length of 80 nm for the smaller bowties predicts a resonance around 785 nm to match with the laser used to probe the system. For the design A1, The gap size between the large bowtie was chosen as 100 nm. For design A2, the gap between the large and small antennas was 80 nm. For both antenna designs the gap between the small bowtie was 30 nm. While a smaller gap between antennas would yield a larger field enhancement, a larger gap was selected so that would be enough space to fabricate a carbon nanodot in the gap.

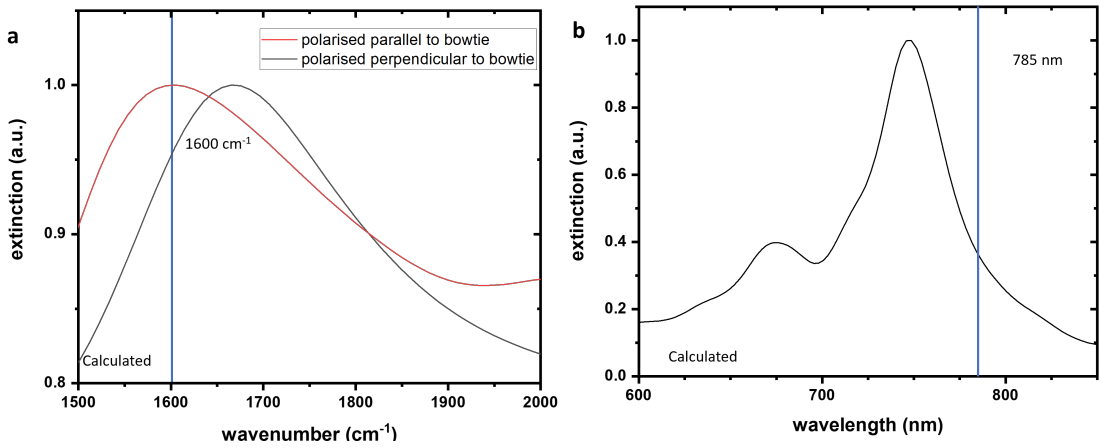

Figure 4.4: (a) Simulated extinction spectrum for mid-IR bowties with a side length of 8 µm and a gap size of 100 nm illuminated by and electric field polarised parallel (black) and perpendicular (red) to the large bowtie antenna. The blue line represents the target resonance of 1600 cm^{-1} (6250 nm) to match with the G band of a graphitic carbon nanodot. (b) Simulated extinction spectrum for NIR Au bowties with a side length of 80 nm and a gap of 30 nm. The blue line represents the target resonance of 785 nm to match with the laser that will be used to probe the antennas via Raman spectroscopy.

4.2.2 Fabrication of IR Antennas

IR antennas fabricated based on the simulations outlined in the previous section are shown in Figure 4.5. The side length of both the perpendicular and parallel large antennas were measured to be 8 µm. The gap between the large antennas in A1 was measured to be 90 nm. The side length of the small antennas in A1 was measured to be 76 nm, slightly smaller than the target length of 80 nm. This is likely due to the fact that the sharp tips of the target triangle shapes that were patterned are not thermodynamically stable, leading to a reduction of the size of the triangle side length. The gap between the large antennas and the smaller antennas in A2 was measured to be 31 nm, significantly smaller than the target gap size. The lower gap size is attributed to overexposure that occurred when patterning the vertical edge of the truncated large triangle. The side length of the small antennas in A2 was measured to be 82 nm, slightly larger than the target size of 80 nm. The increased size is attributed to over exposure due to proximity effects from the patterning of the truncated mid-IR bowtie.

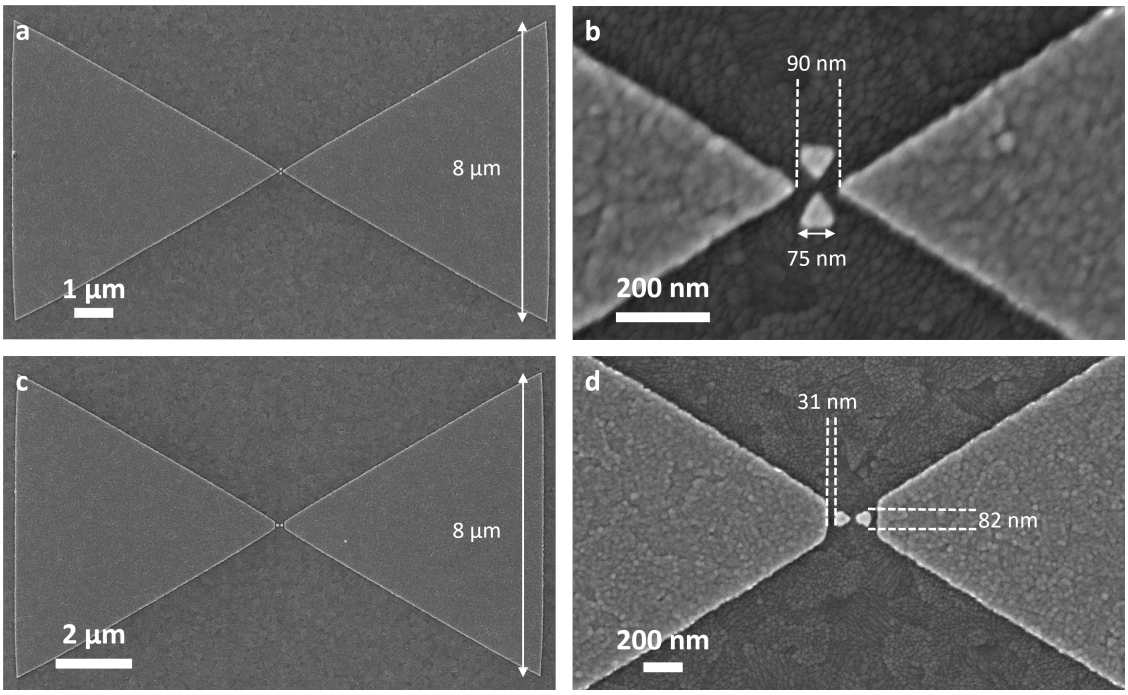

Figure 4.5: Antennas fabricated designed capable of supporting both mid- and NIR resonances. (a) and (b) show a design where the large, mid-IR antenna is perpendicular to the smaller NIR antenna. (c) and (d) show a second design where the tip of the large antenna is truncated and the mid- and NIR antennas are in parallel.

4.2.3 Fabrication of Carbon Nanodots

Carbon nanodots were fabricated in the gap between the nanoantennas by spin coating PMMA onto the fabricated antennas and exposing the resist by operating the beam in the 'spot' mode. The unexposed resist is removed via a typical lift-off process *i.e.,* immersion in n-methylpyrrolidone (NMP) at 60 °C for 45 min, to produce a carbon nanodot as shown in Figure 4.6. This method allows for great control over the placement of the nanodot. A Raman spectrum collected from an individual carbon nanodot located in the hot spot of an antenna designed to be resonant with the Raman laser is shown in Figure 4.7(b). The intense peak from a single nanodot observed in Figure 4.7(b) indicates that the near-IR bowtie antennas are capable of supporting SERS. We aim to couple the mid-IR antenna to the G band peak at 1600 cm^{-1} shown in Figure 4.7(b), which corresponds to a wavelength of 6250 nm. The large bowtie antenna shown in Figure 4.7(a) was not designed for VSC with the carbon nanodot, hence no evidence of coupling is observed in the Raman spectrum.

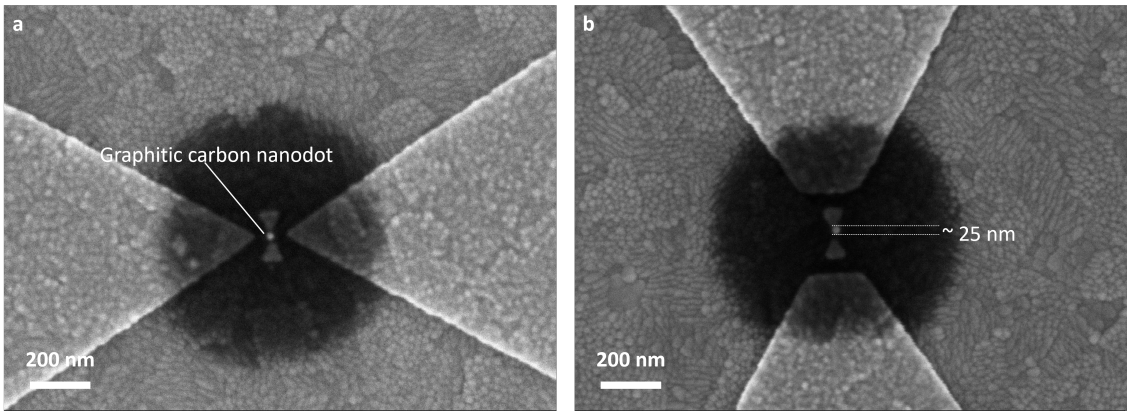

Figure 4.6: Carbon nanodots fabricated in the centre of plasmonic nanoantennas using EBL.

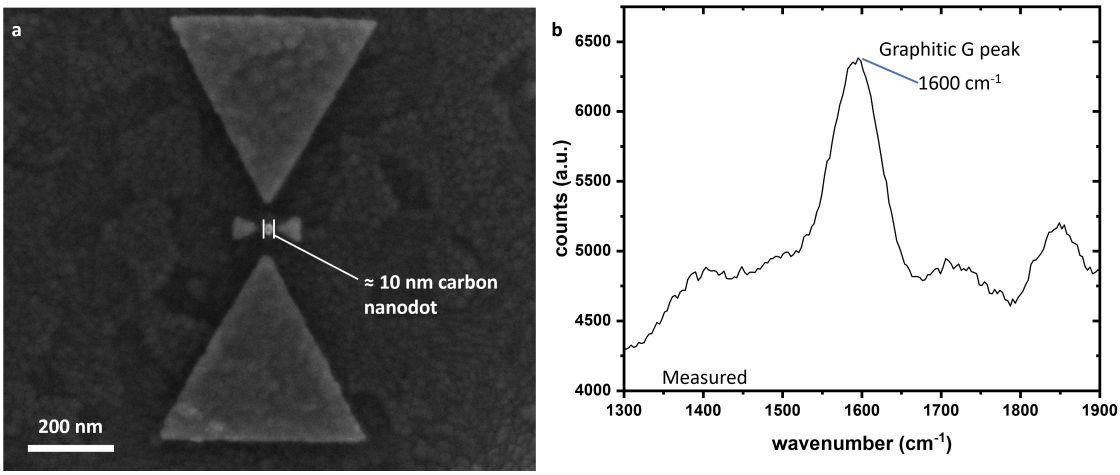

Figure 4.7: (a) Carbon nanodot fabricated in the centre of a plasmonic nanoantenna. The larger bowties shown here were not designed for VSC with the carbon nanodot. (b) Raman spectrum collected from a carbon nanodot in the centre of a plasmonic bowtie shown in (a). The Raman signal was collected using a 785 nm laser polarised in parallel to the small bowtie antenna. The blue line in the Raman spectrum represents the target LSPR wavelength of the mid-IR antennas at 1600 cm^{-1} (6250 nm).

4.2.4 Segmented Antenna Design

As each double-antenna design features only a single near-IR antenna, the resonance wavelength of this antenna could not be confirmed as the extinction spectrum of a single nanoantenna is beyond the sensitivity of our spectroscopy setup. Furthermore, the difficulty in aligning the Raman laser to a single nanodot located within a single nanoantenna led to the development of a new design that would alleviate some of these difficulties. Plasmonic antennas with fractal geometries have been shown to be capable of supporting multiple plasmonic modes.[254] Macroscopic fractal antennas have been used for applications in the GHz range of the spectrum.[255] Modern fabrication techniques such as EBL have made it possible to fabricate complex geometries on a nanometre scale. To date, plasmonic antennas based on multiple different fractal geometries have been demonstrated to support multiple resonances across the IR region of the spectrum.[254,256–258]

Here, we propose a design consisting of Au nanodiamonds arranged in the shape of a large bowtie antenna, hereby denoted as A3. The aim is for the nanoantennas to support LSPRs in the near-IR range, while the collective oscillation over the entire bowtie array would be resonant in the mid-IR. Design A3 would allow for the fabrication of carbon nanodots in the gaps between multiple individual nanodiamonds, thereby increasing the likelihood of the Raman laser overlapping with the plasmonic hotspot. A schematic for this design alongside its simulated extinction spectra in the mid and near IR are shown in Figure 4.8.

4.2.5 Fabrication of Segmented Antenna

Initial fabrication of A3 was performed on bulk ITO substrates. The high density of the nanodiamonds presented a challenge in fabrication owing to large proximity effects. When using EBL to pattern a resist there will be some energy deposited into the resist that remains below the energy threshold for the resist to be exposed. When structures are patterned in close proximity to each other, these regions of excess dose can overlap with each other, summing together to provide enough dose to cause unwanted exposure of the resist in the region between each structure. This unwanted exposure is known

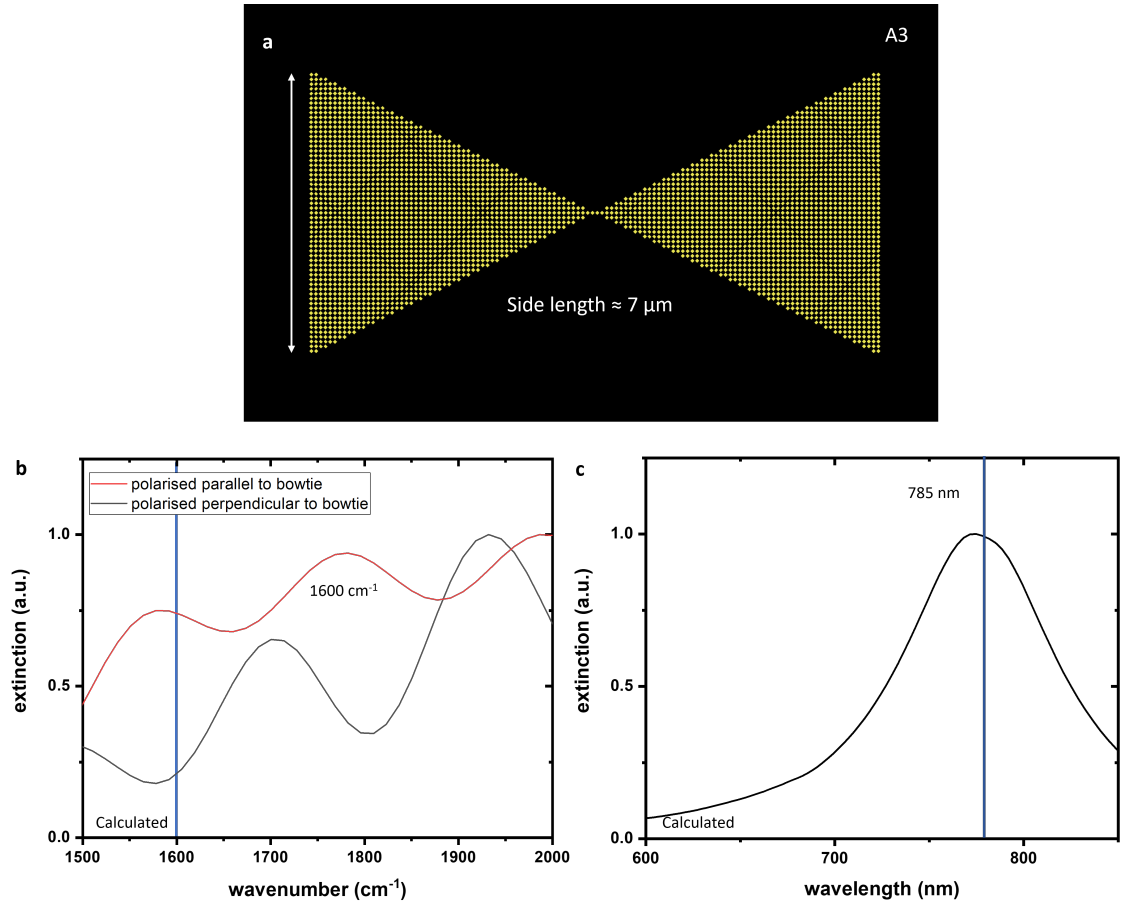

Figure 4.8: (a) Schematic of a new design for plasmonic antennas that support both mid- and near-IR resonances. The large bowtie antenna is designed to be resonant around 1600 cm^{-1}. The large bowtie is made up of nanodiamonds with a separation of 15 nm in both the x and y-directions. Each nanodiamond is designed to be resonant at 785 nm. (b) Simulated mid-IR extinction spectrum in wavenumbers for the segmented antenna. The blue line represents the target resonance to match with the G peak of the graphitic carbon nanodot at 1600 cm^{-1} (6250 nm). (c) Simulated optical spectrum for a pair of nanodiamonds. The blue line represents the target resonance at 785 nm to match with the laser used to probe the antenna with Raman spectroscopy.

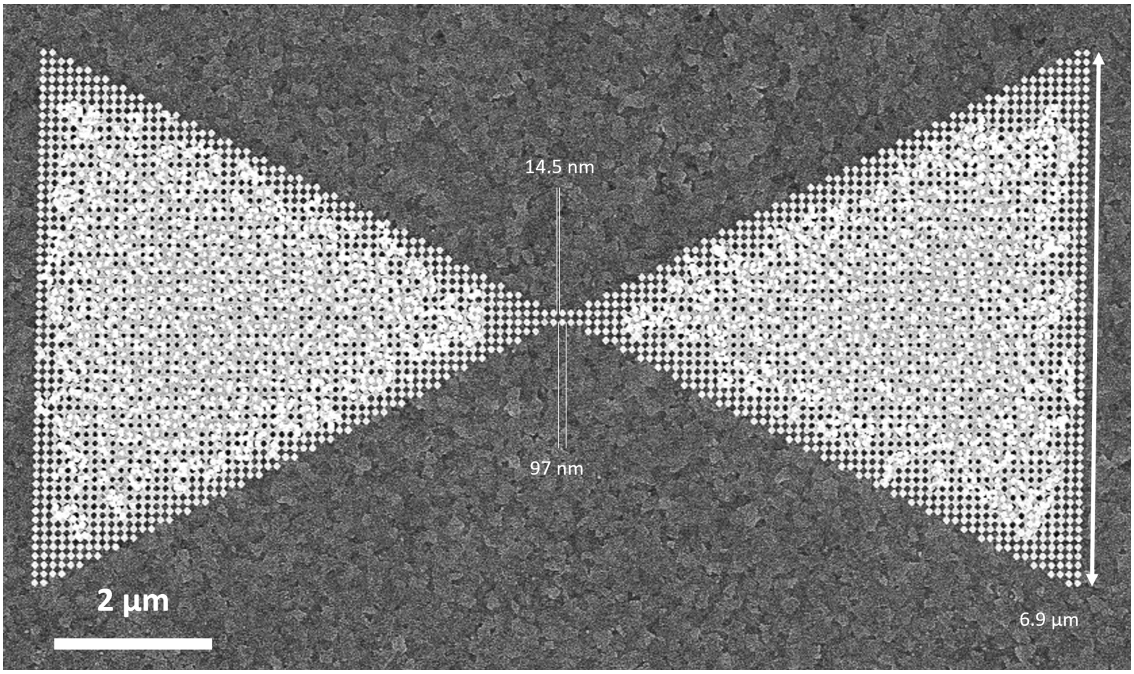

Figure 4.9: SEM micrograph of partially fabricated segmented nanoantenna.

as the proximity effect. To account for proximity effect nanodiamonds in the centre of the bowtie array were given a dose one quarter the amount of the nanodiamonds at the edges. A fabricated segmented antenna is shown in Figure 4.9. The diagonal length of the nanodiamonds was measured to be 97 $\pm$ 4 nm, within error of the target length of 100 nm. The gap size was measured to be 15 $\pm$ 3 nm, within error of the target size of 15 nm. The side length of the large bowtie was measured to be 6.9 $\pm$ 0.02 µm.

It can be seen from Figure 4.9 that proximity effects during the EBL process led to an incomplete lift-off of the Au metal in the centre of A3. However, as a significant number of nanodiamond antennas were fabricated successfully optical and Raman spectra could be recorded from the segmented antenna. From the extinction spectrum in Figure 4.10(a) it can be seen that there is a strong peak near the 785 nm laser line. As the ITO-on-glass substrate is not transparent to IR radiation, Raman spectroscopy was used to probe the mid-IR resonance of the segmented antenna. From Figure 4.10(b) it can be seen that there is a peak at the desired 1600 cm^{-1} wavenumber, however it is uncertain whether this peak is due to a plasmonic resonance or due to graphitic carbon residues from the resist or solvents used to remove the resist.

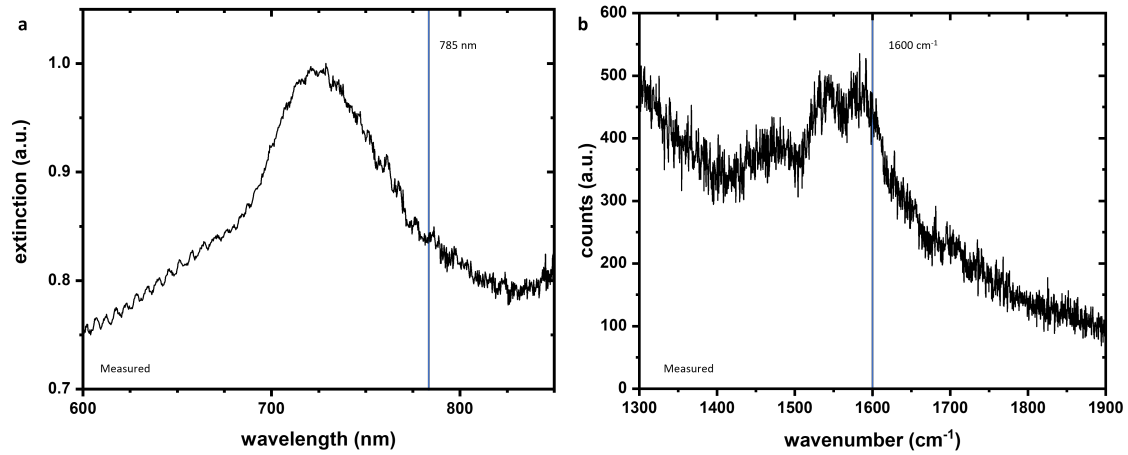

Figure 4.10: (a) Measured optical extinction spectrum of the structure shown in Figure 4.9. The blue line represents the 785 nm laser line. (b) Measured Raman spectrum of the structure based on design A3 shown in Figure 4.9. The Raman spectrum was collected with a 785 nm laser with polarised parallel to the large antenna. The blue line indicates the target resonant wavelength of the large bowtie at 1600 cm^{-1} (6250 nm).

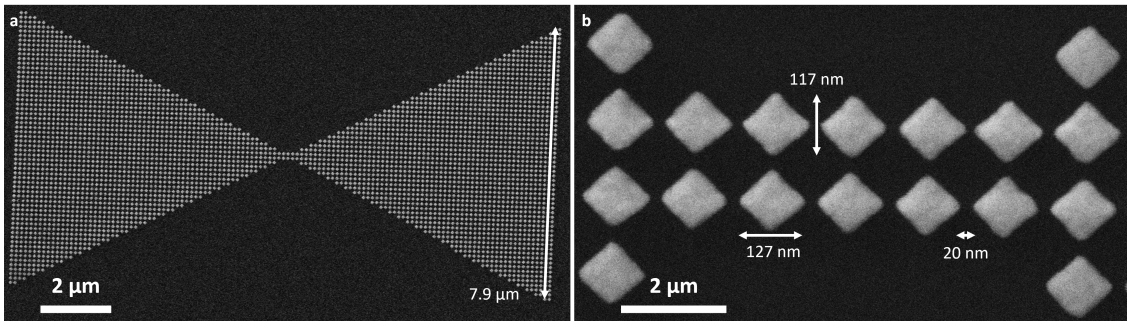

Figure 4.11: Complete segmented nanoantennas fabricated on a 50-nm-thick SiN membrane.

4.2.6 Fabrication of Segmented Antennas on SiN_x X-ray Windows

To confirm the mid-IR resonance, the segmented antennas were fabricated on SiN_x x-ray windows designed to be transparent to IR radiation. This would allow the mid-IR extinction spectrum of the antennas to be measured. As the SiN_x substrates are 50-nm-thick, scattering effects from the substrate will be reduced compared to the bulk substrates. Consequently, proximity effects will be reduced and the fabrication of the complete structure will be easier. Figure 4.12(a) show the results of optical simulations on a SiN_x substrate. It was found that a diagonal length of 115 nm is required for resonance at 785 nm, compared to the length of 100 nm used for nanodiamonds fabricated on ITO.

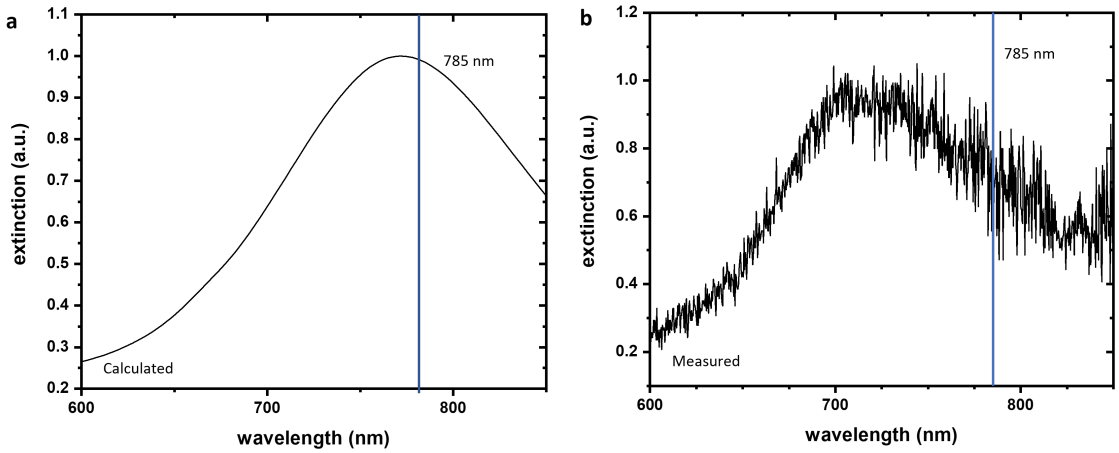

Figure 4.12: Calculated (a) and measured (b) optical extinction spectrum of the segmented antenna on a SiN_x substrate shown in Figure 4.11. The blue lines represent the target resonance of 785 nm to match with the laser used to probe the antenna via Raman spectroscopy.

Figure 4.11(a) shows the complete fabricated structure on the SiN_x membrane. The diagonal length of the nanodiamonds in the *x*-direction was measured to be 127 $\pm$ 3 nm which is larger than the target diagonal length of 115 nm. In the *y*-direction, the diagonal length was measured to be 117 $\pm$ 2 nm, much closer to the target length of 115 nm. The gap size between the nanodiamonds in both directions was measured to be 20 $\pm$ 2 nm, slightly larger than the target size of 15 nm. The diagonal length in the *x*-direction and gap size were measured to be slightly larger than their target lengths which may indicate a slight placement error during the electron beam lithography process. The larger gap size will yield a reduced field enhancement in the plasmonic hot spot and the increased size of the structures will lead to a slight redshift of the LSPR wavelength. However, as the simulated spectrum indicates that the LSPR peak wavelength is slightly lower than the target of 785 nm, this redshift may increase the overlap between the nanodiamond resonance and the laser. The side length of the large bowtie was measured as 7.9 $\pm$ 0.03 µm. The measured extinction spectrum in Figure 4.12(b) shows a broad peak around 785 nm, indicating that there should be good overlap between the Raman laser and the fabricated structures.

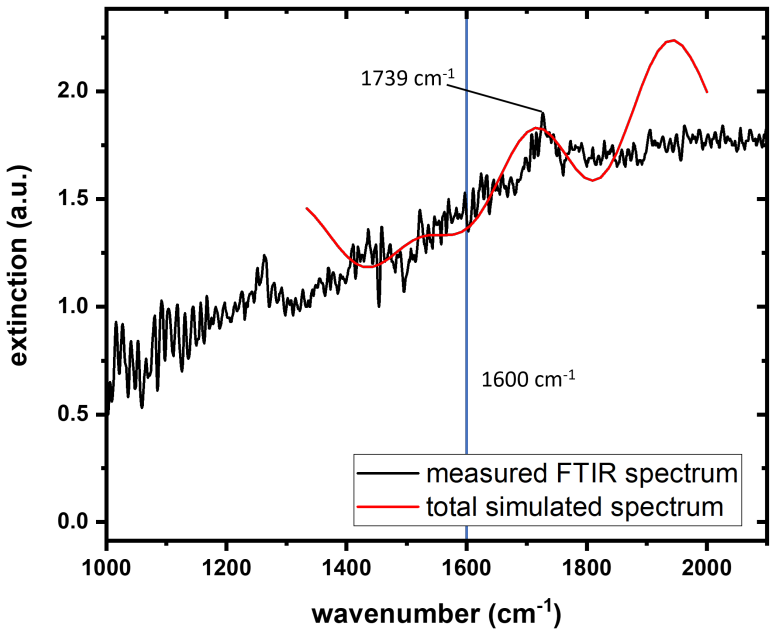

Figure 4.13: Measured (black) and simulated (red) IR spectra of a single segmented antenna. The blue line represents the target resonance for the plasmonic IR mode at 1600 cm^{-1}. The simulated spectrum consists of the sum of simulated spectra calculated using light parallel to the long axis of the bowtie, and orthogonally polarised light.

4.2.7 FTIR Spectroscopy of Segmented Antenna

FTIR spectroscopy was employed to determine the presence of a plasmonic mode near the target wavenumber of 1600 cm^{-1}. The measured IR spectrum recorded from a single A3 bowtie is shown in Figure 4.13. The simulated extinction spectrum for this design is superimposed onto the measured spectrum. As the light source in the FTIR microscope used to record the spectrum is non-polarised, the simulated spectrum shown in Figure 4.13 is the sum of the simulated spectrum parallel to the bowtie and the corresponding spectrum calculated using an orthogonally polarised light source shown in Figure 4.8(a). The first clear observation is that by summing the two simulated spectra, the peak around 1600 cm^{-1} is diminished as the orthogonally polarised spectrum yields more intense peaks that are not designed to be resonant at this frequency. The simulated spectrum agrees with the observed spectrum in the region from 1500-1850 cm^{-1}, but deviates from the measurement outside of this range. In the measured IR spectrum, a peak can be seen at around 1739 cm^{-1}. It can be seen from the spectrum that this matches quite well with one of the peaks in the simulated spectrum, indicating that it may correspond

to a plasmon mode of the orthogonally aligned bowtie. It should be noted however that the PMMA carbonyl stretching mode has been reported to occur around 1730 cm^{-1},[259] so it is possible that this peak is due to some residue after the lithography process. Furthermore, there is no evidence in the measured spectrum of the peak present at around 1900 cm^{-1} in the simulated spectrum so it cannot be said for certain that the peak at 1739 cm^{-1} corresponds to a plasmonic mode. The desired 1600 cm^{-1} could potentially be more readily detected by redesigning the antenna to reduce the intensity of the orthogonal plasmonic modes, or by using a polarised light source to probe only the desired polarisation.

4.2.8 Estimation of Coupling Between Carbon Nanodot and Segmented Antennas

To estimate the strength of the coupling between the plasmonic cavity of the segmented antenna and the carbon nanodot we use a coupled oscillator model used by Pelton *et al.* to calculate the extinction spectrum of the coupled system.[260] The simulated extinction cross section for the coupled system is given by

$$C_{ext}(\omega) = \omega Im\left(\frac{(\omega_{mol}^2 - \omega^2 - i\gamma_{mol}\omega)}{(\omega^2 - \omega_{LSPR}^2 + i\gamma_{LSPR}\omega)(\omega^2 - \omega_{mol}^2 + i\gamma_{mol}\omega) - \omega^2 g^2}\right), \quad (4.2)$$

where ω_{mol} and ωSP are the resonant frequencies of the molecular vibration and LSPR respectively. In our case these values are equal at 1600 cm^{-1} (198 meV). The values γ_{mol} and γ_{LSPR} represent the linewidth of the molecular vibration and the LSPR respectively. The value for γ_{mol} is taken from the full-width at half maximum (FWHM) of the recorded Raman spectrum from a carbon nanodot shown in Figure 4.7(b), which was found to be 67 cm^{-1} (8.3 meV). The value for γ_{LSPR} was taken from the FWHM of the simulated mid-IR spectrum of the segmented antenna in Figure 4.8(a), which was found to be 106 cm^{-1} (13.1 meV). The value g represents the coupling strength between the vibrational mode and the LSPR mode of the segmented antenna.

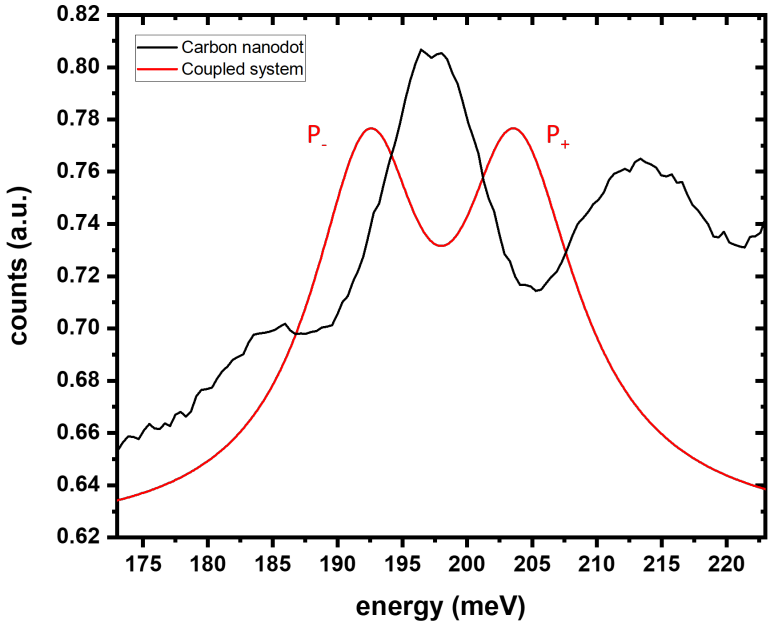

Figure 4.14: Predicted extinction spectrum of the strongly-coupled carbon nanodot-segmented antenna system (red) superimposed over the measured Raman spectrum collected from a carbon nanodot.

In order to estimate the value of g we first consider the case for resonance between the molecular vibration and the LSPR *i.e.*, $\omega_{mol} = \omega_{LSPR} = \omega_0$. When $\omega - \omega_0 << \omega_0$ Equation 4.2 can be simplified to

$$C_{ext} \approx \omega Im \left(\frac{\omega_0 - \omega - \dfrac{i\gamma_{mol}\omega}{2}}{2\omega_0 \sqrt{g^2 - \dfrac{(\gamma_{LSPR} - \gamma_{mol})^2}{4}}} \left(\frac{1}{\omega - \Omega_+} - \frac{1}{\omega - \Omega_-} \right) \right), \tag{4.3}$$

where $\Omega_\pm = \omega_0 + i(\gamma_{LSPR} + \gamma_{mol})/4 \pm \sqrt{g^2/4 - (\gamma_{LSPR} - \gamma_{mol})^2/16}$. The system enters the strong-coupling regime when $g >> (\gamma_{LSPR} - \gamma_{mol})/2$. Consequently for our carbon nanodot-segmented antenna system $g >> 2.4$ meV. Here, we use $g = 10.7$ meV as this is equivalent to $\gamma_{LSPR}/2 + \gamma_{mol}/2$ and satisfies the above condition.

The calculated extinction spectrum of the strongly-coupled carbon nanodot-segmented antenna system is shown in Figure 4.14. The Rabi splitting energy between the upper and lower polariton peaks, $\hbar\Omega_R$ is given by $2g$ and is 21.4 meV. This value is larger than the value for Rabi splitting energy of 8.7 meV reported by Thomas *et al.* for the strong coupling of a Fabry-Pérot cavity to a Si-C stretching mode,[245] and the energy of 9.4 meV

reported by Verdelli *et al.* for the VSC between a surface lattice resonance of an array of Au nanoparticles and the C=O stretch of a PMMA film.[250] However, Rabi splitting energies from 135-200 meV have been reported for the strong coupling of plasmonic Au nanoparticles to J-aggregate dye molecules, owing to the small mode volume of the plasmonic nanoparticles.[261] Therefore, we believe that the value for $\hbar\Omega_R$ found here will be achievable for a carbon nanodot strongly coupled to our segmented plasmonic nanoantenna.

4.3 Conclusions and Outlook

Here we have proposed and fabricated using EBL a design for segmented plasmonic antennas capable of supporting resonances in the near-IR and mid-IR regions of the spectrum. The mid-IR antenna is designed to be resonant at the same frequency as a G band vibration of a graphitic carbon nanodot, with the aim of achieving strong coupling between the antenna and the nanodot. The near-IR antenna is designed to be resonant at the same frequency as a laser used to probe the system with Raman, thereby allowing the antenna to support SERS. We have shown that using EBL a sub-30-nm diameter carbon nanodot can be fabricated in the plasmonic hot spot of a nanoscale plasmonic antenna. The G band peak of an individual nanodot could be detected in the Raman spectrum of one of these antennas indicating that the near-IR bowties can support SERS. Segmented antennas were fabricated on an ITO substrate and the Raman spectrum collected from these antennas indicated the presence of a peak present around the target wavenumber for VSC at 1600 cm^{-1}. As ITO is not transparent to mid-IR radiation, segmented antennas were fabricated on SiN_x substrates. Optical extinction spectra from these segmented antennas indicated a broad resonance around the target wavelength of 785 nm to match with the laser in the Raman system.

To date, the presence of a resonance around the desired wavelength of the mid-IR region has not been confirmed, work on this remains ongoing. IR spectra recorded from a segmented antenna revealed a peak around 1739 cm^{-1}, however it has not been confirmed whether this peak is due to a plasmonic mode or a carbonyl stretching mode present

in PMMA residue on the sample. One of the challenges in collecting IR spectra from these segmented antennas is the high signal-to-noise ratio due to the low intensity of scattering and absorption of the antennas. The signal-to-noise ratio could be improved by fabricating denser arrays of segmented antennas so that there is more signal from the antennas collected by the slit in the FTIR microscope. Furthermore, IR microscopes utilising quantum cascade lasers (QCLs) have recently been developed.[262] The spectral power of these QCLs is much higher than that found in a typical FTIR spectrometer, and therefore the IR signal recorded is much stronger. Using one of these QCL systems would increase the signal-to-noise ratio of the IR spectra collected from the segmented nanoantennas. In addition to the poor signal-to-noise ratio, the light source used to collect the IR spectrum is non-polarised and therefore the signal consists of the sum of plasmonic modes parallel and orthogonal to the long axis of the segmented bowtie. IR simulations revealed that the orthogonal modes have a significant intensity and could obscure the mode around 1600 cm^{-1}. Recording IR spectra with a polarised light source would eliminate these orthogonal modes and help to isolate the modes parallel to the long axis of the antenna.

The extinction spectrum of the coupled system using the coupled harmonic oscillator model used by Pelton *et al.*[260] Using the values for the FWHM of the measured Raman peak of a graphitic carbon nanodot and the simulated mid-IR LSPR peak of the segmented antenna a Rabi splitting energy of 21.4 meV was predicted for the strongly coupled nanodot-antenna system. This Rabi energy is larger than the Rabi splitting observed for VSC with both a Fabry-Pérot cavity and a surface lattice resonance indicating that these segmented antennas could achieve stronger VSC than has been reported to date.[245,250]

Chapter 5

Localised Growth of Semiconductor Materials Driven by Localised Surface Plasmon Resonances

5.1 Semiconductor Nanomaterials

Semiconductor nanomaterials play a key role in the advancement of technology in today's society. The ability to tune the charge transport properties of semiconducting materials has led to a plethora of applications in fields such as logic devices for integrated circuits, light emitting devices, optoelectronics, sensing, thermo-electrics, biomedical applications and catalysis.[263–275] In order for the advancement of semiconductor technologies to continue, alternative materials must be investigated. Furthermore, novel methods of fabricating semiconductor materials on a nanometre scale are required to satisfy the ever-increasing demand for smaller devices.

Ge is an important semiconductor with a direct bandgap at 0.8 eV (1550 nm) and an indirect bandgap at 0.66 eV (1880 nm). Historically, Si has been preferred as a choice of semiconductor over Ge due to the superior stability of the native SiO_2 oxide layer compared to the native GeO_2 oxide layer. However with the advent of new, high-k materials that can be deposited directly onto the semiconductor, interest in Ge has increased

in recent years as materials other than Si are considered for improved transistors for logic gates and other functions.[276–278] Compared to bulk Si, bulk Ge possesses higher intrinsic carrier mobilities (electron mobility, μ_n, $= 3900$ cm^{2}V^{-1}s^{-1} and hole mobility, μ_p, $= 1900$ cm^{2}V$^{-1}s^{-1}$ for Ge, versus $\mu_n = 1450$ cm^{2}V^{-1}s^{-1} and $\mu_p = 500$ cm^{2}V^{-1}s^{-1} for Si at 300 K).[279] Higher charge mobilities yield higher transistor drive currents, which leads to improved performance and lower power consumption. The high mobility of charge carriers in Ge make it an attractive alternative to Si in future low-power logic devices.[263] The intrinsic charge carrier concentration for a semiconductor, n_i, is given by

$$n_i = 2\left(\frac{k_B T}{2\pi\hbar^2}\right)^{3/2} (m_e m_h)^{3/4} \exp(-E_g/2k_B T), \tag{5.1}$$

where k_B is the Boltzmann constant, m_e and m_h are the effective electron and hole masses respectively, and E_g is the band gap of the semiconductor. Compared to Si, Ge possesses a lower band gap (0.66 eV for Ge vs 1.17 eV for Si at 300K) as well as a higher intrinsic charge carrier concentration (2.4×10^{13} cm^{-3} for Ge vs 1.45×10^{10} cm^{-3} for Si). Ge also has a larger bulk excitonic Bohr radius than Si (24.3 nm for Ge versus 4.7 nm for Si) due to its lower effective mass. This larger excitonic Bohr radius yields more prominent quantum-confinement effects.[277]

In a bulk semiconductor the large number of atoms present result in the formation of continuous valence and conduction bands. However, as the dimensions of the semiconductor are reduced, the total number of atoms present is lowered resulting in the emergence of discrete energy levels and an increase in the bandgap of the semiconductor. This is known as the '*quantum-confinement effect*' and typically occurs when the dimensions of the semiconductor are near its excitonic Bohr radius. The quantum-confined Stark effect is the shift of the energy levels of a quantum well due to the application of an electric field. The resulting redshift of the band edge and the exciton energies can be exploited to make optical modulators.[280] The quantum-confinement of electrons and holes also results in an increase in the emission energy of the semiconductor when compared to the bulk. The redshift of the band edge due to the quantum-confined Stark effect can also increase the overlap in the wavefunctions of electrons and holes thereby shortening the radiative lifetime, and increasing the efficiency of radiative decay. Consequently quantum wells

make bright light-emitting devices whose emission properties can be tuned by the choice of quantum-well parameters.[281]

ZnO is a semiconductor with a large band gap of 3.37 eV at room temperature, making it suitable for applications in the blue and UV region of the spectrum.[282,283] The high exciton binding energy of ZnO of 60 meV can allow for significant excitonic emission at room temperature, and subsequently, room temperature UV emission from ZnO nanoparticles and thin films has been reported.[282] To date, ZnO has been used in applications in catalysis, solar cells, sensing, and mechanical actuators.[284–287] In this chapter, we propose a method for the fabrication of crystalline Ge and ZnO with dimensions approaching the threshold required for quantum confinement effects to be realised, and with control over the on-chip location of the semiconductor nanomaterial.

5.2 Fabrication of Nanocrystalline Germanium

Ge nanocrystals (NCs) can be synthesised via either physical or chemical approaches. Physical methods for the fabrication of Ge NCs include chemical vapour deposition (CVD), etching, laser ablation, sputtering, gas-phase pyrolysis, plasma techniques, and ion implantation followed by high-temperature annealing.[288,289] These techniques use extreme temperatures and pressures and thus are expensive and difficult to scale. Furthermore, most of these methods produce crystals with broad distributions of sizes, as well as broad optical absorption and photoluminescence features that make it difficult to relate the effects of quantum confinement and other mechanisms to these spectra.[288]

Approaches based on bottom-up chemical synthesis of semiconductor NCs are attractive as they can be scaled up for commercial production, however there a several challenges facing the synthesis of Ge NCs.[290] Ge is strongly covalent, and therefore has a high crystallization temperature, potentially above 400 ºC. Many organic solvents are unstable at these temperatures which can result in the presence of impurities that are challenging to remove.[288,291] Furthermore, many common Ge salts require harsh reaction conditions and chemicals to convert them to elemental Ge.[290]

5.2.1 Vapour-Liquid-Solid Growth of Semiconductor Nanowires

The vapour-liquid-solid (VLS) growth mechanism has been commonly used in the growth of semiconductor nanowires since it was first reported by Wagner *et al.,*[292] in 1964. In this method, a metallic nanoparticle is chosen as a seed for growth. A vapour phase containing a semiconductor precursor molecule is then flowed over the seed particle, and the system is heated to drive decomposition of the precursor molecule and formation of a liquid alloy of the metallic seed and the semiconductor. As the concentration of the semiconductor increases, it begins to precipitate out of the liquid alloy as a solid 'whisker' or nanowire. As the nanowire grows it pushes the seed particle away from the substrate such that the seed 'rides' atop the whisker as shown in Figure 5.1. The growth continues until the seed particle is fully consumed or the growth conditions are changed *i.e.,* the heating of the system is terminated, the flow of the precursor molecule is stopped *etc.*[292] The diameter of the nanowire grown is typically dependent on the radius of the seed particle, and as such can be controlled by careful design of the seed particle.

In recent years, solution-based approaches such as solution-liquid-solid (SLS) and supercritical fluid-liquid-solid (SFLS) growth have been used to produce large amounts of crystalline Ge nanowires with good control of the wire diameter.[293,294] Similar to VLS, SLS and SFLS promote nanowire growth via the formation of a eutectic between a metallic seed particle and the semiconductor. SFLS involves the heating and pressurisation of solvents above their critical point, enabling temperatures in the range of 400-650 ºC.[295,296] SFLS uses temperatures above the eutectic points of many metal/semiconductor alloys, enabling a variety of metal seeds and reactants to be used for the growth of both Ge and Si nanowires, however the high pressures limit the scalability of these processes.[294] SLS uses ambient conditions and is therefore limited by the boiling point of the solvent used. The bulk Au:Ge eutectic occurs at $\sim$ 360 ºC, and thus high-boiling point solvents such as squalane are typically used for SLS growth.[294] A numerical study by Lu *et al.* found that the Au:Ge eutectic occurs at lower temperatures as the dimensions of the seed particle and nanowire decrease.[297] For Au seed nanoparticles and Ge nanowires with a diameter of 10 nm the eutectic was found to occur at a temperature 47 K below the bulk. Furthermore, the melting points for 10 nm Au and Ge nanoparticles were found to

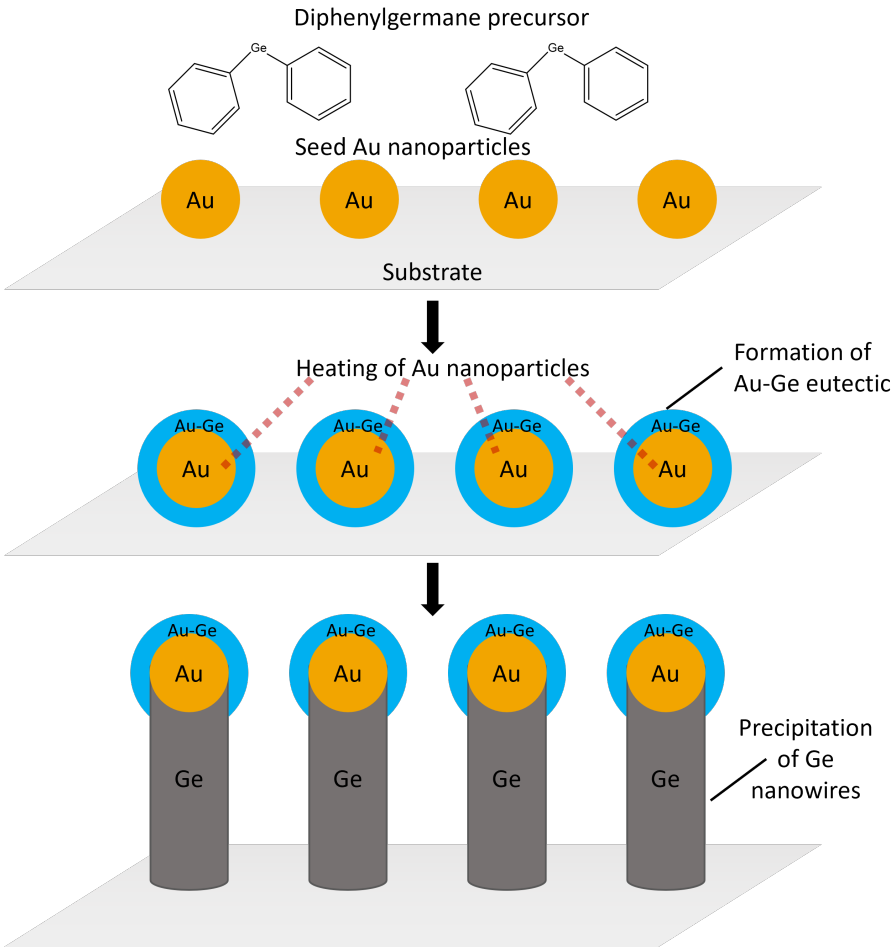

Figure 5.1: The solution-liquid-solid growth of Ge NWs. Au seed nanoparticles are dispersed on a substrate and immersed in diphenylgermane. The heating of the seed particles results in the formation of the Au-Ge eutectic. When the eutectic alloy is saturated, elemental Ge precipitates out in the form of crystalline NWs.

be 105 K and 83 K lower than their bulk meting temperatures respectively. These results indicate that the VLS growth process could be initiated at lower temperatures as the size of the seed nanoparticles is decreased.

5.2.2 Laser Induced Growth of Semiconductor Nanowires

The high temperatures required by SLS growth are typically achieved by global heating of the reaction system. This limits the versatility of this process when aiming to grow semiconductor materials on top of existing devices, or on soft materials as they can be damaged during the growth process. Consequently, there has been a push to-

wards low temperature growth methods, or methods involving localised heating of the reactants.[298] One such method for localised heating is the use of laser irradiation of the seed particles.[299] The excitation of LSPRs of metallic nanoparticles can result in further confinement of incident laser irradiation around the nanoparticle,[300] as well as plasmonic heating of the metal surface.[9] Using this localised heating would allow for greater control of the nanowire growth process, while also reducing the energy required when compared to heating the entire system.[69] Furthermore, using a laser for localised heating could allow for faster switching of the heating of the metal nanoparticles. If the entire system is heated, it will remain at elevated temperatures for some time after the heating is switched off, potentially allowing the reaction to continue for some time after the heating has been switched off. Using a laser to selectively heat seed particles offers almost instantaneous control of the heating and in principle growth can be stopped and started with submonolayer precision.[69] In addition, it has been shown that plasmonic nanoparticles can act as heat sources to heat water beyond 100 °C. Baffou *et al.,* observed supercritical water with temperatures up to 220 °C before bubble formation occurred upon illumination of Au nanoparticles with a laser matched to their LSPR frequency.[66] The superheating is possible due to high internal pressures of micro-bubbles. The internal pressure of a micro-bubble is given by:[301]

$$P_{MB} = P_{\infty} + \frac{2\gamma}{a}, \tag{5.2}$$

where P_{∞} is the ambient pressure, γ is the surface tension of the liquid and a is the radius of the micro-bubble. Bubbles with radii on the order of microns have internal pressures much higher than atmospheric pressure, and therefore allow for the heating of the solvent beyond its typical boiling point. As a result of the elevated temperatures possible via plasmonic heating, plasmon-induced SLS growth could be an alternative method of producing semiconductor NCs.

To date, literature reports have shown that Ge and ZnO have been successfully grown by irradiating plasmonic Au nanoparticles with laser light matched to the appropriate LSPR frequency.[298,302] In the case of Ge, a gaseous precursor was passed over chemically grown Au nanoparticles, randomly dispersed on a SiN_x membrane.[298] For the growth of nanocrystalline ZnO nanostructures, Au nanostructures were first fabricated on a glass

substrate using electron-beam lithography (EBL) and were then immersed in a liquid-phase- precursor solution.[302] In both cases, nanowire growth was observed upon illumination of the metal nanoparticles with a laser that matched with the LSPR frequency of the nanoparticles. Colloidal Bi and In nanoparticles have also been shown to seed the growth of CdSe and Ge nanowires under laser illumination.[303] However, in this experiment a high-power (2-15 W) laser was used to irradiate the samples. Furthermore, the laser wavelength was not matched to the LSPR of the nanoparticles.

EBL is a top-down fabrication technique that allows for the precise control of feature geometries and positions on a sub-10-nm scale.[136] This makes it an ideal technique for fabrication of plasmonic structures as the LSPR resonance can be tuned by varying the geometry of the structure.[77,304] Furthermore, if these plasmonic structures are being used as seeds for the growth of semiconductor materials, fabrication with EBL allows for precise control of the location where growth is initiated. Plasmonic nanoparticles can transfer energy directly into semiconductor nanomaterials if they are in close enough proximity to each other.[31] Fabricating semiconductors directly on the surface of these plasmonic nanoparticles can result in the formation of strongly coupled systems which can open new pathways for catalysis and modification of the light emission properties of the isolated semiconductors.[38,274,305] Controlling the growth of the crystalline material such that it remains located near the surface of the metal catalyst could allow for the fabrication of devices based on these strongly coupled systems. Here we use EBL to fabricate Au nanoantennas resonant at a wavelength of 785 nm to catalyse the growth of Ge nanowires when illuminated by a 785 nm laser. We use Au as it is a well-known catalyst for the growth of GeNWs, as well as being a good plasmonic material in the NIR region.[13] The benefit of this approach is that the use of EBL allows for control of the on-chip placement of the seed particles and thus the placement of the semiconductor material. Furthermore this approach can be adapted to use other plasmonic metals such as Ag or Al as seed nanoparticles for the growth of other semiconductor materials.

5.3 Results and Discussion

5.3.1 Optical Properties of Au Nanoantennas

FDTD simulations were used to design Au nanoantennas with two distinct geometries having their LSPR modes close to the laser wavelength of 785 nm. Bowtie nanoantennas consisting of pairs of equilateral triangles with a side length of 85 nm and a gap of 15 nm between them were chosen as the first geometry. The bowtie nanoantenna design is an attractive structure as the sharp tips at the apex of the triangles allow for '*lightning-rod*' effects as well as the field enhancement from LSPR. Furthermore, by placing two triangles with their tips facing each other, large field enhancements can be achieved in the gap between the antennas. This bowtie geometry also supports a broader LSPR than when compared to a nanorod dimer geometry due to the fact that the triangular geometry of the bowtie can support multiple resonances.[253] We also design Au nanodiamond structures consisting of squares with a side length of 71 nm, rotated at a 45 degree angle. This corresponds to a length of 100 nm for the bisector along the long axis. There is a gap of 15 nm between each nanodiamond. These structures aim to maximise the total field enhancement over a given area by exploiting the symmetry of the design and by increasing the total number of plasmonic hot spots per area, while also supporting lightning-rod effects.

Simulated extinction spectra as well as electric field enhancement for both bowtie and nanodiamond structures on an ITO substrate are shown in Figure 5.2. Light polarised along the x-axis was used in each simulation. Periodic boundary conditions were used to allow for an array of nanostructures to be simulated. This allows for any effects of surface lattice resonances present in the array to be included. For bowties, a period of 400 nm in both x and y directions were used to isolate each bowtie and reduce the effects of interference between the LSPR of adjacent bowties. For nanodiamonds, a period of 115 nm in the x direction was used so that there was a continuous series of nanodiamonds with a gap of 15 nm between each. A period of 400 nm was used in the y direction. As expected, the field enhancement is strongest in the gap between two structures, with the maximum enhancement nearest the sharp tips of the structures. The maximum field inten-

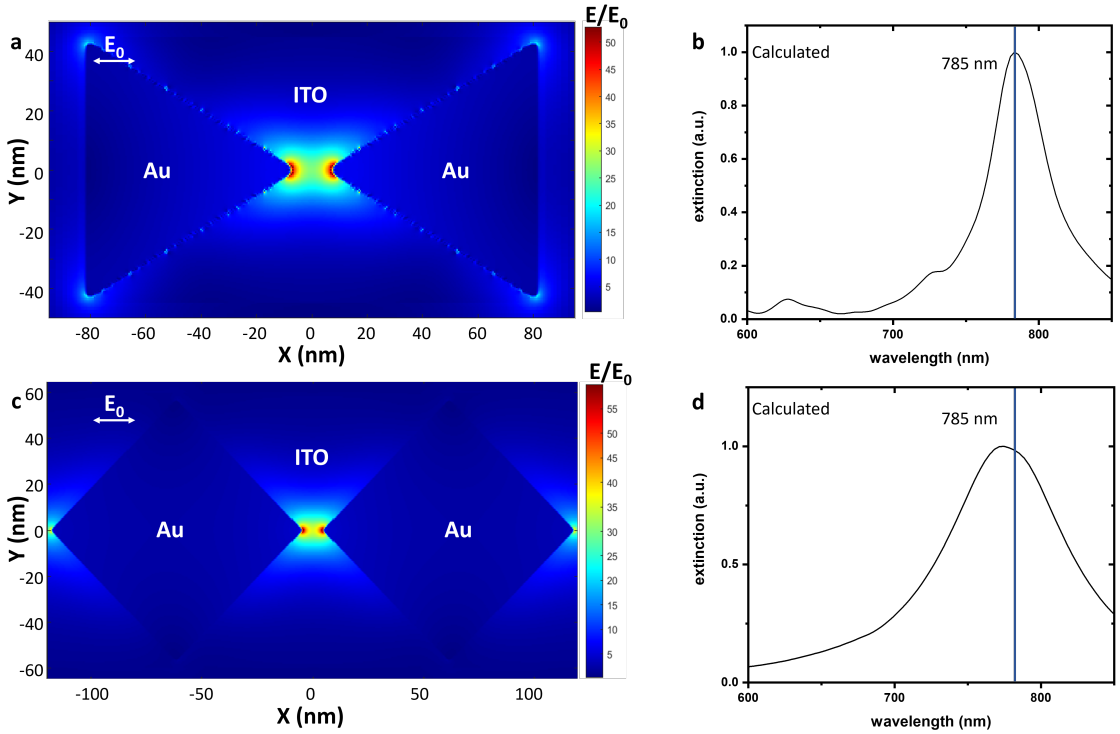

Figure 5.2: Results of the simulations used to design Au bowtie and nanodiamond structures that support LSPR at 785 nm on an ITO substrate. (a) and (c) show the simulated field enhancement for bowties and nanodiamonds respectively at 785 nm. (b) and (d) show the normalised calculated extinction spectra for bowties and nanodiamonds respectively. The blue line at represents the target resonant wavelength of 785 nm. A mesh size of $0.5 \times 0.5 \times 0.5$ nm was used for all calculations.

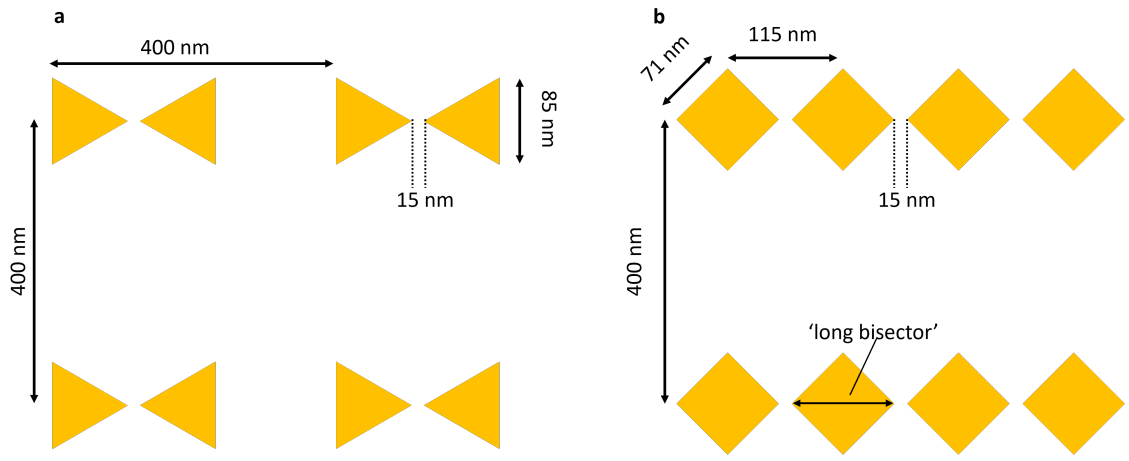

Figure 5.3: Schematic showing the dimension of (a) bowties and (b) nanodiamonds fabricated using EBL. A 1 nm layer of Ti was first deposited as an adhesive layer, followed by 20 nm Au for all structures.

sities for the bowties and nanodiamonds are $|\mathbf{E}^2| = 2500$ and $|\mathbf{E}^2| = 3025$ respectively. It can be seen that the nanodiamonds exhibit strong field enhancement at both sides due to the symmetry of the structure as well as the close proximity to other nanodiamonds on either side. It would be possible to further increase the number of plasmonic hotspots while eliminating the polarisation dependence of this design by reducing the period in the *x* direction to match with the period of the *y* direction. It was decided to keep a larger *y* period here as structures with this high a density would yield a large proximity effect, making fabrication via EBL challenging. Simulated extinction spectra for bowties and nanodiamonds are shown with the 785 nm laser line marked in each spectrum. It can be seen that both structures have good overlap with the laser line and should therefore support LSPR at this frequency.

5.3.2 Fabricated Au Bowties and Nanodiamonds on ITO

Figure 5.4 shows SEM images of the bowtie and nanodiamond structures fabricated on ITO coated glass bulk substrates using EBL. The structures are fabricated using a 1 nm Ti layer as an adhesive layer, followed by deposition of 20 nm Au. For both bowties and nanodiamonds, the side length of the fabricated structures was measured as 86 ± 4 nm and 70 ± 2 nm respectively, equalling the target lengths. The gap sizes between bowties were measured as 16 ± 2 nm and measured gaps for nanodiamonds were 20 ± 2 nm.

This difference is accounted for as the long bisector of the nanodiamonds was measured as 96 $\pm$ 2 nm instead of the intended 100 nm. The change in length occurs due to the larger radii of curvature for the apexes of both the bowties and nanodiamonds. This is because during the electron beam exposure, perfect equilateral triangles and square shapes are selected as target geometries to pattern the sample. The sharp edges of these shapes are rounded when the structures are fabricated yielding slightly reduced edge lengths and gaps between pairs of structures. The measured extinction spectra are slightly blueshifted relative to the simulated spectra. This could be due to the slight difference the dimensions of the simulated and fabricated structures, as well as due to a difference between the simulated and experimental ITO layer thickness and refractive index. In particular, it can be seen that the measured extinction spectrum from the nanodiamonds is significantly blueshifted away from the target resonance wavelength of 785 nm. Adjusting the exposure dose could help to fabricate structures with smaller gaps, however as the experiment is taking place in a higher index diphenylgermane medium the LSPR wavelength will be red-shifted, meaning that the overlap with the 785 nm laser line will be increase during the experiment.

5.3.3 Growth of Ge on Bulk ITO on Glass Substrates

SEM images of the bowtie and nanodiamond structures after laser induced growth experiments are shown in Figure 5.5. The laser power was varied from 30-60 mW. As can be seen from the SEM images, material has grown on both bowtie and nanodiamond structures, however the extent of growth is much larger for the nanodiamonds, likely due to the greater overall light absorption due to the higher density of structures in the array. For the bowties it can be seen that the grown material is localised to the surface of individual pairs of bowties, whereas for the nanodiamonds at 30 mW laser power the material covers a much larger area, but is still located almost exclusively in contact with the nanodiamonds. When a high (60 mW) laser power is used for the nanodiamonds, it can be seen that there is extremely dense growth of material, covering an area with an approximate radius of 10 μm, much larger than the spot size of the laser, which has a radius $<$ 2 μm. Nanowires with lengths $>$ 10 μm can be seen, indicating that crystalline

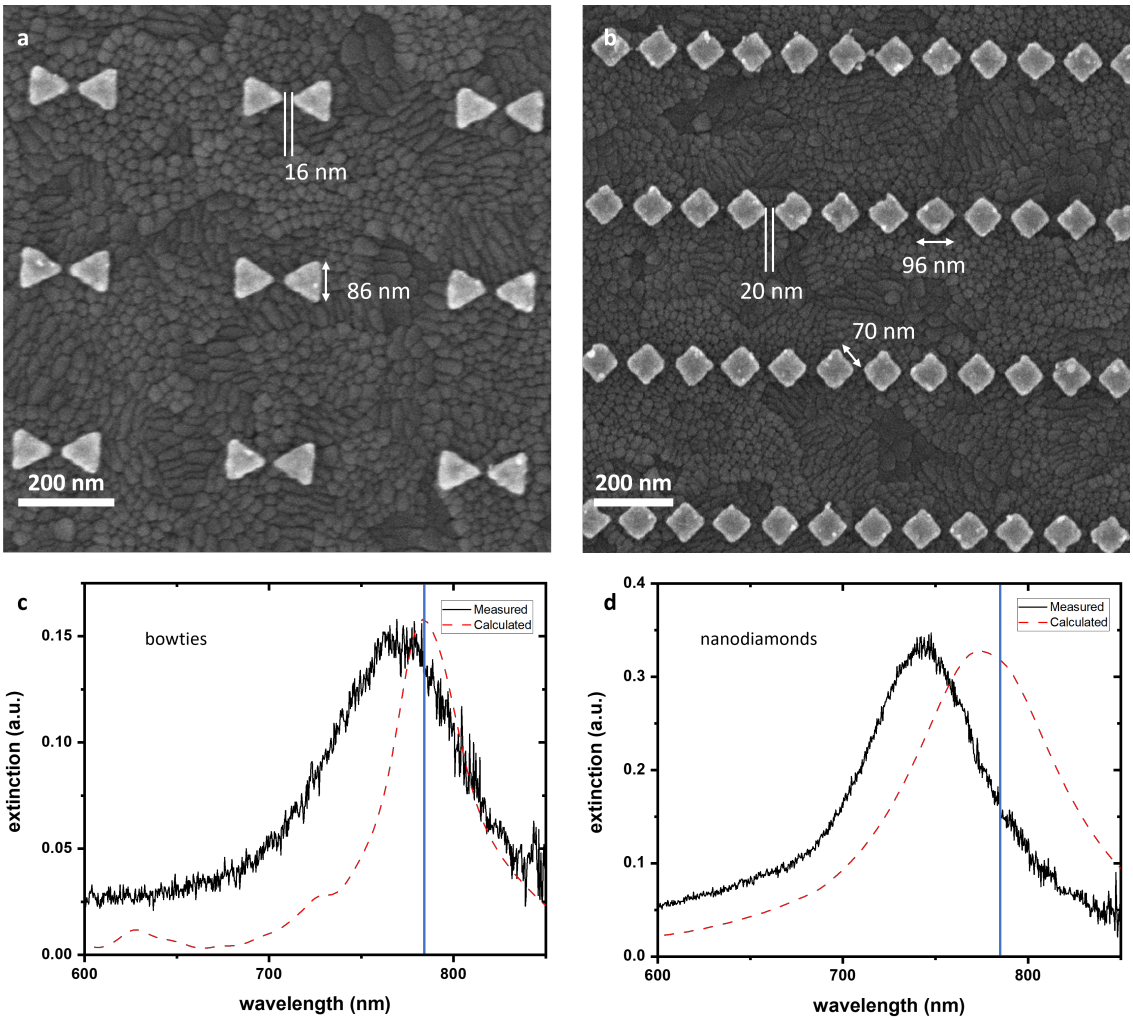

Figure 5.4: Au (a) bowties and (b) nanodiamonds designed to support LSPR at 785 nm fabricated on an ITO substrate using EBL. (c) and (d) show both measured and calculated extinction spectra for bowties and nanodiamonds respectively. The calculated spectra have been normalised to the measured data. The blue line at 785 nm in each spectrum represents the wavelength of the laser used for SLS growth.

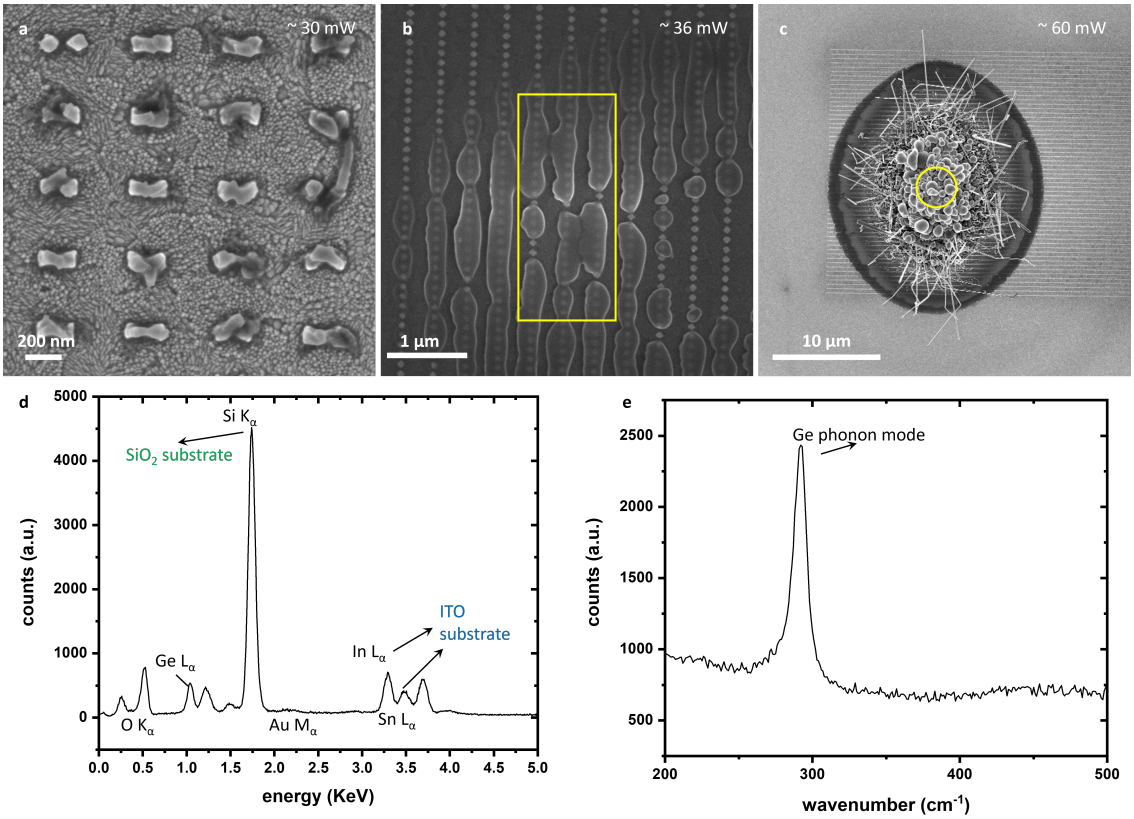

Figure 5.5: (a-c) SEM images of Au bowties and nanodiamonds after the laser-driven SLS growth process. (a) Bowties after being exposed to 30 mW laser irradiation for 200 s. (b) Nanodiamonds after being exposed to 36 mW laser irradiation for 30 s. (c) Nanodiamonds after being exposed to 60 mW laser irradiation for 10 s. (d) EDX spectrum recorded from the region outlined by the yellow rectangle in (b). (e) Raman spectrum recorded from the region outlined by the yellow circle in (c) highlighting the Ge phonon mode at 300 cm^{-1}.

Ge has grown via the SLS process.

Raman spectroscopy of the region of dense growth at 60 mW laser power yielded a peak near 300 cm^{-1}, corresponding to the characteristic phonon mode of crystalline Ge. The presence of this peak could not be confirmed for the case of Ge growth induced by lower laser intensities, however Raman signals have intrinsically low intensities and would therefore be difficult to observe from the low density growth seen on the bowties. It would be expected, however that some signal would be detected from the denser growth seen for the 30 mW exposure, but this was not observed. Energy dispersive x-ray spectroscopy (EDX) was used to further probe this region, and the presence of a peak near 1.1 keV corresponds to the L_α peak of Ge, indicating that this grown material is Ge.

It is theorised that this is amorphous Ge deposited onto the Au nanodiamonds as the diphenylgermane precursor decomposes.

5.3.4 Fabrication of Au Nanodiamonds on SiN_x Membranes for TEM

To further probe the grown Ge, nanodiamond structures were fabricated on 10-nm-thick SiN_x membranes to allow for TEM analysis of the structures. Each TEM grid consists of eight 100 $\times$ 100 μm windows and one 200 $\times$ 100 μm window. Due to the limited space on each grid, as well as the added difficulty in fabricating on such delicate membranes, it was decided that initially only the nanodiamond structures would be fabricated, as these structures had displayed a much greater magnitude of Ge growth than the bowties, as shown previously. FDTD calculations were repeated to determine the optimal dimensions for Au nanodiamonds on a 10 nm SiN_x membrane, the results of which are shown in Figure 5.6. It was found that a side length of 80 nm, corresponding to a long bisector length of 113 nm was found to be the optimum size to support a LSPR at 785 nm. A gap size of 10 nm was selected. The use of a thin membrane rather than a bulk substrate will reduce proximity effects during fabrication and therefore a smaller gap size should be achievable. Figure 5.6(a) indicates a reduced field enhancement of $|\mathbf{E}^2| = 1225$ for nanodiamonds on a SiN_x substrate compared to $|\mathbf{E}^2| = 3025$ previously calculated for nanodiamonds on an ITO substrate. The value of refractive index used for SiN_x was taken to be 2 at 785 nm.[188] The refractive index for ITO was taken to be 1.6 at 785 nm.[190] It has been shown that substrates with a higher refractive index play a significant role in the redistribution of dipoles when the LSPR is excited, resulting in a weakening in the intensity of the plasmonic hot spots.[306]

SEM images of the nanodiamond structures fabricated on SiN_x TEM grids are shown in Figure 5.7, alongside their measured extinction spectrum. The side length of the fabricated nanodiamonds was measured as 82 $\pm$ 4 nm, while the long bisector was measured as 110 $\pm$ 3 nm. The gap size was measured to be 10 $\pm$ 3 nm. The difference between targeted and measured lengths is attributed to the intrinsic variation in feature sizes, as well as the larger radii of curvature in the fabricated structures compared to the target design. The measured extinction spectrum is blueshifted compared to the calculated spectrum.

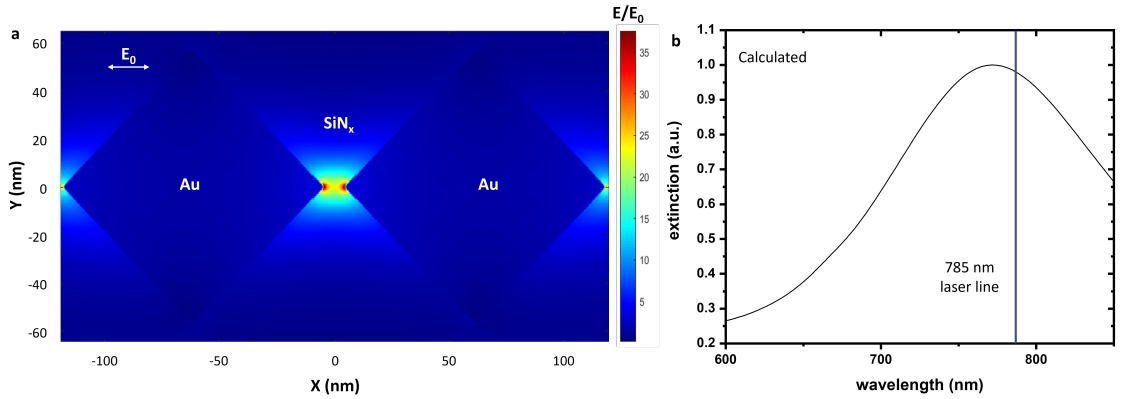

Figure 5.6: Simulated (a) field enhancement at 785 nm and (b) extinction spectra for Au nanodiamonds on a 10 nm thick SiN_x membrane. The blue line in the extinction spectrum represents the target resonance wavelength of 785 nm. A mesh size of 0.5 × 0.5 × 0.5 nm was used for all calculations.

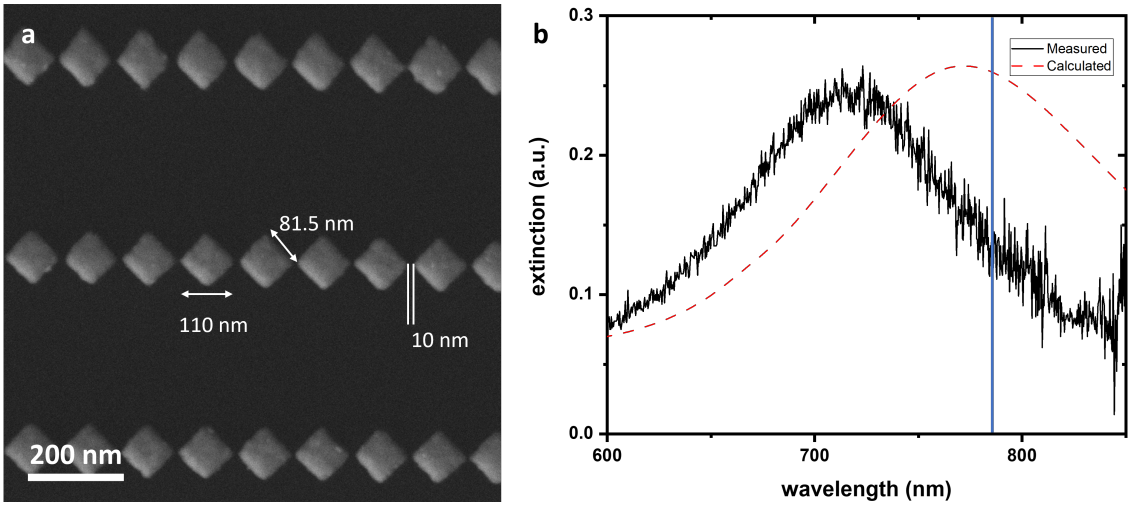

Figure 5.7: (a) SEM image of 20 nm thick Au nanodiamonds fabricated on a 10 nm thick SiN_x TEM membrane. (b) Measured and calculated extinction spectra for Au nanodiamonds on an 10 nm thick SiN_x membrane. The calculated spectrum is normalised to the measured spectrum. The blue line represents the target resonance wavelength of 785 nm.

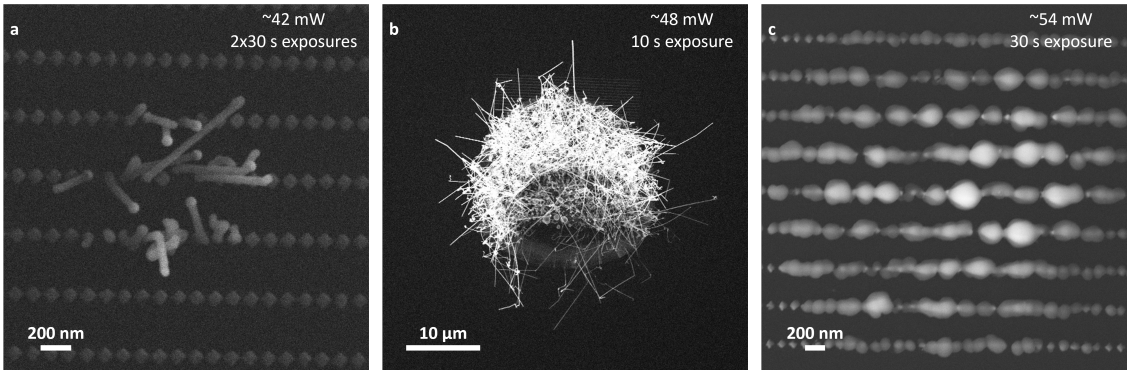

Figure 5.8: SEM micrographs of Ge growth on Au nanodiamonds on a SiN_x substrate. (a) NWs grown after 2 $\times$ 30 s exposures to a 785 nm laser with a power of 42 mW. (b) Dense NW growth after 10 s of exposure to a 785 nm laser with a power of 48 mW. (c) Amorphous growth of Ge after 30 s of exposure to a 785 nm laser with a power of 54 mW.

However, as diphenylgermane is used as the medium during laser exposure and has a higher refractive index of 1.6,[307] the LSPR is expected to be redshifted towards the laser wavelength of 785 nm.

5.3.5 Growth of Ge on TEM Membranes

SEM images of the nanodiamond structures after immersion in diphenylgermane and laser exposure are shown in Figure 5.8. Figure 5.8(a) shows the nanodiamond structures after two 30 s exposures to a laser with a wavelength of 785 nm and an incident power of 42 mW. This exposure has resulted in the formation of short nanowires. Figure 5.8(a) shows an array of nanodiamonds exposed to a laser with a power of 48 mW for 10 s, resulting in expansive growth of Ge seen in the earlier experiment. Interestingly, for a 30 s exposure with a laser power of 54 mW, growth of amorphous Ge was observed.

TEM was used to further probe the structure of the grown material, the results of which are shown in Figure 5.9. Figures 5.9(a) and 5.9(b) show the Ge NWs seen in Figure 5.8(a). From Figure 5.9(b) the interface between the Au nanoparticle and crystalline Ge can be clearly seen. Conversely, this structure is not present in Figure 5.9(d) confirming, as suspected that this material is not crystalline. Furthermore, it can be seen in Figure 5.9(a) that the Au nanodiamond has lost most of its sharp features. This is due to the melting of the particle during the SLS growth process. The nanodiamonds coated with

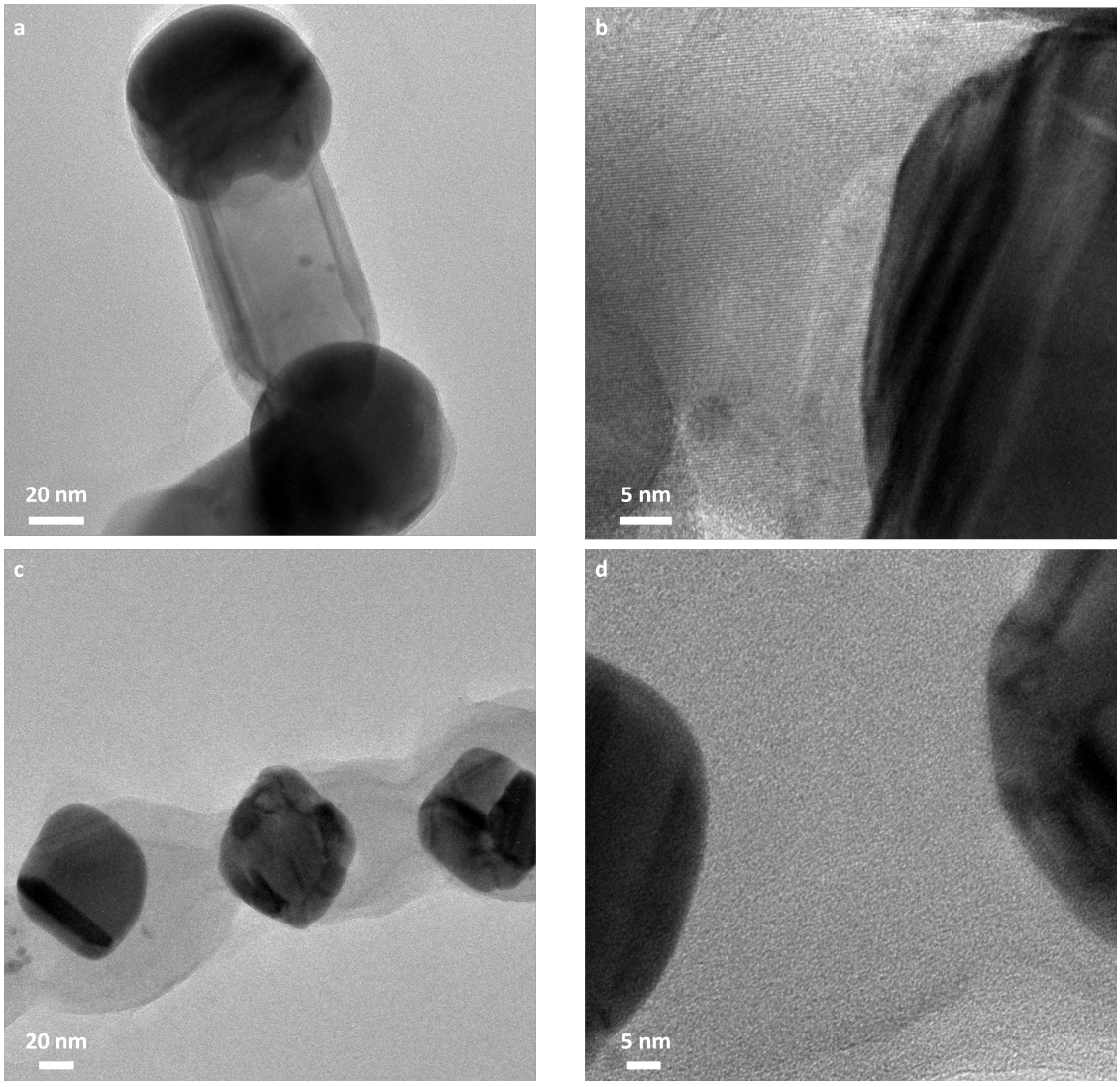

Figure 5.9: TEM micrographs of (a-b) crystalline and (c-d) amorphous Ge grown via laser-induced SLS growth. The dark regions in each image are the Au nanoparticles, while the lighter material is Ge.

amorphous material have retained their shape indicating that they have not reached a sufficient temperature to initiate the SLS growth process.

5.3.6 Elemental Analysis

EDX spectra from both crystalline and amorphous Ge are shown in Figure 5.10. Both Ge K_α and L_α peaks can clearly be seen in both spectra. The presence of these peaks in Figure 5.10(b) is confirmation that the material grown is Ge. The lack of any observed crystallinity for this material indicates that it is amorphous Ge. The Au M_α peak is

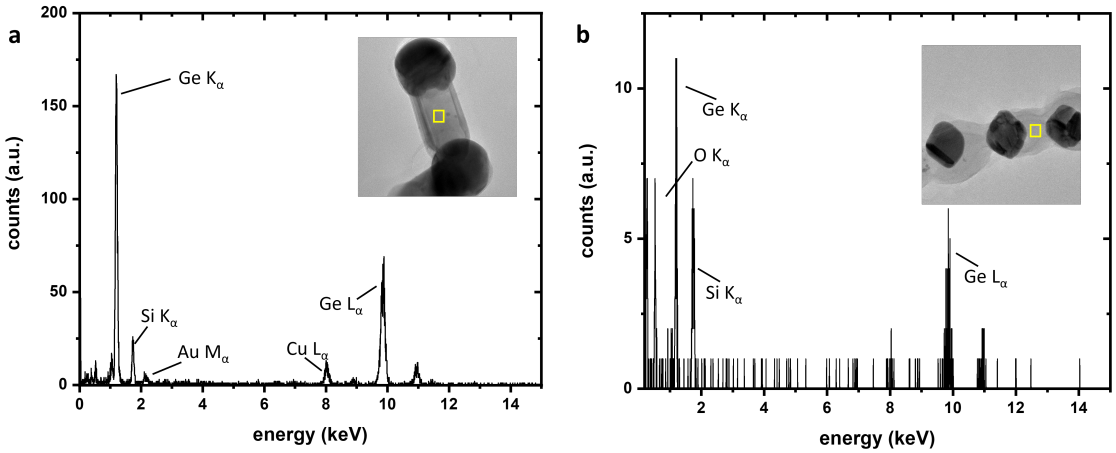

Figure 5.10: EDX spectra recorded from (a) crystalline and (b) amorphous Ge grown via laser-induced SLS growth. The yellow rectangle in the inset TEM micrographs represent the region from which each spectrum was collected.

present in the crystalline Ge spectrum as during the SLS growth process some of the seed metal nanoparticle can precipitate into the NW. The lack of this peak in Figure 5.10(b) is further evidence that the amorphous Ge is not being grown via the SLS process. The presence of the Si K_α is due to both the EDX detector, as well as the TEM grid which is SiN_x supported by Si. The presence of the Cu L_α peak is due to Cu present within the TEM.

Figure 5.11(b) shows the Raman spectrum collected from short Ge NWs shown in Figure 5.11(a), as well as the spectrum from a reference crystalline Ge film on a bulk Si substrate. The peak at 300 cm^{-1} is attributed to the transverse optical phonon mode of crystalline Ge. The fact that this peak can be detected despite the low volume of Ge present is likely due to enhancement of the Raman signal due to LSPR of the Au nanoparticles. From the extinction spectrum in Figure 5.11(c) it can be seen that despite the reshaping of the nanoparticles due to the SLS growth process, they still support a LSPR around 785 nm. The spectrum has been redshifted after the laser exposure process. This is likely due to the coating of the nanodiamonds by organic residue remaining from the diphenylgermane precursor after the exposure process, as well as due to the reshaping of the nanodiamonds. It can be seen from Figure 5.11(c) that the LSPR peak maintains good overlap with the 785 nm laser, and as the Raman spectrum is collected in air there will be no further shift in this peak during the collection of the signal. Consequently, the

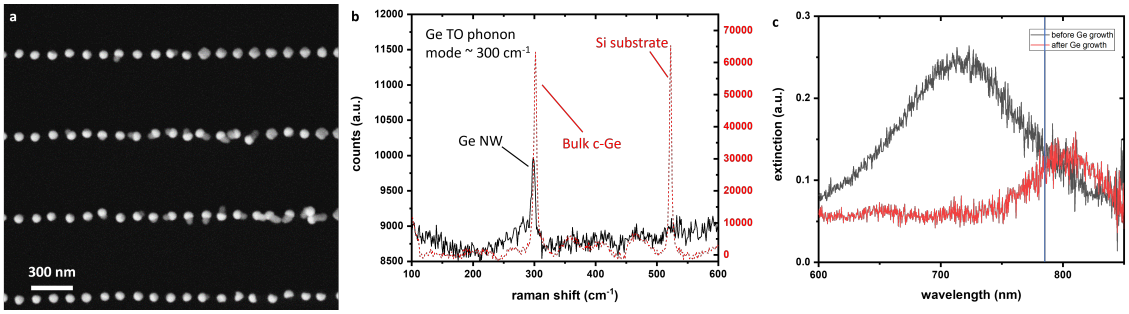

Figure 5.11: (a) SEM micrograph of short Ge NWs growth by terminating the SLS growth process early. (b) Raman spectrum collected from the Ge NWs shown in (a). The dashed red line is the Raman spectrum recorded from a reference crystalline Ge on a bulk Si sample. (c) Extinction spectra recorded from Au nanodiamonds before (black) and after (red) the laser-induced SLS growth process. The blue line at 785 nm represents the laser wavelength used during the SLS growth process, as well as while recording the Raman spectrum.

nanodiamonds provide sufficient enhancement to the Raman signal from the crystalline Ge to allow the signal to be detected. The ability of these nanoantennas to support SERS is a further benefit of using LSPR to induce the growth of semiconductor materials.

5.3.7 Mechanism of SLS Growth of Ge Nanowires

Chockla *et al.*[294] proposed that during the SLS growth process, diphenylgermane first undergoes a phenyl redistribution, leading to the formation of tetraphenylgermane and germane (GeH_4) in solution as end products. Germane subsequently undergoes thermal decomposition to atomic Ge, which diffuses to the Au nanocrystal. Other heterogeneous decomposition pathways were deemed unlikely by the authors as they require the adsorption of multiple phenylgermane molecules to the surface of the Au nanocrystals.

From Figure 5.8 it can be seen that a small change in laser power can result in drastically different growth regimes. As the GeNWs grow, the composite Ge-Au nanostructure absorbs more light due to the increase in the optical cross-section, leading to a continuous increase in the temperature of the nanostructure during the growth process. This continuous heating can lead to temperatures high enough to lose the selectivity of the NW growth process, and instead result in exponential pyrolytic growth of Ge, as seen in Figure 5.8(b).[298] At lower powers, the growth is slower and can therefore be more easily

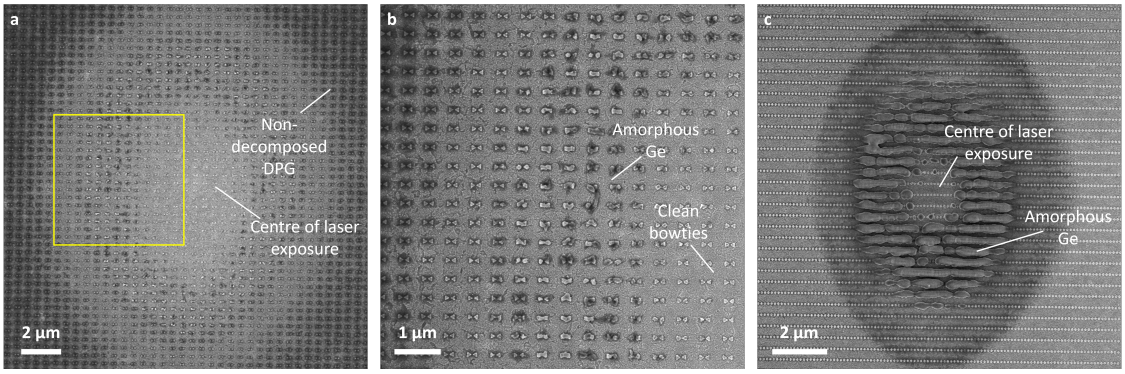

Figure 5.12: SEM micrographs showing the growth of amorphous Ge on bowties (a-b) and nanodiamonds (c) on an ITO substrate. (b) is the region outlined by the yellow square in (a). In each array of nanoantennas the region at the centre of the laser exposure is clean and no growth is observed. Amorphous Ge is deposited on antennas in a ring around the centre of the laser exposure. The outermost dark region is likely non-decomposed diphenylgermane also deposited via the coffee-ring effect.

controlled to achieve shorter nanowires as seen in Figures 5.8(a) and 5.11(a).

At higher laser powers, the growth of amorphous Ge dominates. During the laser exposure, the formation of bubbles was observed. The formation of these bubbles could lead to a local depletion of diphenylgermane around the nanoantennas that are being exposed by the laser. Furthermore, the bubbles could result in coffee-ring like deposition of the diphenylgermane precursor at the edge of the bubbles. This is supported by the low-magnification SEM images of the arrays of nanoantennas where amorphous growth was observed. The centre of the region that was exposed by the laser is pristine, while the edges of this region are darker. It is in this darker region where the amorphous growth occurred. It is possible that the diphenylgermane underwent thermal decomposition to elemental Ge as proposed by Chockla *et al*, however this elemental Ge was then carried away from the exposed Au nanoantennas preventing the SLS growth process from occurring. This elemental Ge was subsequently deposited onto the surface of the 'colder' nanoantennas further away from the centre of the laser exposure. Melting of the nanoantennas does not appear to occur in this outer region, indicating that these antennas are not reaching sufficient temperatures for SLS growth to occur.

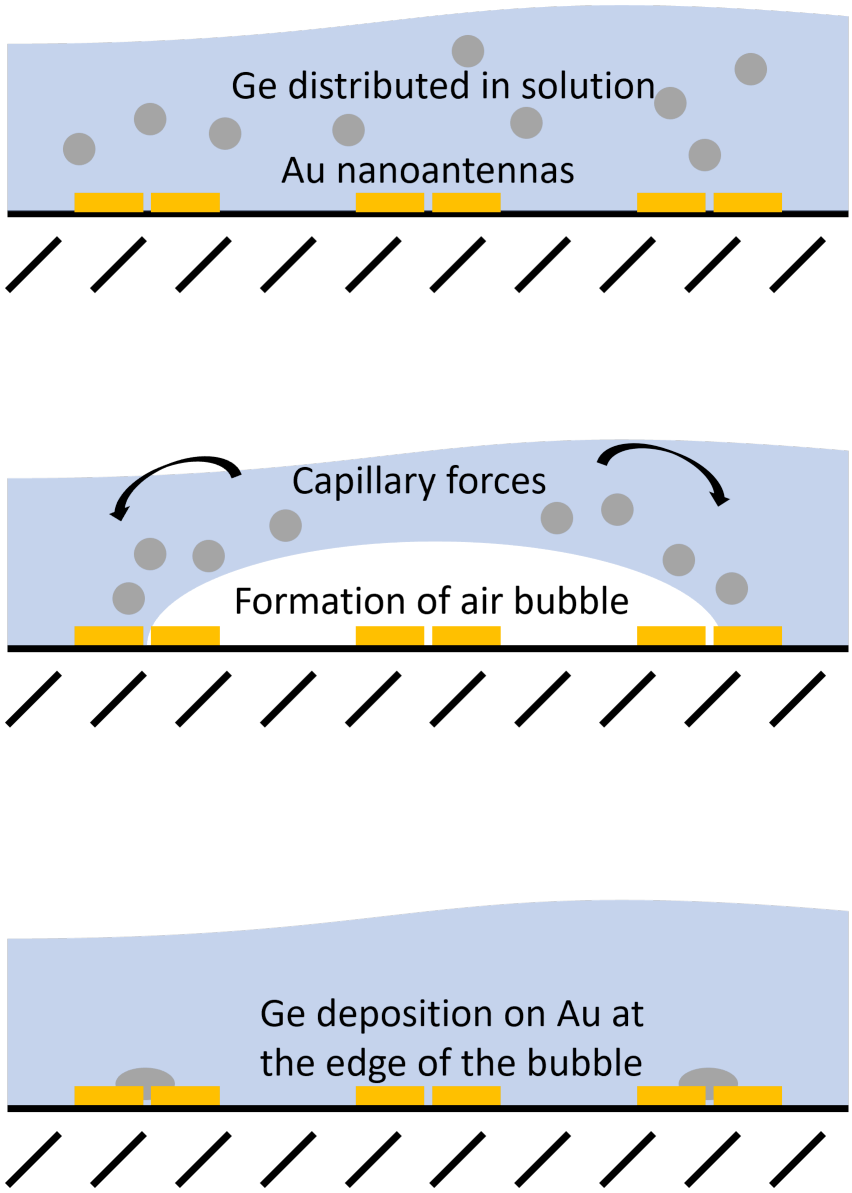

Figure 5.13: Deposition of Ge on Au nanoantennas via the coffee-ring effect. Diphenylgermane thermally decomposes to elemental Ge in solution under laser illumination. Heating of the nanoantennas at the centre of the laser exposure results in the formation of air bubbles around the nanoantennas. Capillary forces drive the elemental Ge around the edge of the bubble, resulting in the deposition of amorphous Ge on the nanoantennas at the edge of the bubble.

5.3.8 Plasmon-Induced Growth of ZnO

To investigate the suitability of this method to the growth of other semiconductor materials, we aimed to grow ZnO NWs using the same experimental setup. Bowties and nanodiamonds were fabricated on a bulk ITO substrate using EBL with the same target dimensions as outlined previously. The ZnO precursor consisted of a 1:1 mixture of aqueous 75 mM zinc nitrate hexahydrate and aqueous 75 mM hexamethylenetetramine (HMTA) as used previously by Fujiwara *et al.* for plasmon-assisted synthesis of ZnO NWs.[302]

Preliminary results of the LSPR-induced growth of ZnO are shown in Figure 5.14. It can be seen that with low exposure times that there is extensive growth of what is proposed to be ZnO on the surface of the arrays of plasmonic nanostructures. From Figure 5.14(b) it can be seen that it appears that the growth originates at the surface of the Au nanoantenna as expected, however there is no apparent melting of the Au nanoparticle. Furthermore, the diameter of the grown material appears to be independent of the size of seed Au nanoparticle, as can be seen by the large grown structures in Figures 5.14(c) and 5.14(d). The larger structures are formed due to the merging of NWs originating from nuclear sites in close proximity to one another.[308] These factors indicate that the mechanism for the growth of ZnO is not the VLS mechanism previously observed for the growth of Ge NWs. Instead, the ZnO growth proceeds via a hydrothermal growth mechanism.[309,310] In water, HMTA readily hydrolyzes and produces HCHO and NH_3. The NH_3 produced supplies a basic environment that is necessary for the formation of $Zn(OH)_2$, while also stabilising the Zn^{2+} ions in solution. Under heating, $Zn(OH)_2$ dehydrates to ZnO NWs.[310] This hydrothermal synthesis occurs at temperatures of 90 $^\circ$ C, significantly lower than the temperatures required for the VLS growth of Ge.[309] Lower reaction temperatures would explain why no melting of the Au bowties was observed. The role of the plasmonic Au nanostructures is to act as heat sources to drive the hydrothermal reaction, and also to act as seeds from which the ZnO NWs can nucleate from.[311]

Figures 5.14(e) and 5.14(f) show bowtie structures that were overexposed during EBL patterning resulting in the bowtie structures becoming fused. These bowties were exposed under the same conditions as the bowties shown in Figure 5.14(a) and 5.14(b) and

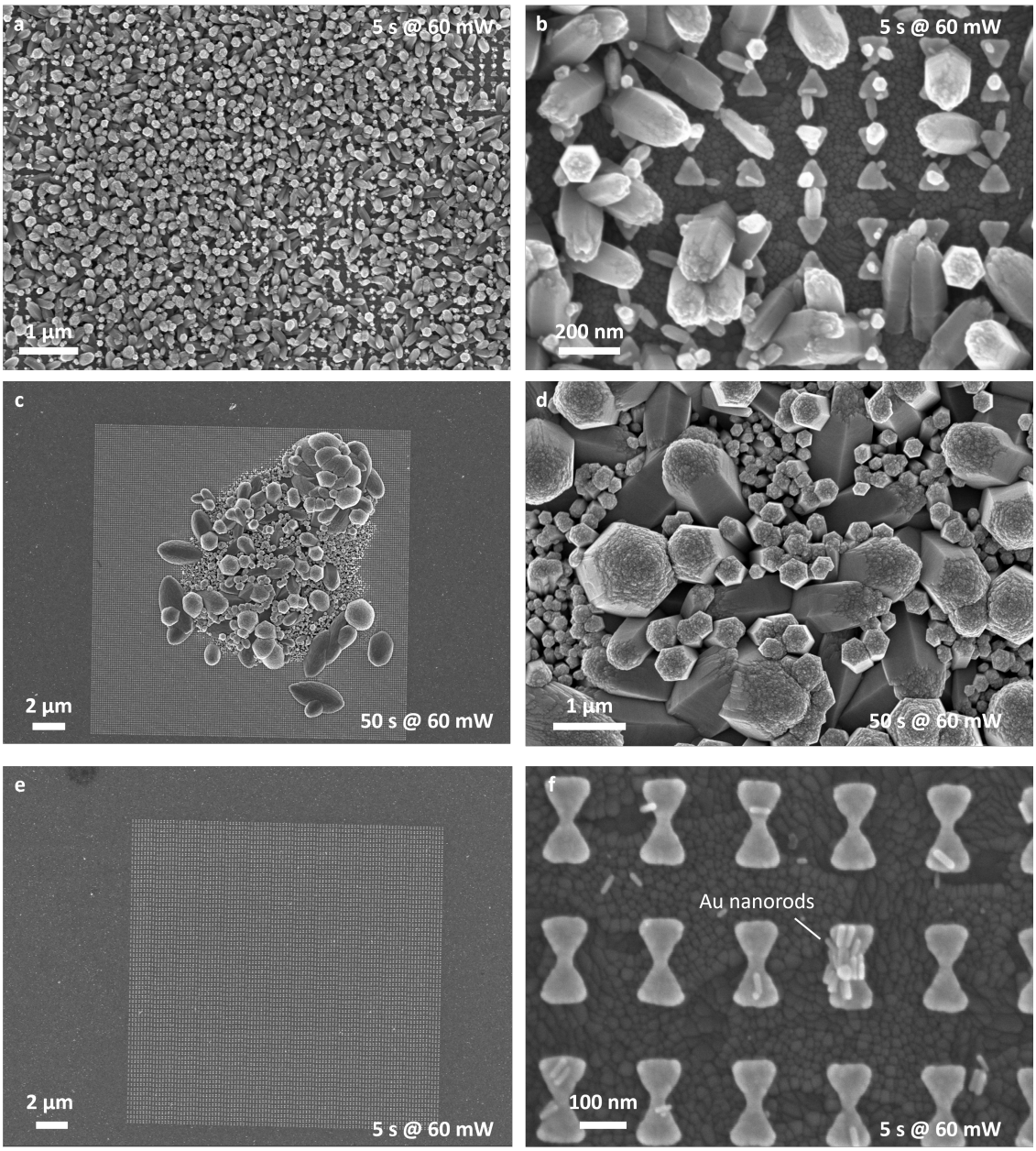

Figure 5.14: Preliminary results of LSPR-induced growth of ZnO nanowires.(a)-(d) ZnO NWs grown via a hydrothermal mechanism driven by localised heating of plasmonic Au bowtie structures. (e)-(f) Over exposed bowties that do not support LSPR at the desired resonance. The lack of observed growth indicates that the LSPR is the driving factor of the ZnO NW growth.

no growth of ZnO was observed. This result shows that it is the presence of LSPR at the correct frequency that drives the reaction rather than direct heating of the precursor materials by the laser. The nanorod structures that are visible are Au nanorods resonant at 785 nm that were added to the reaction mixture to enhance plasmonic effects during laser exposure, however no noticeable effect was observed.

5.4 Outlook

The LSPR-induced SLS growth of Ge NWs outlined here holds great promise for the fabrication of nanocrystalline Ge for microelectronic applications. The use of EBL to fabricate the resonant nanoantennas allows for precise control of the on-chip location of the nanoantennas, and consequently the location of the Ge nanocrystals. Furthermore, EBL can used to fabricate individual antennas, allowing for the growth of individual nanocrystals. As shown in this work, multiple nanoantenna geometries can be used to grow Ge so the nanoantenna geometries can be adapted to fit different chip designs. EBL also facilitates the use of different metal nanoantennas, allowing the LSPR-induced SLS growth process to be adapted to a variety of different crystalline semiconductors, operating across a range of laser wavelengths.

Throughout the experiments in this work undiluted diphenylgermane was used. Mullane *et al*[312] demonstrated that the length of Ge nanowires produced by the pyrolysis of phenyl germanes can be controlled by diluting the phenyl germanes with a high boiling point solvent such as squalane. The rate of NW growth in this work was highly sensitive to the incident laser power. Dilution of diphenylgermane could slow the rate of growth, allowing for greater control over the size of the nanocrystals produced.

A further benefit of this approach is that both the amorphous and crystalline Ge are grown in direct contact with the metallic nanoantennas. To date, photodetectors with a bandwidth greater than 100 GHz have been developed by fabricating amorphous Ge in the gap between two plasmonic Au resonators.[313] In this work by Salamin *et al* however, Ge was deposited onto the Au resonators by means of thermal evaporation. The method of fabricating amorphous-Ge directly onto Au nanoantennas outlined in our work could

allow for the production of similar devices, with a greater degree of control, and on a sub-100-nm scale. Additionally, the fabrication of semiconductor materials in direct contact with a plasmonic nanoantenna with its LSPR tuned to the bandgap of the semiconductor could lead to the strong coupling of the semiconductor and the plasmonic nanoantenna.

We have also presented preliminary results for the LSPR-induced growth of ZnO NWs based on the method outlined by Fujiwara *et al.*[302] In this case it was found that the growth proceeded via a hydrothermal reaction instead of via the VLS mechanism observed for the growth of Ge. This result highlights the versatility of plasmonic nanoparticles in the growth of semiconductor materials as we have demonstrated growth of two different semiconductors that proceeds via two different reaction mechanisms, both of which are driven by the excitation of LSPR.

Chapter 6

Conclusions

6.1 Thesis Summary

The objectives of this thesis were to study the limits of high-resolution lithography techniques such as EBL and HIBL, and to investigate their applications in the study of plasmonic materials and devices. The plasmonic properties of metallic nanoparticles is strongly dependent on their dimensions. Furthermore, next-generation plasmonic devices will require precise control over their on-chip location. Electron and He^+ ion beam lithography offer the ability to fabricate metallic nanostructures with arbitrary 2-D geometries, with exact control over on-chip placement, making them ideal candidates for the study of plasmonic nanoparticles.

In Chapter 3, we simulated and measured the He^+ ion PSFs for negative-tone PMMA and a fullerene-derivative resist on ultrathin membranes. PSFs reveal information about the lateral spread of energy deposited by an incident beam of electrons or He^+ ions in a resist. Accurate knowledge of PSFs allows for corrections to be made to the beam dose for an exposure to reduce proximity effects, thereby improving the resolution of the fabrication process. PSFs were measured by carrying out a series of point exposures with varying dose, and plotting the radii of the negative-tone structures produced vs the inverse exposure dose. The smallest structure produced using PMMA was measured as having a radius of 3.2 nm, whereas for the fullerene-derivative resist the minimum

resolvable feature size had a radius of 2.7 nm. The fullerene-derivative also required a higher exposure dose, indicating that is could be a good candidate as a next-generation lithographic resist.

The PSFs were also calculated using the model proposed by Winston *et al.*,[196] and the results were found to be in good agreement with the experimental data. Measured PSFs were also fitted with both a power law and with a function resembling a low-pass filter function. Fitting with these functions allowed for direct comparison between our results and the results of similar work measuring the PSF of PMMA when exposed with an aberration-corrected electron beam in a STEM.[136] Dose contrast calculations predicted that for He^+ ion beam exposure with a PSF radius of 0.85 nm, superior contrast is achievable in both PMMA and the fullerene-derivative for pitches above 2 nm when compared to a similar exposure using an aberration-corrected electron beam with a PSF radius of 0.5 nm. When compared to an aberration-corrected EBL process with a PSF radius of 0.85 nm, it was proposed that HIBL can achieve superior dose contrast for all pitches for both resists. We propose HIBL as a superior alternative to EBL for the patterning of dense arrays of nanostructures owing to the simplicity of our He^+ setup compared to the aberration-corrected EBL setup.

In Chapter 4 we proposed a design for a segmented plasmonic antenna to probe coupling between a plasmonic cavity and the vibrational mode of a molecule. The segmented antenna is designed to support two distinct resonances. One of these resonances is designed to be in the mid-IR part of the spectrum to match with the vibrational mode chosen for coupling. Here, we targeted a LSPR wavelength of 6250 nm (1600 cm^{-}) to match with the graphitic G band peak of a carbon nanodot. This peak was chosen as we have demonstrated that a carbon nanodot can be fabricated in the centre of a plasmonic hot spot using EBL, and that the peak from an individual nanodot fabricated in the centre of a plasmonic antenna can be detected with Raman spectroscopy. The second resonance is designed to be in the near-IR region to match with a Raman laser so that the antenna can support SERS to facilitate the detection of the vibrational strong coupling. Here, a wavelength of 785 nm was chosen as Au exhibits better plasmonic properties in the NIR part of the spectrum. Furthermore, 785 nm laser yield a reduced fluorescence background

than 532 nm or 633 nm lasers, facilitating the detection of low intensity signals.

Optical and NIR extinction spectra confirmed the presence of a broad peak around 785 nm to match with the target NIR wavelength. Raman spectra collected from segmented antennas fabricated on an ITO substrate indicate the presence of peak at the desired wavenumber of 1600 cm^{-1}. Segmented antennas were fabricated on a SiN_x membrane to allow IR spectra to be collected from the antennas to confirm the presence of the LSPR at 1600 cm^{-1}. IR spectra recorded from a segmented antenna revealed a peak at 1739 cm^{-1}. It is known that the PMMA carbonyl stretching mode has a frequency around 1730 cm^{-1}.[259] Therefore it could not be confirmed whether the observed peak is due to a plasmonic mode in the segmented antenna or due to the presence of PMMA residue leftover from the lithography process.

Using the values for the FWHM of the measured Raman peak of a graphitic carbon nanodot and the simulated mid-IR LSPR peak of the segmented antenna, a Rabi splitting energy of 21.4 meV was predicted for the strongly coupled system using the model used by Pelton *et al.*[260] This Rabi energy is larger than the splitting energies previously reported for VSC with both a Fabry-Pérot cavity and a surface lattice resonance.[245,250] These results indicate that by using a plasmonic antenna similar to what we have proposed here could achieve stronger VSC than has been reported to date.

The LSPR-induced growth of semiconductor materials Ge and ZnO were investigated in Chapter 5. Au nanoantennas were designed to be resonant at 785 nm to match with the laser used to drive the semiconductor growth. Au bowties and nanodiamonds were first simulated and then fabricated on bulk ITO substrates using EBL. Initial results for the growth of Ge revealed that for high laser intensities, dense NW growth was observed, whereas at lower intensities the grown Ge was more localised around the plasmonic bowties. EDX and Raman spectroscopy were employed to probe the grown material, and confirmed the presence of Ge.

To further investigate the growth of Ge, Au nanodiamonds were fabricated on TEM membranes. Laser exposure at varying intensities revealed three different growth regimes. At lower intensities, short Ge nanowires are grown. These nanowires were capped with spherical nanoparticles, indicating that they are grown via a solution-liquid-solid mecha-

nism. At slightly higher intensities, there is rapid and expansive growth of Ge nanowires. This rapid growth is attributed to increased optical cross-section of the Ge-Au nanostructures, resulting in a continuous increase in the temperature around nanostructures. At higher intensities, amorphous growth of Ge is observed. This amorphous growth is attributed to coffee-ring deposition of elemental Ge on the surface of the Au nanoparticles due to the formation of bubbles in the reaction mixture at elevated temperatures. TEM and Raman analysis of the grown NW structures confirmed the growth of crystalline Ge NWs. Ge was confirmed to be present in the amorphous material, indicating that it is amorphous Ge.

The method used for the growth of Ge was also used to grow ZnO nanowires. In this case the reaction proceeds via a hydrothermal mechanism rather than the SLS mechanism observed for the growth of Ge NWs. It was found that growth is seeded by the Au nanoparticles and that NWs that are in close proximity to each other can fuse to form larger structures. No growth of ZnO was observed on structures that were overexposed during EBL fabrication and therefore didn't support LSPR at the correct wavelength, highlighting the importance of LSPR in this growth mechanism.

6.2 Future Directions

Accurate knowledge of the PSF of a resist-beam system allows for corrections to be made to the dose received by the resist, thereby improving the resolution of the exposure process. Furthermore, accurate PSFs allow for direct comparison between different resist materials and between electron and He^+ ion beam processes. Consequently, measuring the PSF of well established and emerging resist materials will allow for direct comparison between resists and aid in the search for the next generation of lithographic resists.

Emerging techniques such as AFM-IR allow for the spatial mapping of the chemical change in resist materials.[236,237] AFM-IR could be used to map the spatial distribution of a peak that is only present in an exposed resist. This would allow for the measurement of the PSF of a resist prior to the development step, therefore collecting information about the spatial extent of the resist exposure that is typically lost during development.

Furthermore, by exposing resists of different thicknesses from the backside of the TEM membrane AFM-IR could be used to build up a model of the 3-D interaction volume of the resist.

The presence of a plasmon resonance in the mid-IR region for the segmented antennas has to date not been confirmed. The fabrication of denser arrays of segmented antennas could facilitating the detection of the IR peak by improving the signal-to-noise ratio of the IR signal collected from the antennas. Simulated IR spectra using light polarised orthogonally to the long axis of the bowtie indicates the presence of an intense mode near 1750 cm^{-1}. As the laser used to collect the IR spectra was non-polarised, it is possible that the plasmonic modes parallel to the long axis of the bowtie were obscured by these intense orthogonal modes. Using an IR spectroscopy system that allows for the sample to be probed with polarised light could allow for the parallel modes to be isolated. Once the presence of the mid-IR resonance is confirmed the vibrational strong coupling of the segmented antenna to a carbon nanodot can be probed via Raman or IR spectroscopy. If a strongly coupled system is observed, these segmented antennas can be coupled to other molecular vibrations by tuning the LSPR wavelength by varying their dimensions.

The LSPR-induced growth of semiconductors demonstrated in this thesis is a versatile technique that could be adapted for the growth of other semiconductor materials. Using different plasmonic metals could expand the range of laser wavelengths that may e utilised for semiconductor nanomaterial growth. Furthermore, as the SLS growth mechanism is dependant on the eutectic point of the seed metal and semiconductor, using different plasmonic metals as seed particles could further expand the number of semiconductor materials that can be grown by this method. In addition to this, the use of a metal such as Al as a seed would further improve the suitability of this growth method for the development of on-chip devices where the migration of the Au seeds into the chip would be an issue.

As shown here, both SLS and hydrothermal synthesis mechanisms are possible by exploitation of LSPR. SLS growth requires the formation of an Au-Ge eutectic which has a temperature of 360 °C, whereas the hydrothermal synthesis of ZnO requires much lower temperatures around 90 °C.[294,309] A thorough understanding of the LSPR heating of

the Au nanoparticles and their surroundings under laser illumination is required to fully control this LSPR-induced growth, as well as the formation of bubbles. One method to improve the control of the Ge nanowire growth process would be the mixture of the DPG precursor with a high boiling point solvent such as squalene. The use of a high boiling point solvent should reduce the likelihood of bubbles forming when the Au nanoparticles are illuminated by the laser. In addition to this, diluting the DPG precursor will reduce the amount of elemental Ge available to migrate into the Au-Ge eutectic mixture, thereby reducing the rate of nanowire growth. Longer growth time-scales *i.e.,* on the order of minutes, will allow for greater control over and better uniformity of the length of the nanowires grown.

To obtain a better understanding of the nanowire growth mechanisms and conditions, in-situ heating in a TEM could be used. In this experiment a cell containing Au seed particles immersed in the relevant precursor material could be globally heated over a wide temperature range, and the nanowire growth could be observed in real-time using a TEM. This could allow for the precise determination of the temperatures at which bubbles are formed and nanowire growth are initiated. In addition to this, computational methods could be used to calculate the localised heating caused by the LSPR supported by the plasmonic Au nanoparticles illuminated at various laser powers. This would allow the laser power to be tuned so that the temperature of the nanoparticles matches with the temperatures required to initiate nanowire growth. Furthermore, by monitoring the growth of nanowires in-situ preferential growth directions could be identified. This could allow for further control over the structure and placement of semiconductor devices fabricated using this growth method. To date, photodetectors with a bandwidth greater than 100 GHz have been produced by fabricating amorphous Ge across the gap between two plasmonic resonators.[313] If the heating of the system is fully controlled, then the growth of amorphous Ge directly on the seed nanoparticles could be preferentially achieved. Consequently this method of LSPR-induced of Ge could be used to fabricate similar photodetectors on a sub-100-nm scale.

6.3 Final Remarks

Plasmonic materials offer great promise for applications such as catalysis, nano-optics, sensing, as well as in solar cells. To fully control and exploit the properties of plasmonic materials precise control of their dimensions and relative placement is required. In this thesis, we have investigated the limits of EBL and HIBL, and highlighted their utility and importance for the fabrication of the next generation of plasmonic devices. We have shown how FDTD simulations can be used to accurately predict the dimensions required for various geometries to support different LSPR modes. Furthermore, we have exploited the LSPR of these metal nanoparticles to probe the coupling between a plasmonic cavity and a vibrational mode in a chemical bond. In addition we have demonstrated how nanoscale semiconductor materials can be grown with excellent control of their on chip location via the exploitation of plasmonic heating. It is the belief of the author that continued research into advanced fabrication techniques, as well as into the mechanisms of the LSPR-driven chemical reaction could pave the way for the next generation of plasmonic devices.

Chapter 7

Bibliography

[1] Shi, X.; Prewett, P.; Huq, E.; Bagnall, D. M.; Robinson, A. P.; Boden, S. A. *Microelectronic Engineering* **2016**, *155*, 74–78.

[2] Khurgin, J. B. *Nanophotonics* **2019**,

[3] Linic, S.; Aslam, U.; Boerigter, C.; Morabito, M. *Nature Materials 2015 14:6* **2015**, *14*, 567–576.

[4] Cortés, E.; Xie, W.; Cambiasso, J.; Jermyn, A. S.; Sundararaman, R.; Narang, P.; Schlücker, S.; Maier, S. A. *Nature Communications* **2017**, *8*, 1–10.

[5] Zhang, Y.; He, S.; Guo, W.; Hu, Y.; Huang, J.; Mulcahy, J. R.; Wei, W. D. Surface-Plasmon-Driven Hot Electron Photochemistry. 2018; `https://pubs.acs.org/sharingguidelines`.

[6] Knight, M. W.; Sobhani, H.; Nordlander, P.; Halas, N. J. *Science* **2011**, *332*, 702–704.

[7] Tang, H.; Chen, C. J.; Huang, Z.; Bright, J.; Meng, G.; Liu, R. S.; Wu, N. *Journal of Chemical Physics* **2020**, *152*, 220901.

[8] Baffou, G.; Quidant, R. *Laser & Photonics Reviews* **2013**, *7*, 171–187.

[9] Jauffred, L.; Samadi, A.; Klingberg, H.; Bendix, P. M.; Oddershede, L. B. Plasmonic Heating of Nanostructures. 2019.

[10] Grzelczak, M.; Pérez-Juste, J.; Mulvaney, P.; Liz-Marzán, L. M. Shape control in gold nanoparticle synthesis. 2008.

[11] Tseng, W. H.; Chiu, C. Y.; Chou, S. W.; Chen, H. C.; Tsai, M. L.; Kuo, Y. C.; Lien, D. H.; Tsao, Y. C.; Huang, K. Y.; Yeh, C. T.; He, J. H.; Wu, C. I.; Huang, M. H.; Chou, P. T. *Journal of Physical Chemistry C* **2015**, *119*, 7554–7564.

[12] drinking-cup — British Museum. `https://www.britishmuseum.org/collection/object/H{\_}1958-1202-1`.

[13] West, P.; Ishii, S.; Naik, G.; Emani, N.; Shalaev, V.; Boltasseva, A. *Laser & Photonics Reviews* **2010**, *4*, 795–808.

[14] Kelly, K. L.; Coronado, E.; Zhao, L. L.; Schatz, G. C. *Journal of Physical Chemistry B* **2003**, *107*, 668–677.

[15] Hutter, E.; Fendler, J. H. *Advanced Materials* **2004**, *16*, 1685–1706.

[16] Campion, A.; Kambhampati, P. *Chemical Society Reviews* **1998**, *27*, 241–250.

[17] Dai, D.; Wu, H.; Zhang, W. *Materials 2015, Vol. 8, Pages 6772-6791* **2015**, *8*, 6772–6791.

[18] Homola, J. *Analytical and Bioanalytical Chemistry* **2003**, *377*, 528–539.

[19] Lee, J. S.; Han, M. S.; Mirkin, C. A. *Angewandte Chemie International Edition* **2007**, *46*, 4093–4096.

[20] Hou, W.; Liu, Z.; Pavaskar, P.; Hung, W. H.; Cronin, S. B. *Journal of Catalysis* **2011**, *277*, 149–153.

[21] Dong, J.; Zhang, Z.; Zheng, H.; Sun, M. Recent Progress on Plasmon-Enhanced Fluorescence. 2015; `https://www.degruyter.com/document/doi/10.1515/nanoph-2015-0028/html`.

[22] Novotny, L.; Hecht, B. *Principles of Nano-Optics* **2012**, 282–312.

[23] Novotny, L.; Van Hulst, N. *Nature Photonics* **2011**, *5*, 83–90.

[24] Jaynes, E. T.; Cummings, F. W. *Proceedings of the IEEE* **1963**, *51*, 89–109.

[25] Yoshle, T.; Scherer, A.; Hendrickson, J.; Khitrova, G.; Gibbs, H. M.; Rupper, G.; Ell, C.; Shchekin, O. B.; Deppe, D. G. *Nature* **2004**, *432*, 200–203.

[26] Thompson, R. J.; Rempe, G.; Kimble, H. J. *Observation of Normal-Mode Splitting for an Atom in an Optical Cavity*; 1992; Vol. 68.

[27] Vahala, K. J. Optical microcavities. 2003.

[28] Törmä, P.; Barnes, W. L. *Strong coupling between surface plasmon polaritons and emitters*; 2014.

[29] Purcell, E. *Phys. Rev* **1946**, *69*.

[30] Gérard, J. M.; Sermage, B.; Gayral, B.; Legrand, B.; Costard, E.; Thierry-Mieg, V. *Enhanced Spontaneous Emission by Quantum Boxes in a Monolithic Optical Microcavity*; 1998.

[31] Vasa, P.; Lienau, C. Strong Light-Matter Interaction in Quantum Emitter/Metal Hybrid Nanostructures. 2018.

[32] Halas, N. J.; Lal, S.; Chang, W. S.; Link, S.; Nordlander, P. Plasmons in strongly coupled metallic nanostructures. 2011; `https://pubs.acs.org/sharingguidelines`.

[33] Bitton, O.; Gupta, S. N.; Haran, G. *Nanophotonics* **2019**, *8*, 559–575.

[34] Höppener, C.; Lapin, Z. J.; Bharadwaj, P.; Novotny, L. *Physical Review Letters* **2012**, *109*, 017402.

[35] Brolo, A. G.; Kwok, S. C.; Cooper, M. D.; Moffitt, M. G.; Wang, C. W.; Gordon, R.; Riordon, J.; Kavanagh, K. L. *Journal of Physical Chemistry B* **2006**, *110*, 8307–8313.

[36] Achermann, M. *Journal of Physical Chemistry Letters* **2010**, *1*, 2837–2843.

[37] Curto, A. G.; Volpe, G.; Taminiau, T. H.; Kreuzer, M. P.; Quidant, R.; Van Hulst, N. F. *Science* **2010**, *329*, 930–933.

[38] Ratchford, D.; Shafiei, F.; Kim, S.; Gray, S. K.; Li, X. *Nano Letters* **2011**, *11*, 1049–1054.

[39] Vasa, P.; Pomraenke, R.; Cirmi, G.; De Re, E.; Wang, W.; Schwieger, S.; Leipold, D.; Runge, E.; Cerullo, G.; Lienau, C. *ACS Nano* **2010**, *4*, 7559–7565.

[40] Hutchison, J. A.; Schwartz, T.; Genet, C.; Devaux, E.; Ebbesen, T. W. *Angewandte Chemie International Edition* **2012**, *51*, 1592–1596.

[41] Schwartz, T.; Hutchison, J. A.; Genet, C.; Ebbesen, T. W. **2011**,

[42] Thomas, A.; Lethuillier-Karl, L.; Nagarajan, K.; Vergauwe, R. M.; George, J.; Chervy, T.; Shalabney, A.; Devaux, E.; Genet, C.; Moran, J.; Ebbesen, T. W. *Science* **2019**, *363*, 615–619.

[43] Peter, E.; Senellart, P.; Martrou, D.; Lemaître, A.; Hours, J.; Gérard, J. M.; Bloch, J. *Physical Review Letters* **2005**, *95*, 067401.

[44] Gómez, D. E.; Vernon, K. C.; Mulvaney, P.; Davis, T. J. *Nano Letters* **2010**, *10*, 274–278.

[45] Wang, H.; Wang, H. Y.; Toma, A.; Yano, T. A.; Chen, Q. D.; Xu, H. L.; Sun, H. B.; Proietti Zaccaria, R. *Journal of Physical Chemistry Letters* **2016**, *7*, 4648–4654.

[46] Santhosh, K.; Bitton, O.; Chuntonov, L.; Haran, G. *Nature Communications 2016 7:1* **2016**, *7*, 1–5.

[47] Kumar, S.; Bozhevolnyi, S. I. *Advanced Quantum Technologies* **2021**, *4*, 2100057.

[48] Kuttruff, J.; Romanelli, M.; Pedrueza-Villalmanzo, E.; Allerbeck, J.; Fregoni, J.; Saavedra-Becerril, V.; Andréasson, J.; Brida, D.; Dmitriev, A.; Corni, S.; Maccaferri, N. *Nature Communications 2023 14:1* **2023**, *14*, 1–10.

[49] Chang, D. E.; Sørensen, A. S.; Demler, E. A.; Lukin, M. D. *Nature Physics 2007 3:11* **2007**, *3*, 807–812.

[50] Sato, Y.; Tanaka, Y.; Upham, J.; Takahashi, Y.; Asano, T.; Noda, S. *Nature Photonics 2011 6:1* **2011**, *6*, 56–61.

[51] Noda, S. *Science* **2006**, *314*, 260–261.

[52] Cao, E.; Lin, W.; Sun, M.; Liang, W.; Song, Y. Exciton-plasmon coupling interactions: From principle to applications. 2018.

[53] Pelton, M.; Yamamoto, Y. **1999**,

[54] Manuel, A. P.; Kirkey, A.; Mahdi, N.; Shankar, K. *Journal of Materials Chemistry C* **2019**, *7*, 1821–1853.

[55] Khurgin, J. B. *Nature Nanotechnology* **2015**, *10*, 2–6.

[56] Boriskina, S. V.; Cooper, T. A.; Zeng, L.; Ni, G.; Tong, J. K.; Tsurimaki, Y.; Huang, Y.; Meroueh, L.; Mahan, G.; Chen, G. *Advances in Optics and Photonics* **2017**, *9*, 775.

[57] Govorov, A. O.; Zhang, H.; Gun'Ko, Y. K. *Journal of Physical Chemistry C* **2013**, *117*, 16616–16631.

[58] Kumar, P. V.; Rossi, T. P.; Kuisma, M.; Erhart, P.; Norris, D. J. Direct hot-carrier transfer in plasmonic catalysis. Faraday Discussions. 2019; pp 189–197.

[59] Furube, A.; Du, L.; Hara, K.; Katoh, R.; Tachiya, M. *Journal of the American Chemical Society* **2007**, *129*, 14852–14853.

[60] Zhu, X.-Y. *Annual Review of Physical Chemistry* **2002**, *53*, 221–247.

[61] Scales, C.; Berini, P. *IEEE Journal of Quantum Electronics* **2010**, *46*, 633–643.

[62] Xie, W.; Schlücker, S. *Nature Communications* **2015**, *6*, 1–6.

[63] Christopher, P.; Moskovits, M. *Annual Review of Physical Chemistry* **2017**, *68*, 379–398.

[64] Lee, H.; Park, Y.; Song, K.; Park, J. Y. *Accounts of Chemical Research* **2022**, *55*, 3727–3737.

[65] Brongersma, M. L.; Halas, N. J.; Nordlander, P. *Nature Nanotechnology 2015 10:1* **2015**, *10*, 25–34.

[66] Baffou, G.; Polleux, J.; Rigneault, H.; Monneret, S. *Journal of Physical Chemistry C* **2014**, *118*, 4890–4898.

[67] Pitsillides, C. M.; Joe, E. K.; Wei, X.; Anderson, R. R.; Lin, C. P. *Biophysical Journal* **2003**, *84*, 4023–4032.

[68] Shukla, R.; Bansal, V.; Chaudhary, M.; Basu, A.; Bhonde, R. R.; Sastry, M. Biocompatibility of gold nanoparticles and their endocytotic fate inside the cellular compartment: A microscopic overview. 2005.

[69] Cao, L.; Barsic, D. N.; Guichard, A. R.; Brongersma, M. L. *Nano Letters* **2007**, *7*, 3523–3527.

[70] Catone, D.; Ciavardini, A.; Di Mario, L.; Paladini, A.; Toschi, F.; Cartoni, A.; Fratoddi, I.; Venditti, I.; Alabastri, A.; Proietti Zaccaria, R.; O'Keeffe, P. *Journal of Physical Chemistry Letters* **2018**, *9*, 5002–5008.

[71] Garnett, E. C.; Cai, W.; Cha, J. J.; Mahmood, F.; Connor, S. T.; Greyson Christoforo, M.; Cui, Y.; McGehee, M. D.; Brongersma, M. L. *Nature Materials* **2012**, *11*, 241–249.

[72] Johnson, P. B.; Christy, R. W. *Physical Review B* **1972**, *6*, 4370.

[73] McPeak, K. M.; Jayanti, S. V.; Kress, S. J.; Meyer, S.; Iotti, S.; Rossinelli, A.; Norris, D. J. *ACS Photonics* **2015**, *2*, 326–333.

[74] Smith, N. V. *Physical Review* **1969**, *183*, 634.

[75] Palm, K. J.; Murray, J. B.; Narayan, T. C.; Munday, J. N. *ACS Photonics* **2018**, *5*, 4677–4686.

[76] Bennett, H. E.; Peck, R. L.; Burge, D. K.; Bennett, J. M. *Journal of Applied Physics* **1969**, *40*, 3351–3360.

[77] Chumpol, K.; McEvoy, N.; Zhang, X.; Hobbs, R. G. *Journal of Physical Chemistry C* **2020**, *124*, 8930–8937.

[78] Blaber, M. G.; Arnold, M. D.; Harris, N.; Ford, M. J.; Cortie, M. B. *Physica B: Condensed Matter* **2007**, *394*, 184–187.

[79] Ringe, E. *Journal of Physical Chemistry C* **2020**, *124*, 15665–15679.

[80] Naik, G. V.; Kim, J.; Boltasseva, A. *Opt Mater Express* **2011**, *1*, 1090–1099.

[81] Naik, G. V.; Boltasseva, A.; Kildishev, A. V.; Schroeder, J. L.; Ni, X.; Sands, T. D. *Optical Materials Express, Vol. 2, Issue 4, pp. 478-489* **2012**, *2*, 478–489.

[82] Babicheva, V. E.; Boltasseva, A.; Lavrinenko, A. V. *Nanophotonics* **2015**, *4*, 165–185.

[83] Khamh, H.; Sachet, E.; Kelly, K.; Maria, J. P.; Franzen, S. *Journal of Materials Chemistry C* **2018**, *6*, 8326–8342.

[84] Tegg, L.; Keast, V. J. *Plasmonics 2022 18:1* **2022**, *18*, 49–71.

[85] Lalisse, A.; Tessier, G.; Plain, J.; Baffou, G. *Scientific Reports 2016 6:1* **2016**, *6*, 1–10.

[86] Briggs, J. A.; Naik, G. V.; Petach, T. A.; Baum, B. K.; Goldhaber-Gordon, D.; Dionne, J. A. *Applied Physics Letters* **2016**, *108*, 51110.

[87] Saha, S.; Dutta, A.; Kinsey, N.; Kildishev, A. V.; Shalaev, V. M.; Boltasseva, A. *ACS Photonics* **2018**, *5*, 4423–4431.

[88] Khezripour, Z.; Mahani, F. F.; Mokhtari, A. *Optical Materials* **2018**, *84*, 651–657.

[89] Hao, Q. et al. *Advanced Materials* **2018**, *30*, 1705421.

[90] Wang, L.; Hasanzadeh Kafshgari, M.; Meunier, M. *Advanced Functional Materials* **2020**, *30*, 2005400.

[91] Zeman, E. J.; Schatz, G. C. *Journal of Physical Chemistry* **1987**, *91*, 634–643.

[92] Voshchinnikov, N. V.; Farafonov, V. G. *Astrophysics and Space Science* **1993**, *204*, 19–86.

[93] Draine, B. T.; Flatau, P. J. *JOSA A, Vol. 11, Issue 4, pp. 1491-1499* **1994**, *11*, 1491–1499.

[94] Aizpurua, J.; Bryant, G. W.; Richter, L. J.; García De Abajo, F. J.; Kelley, B. K.; Mallouk, T. *Physical Review B - Condensed Matter and Materials Physics* **2005**, *71*, 235420.

[95] Wiley, B. J.; Im, S. H.; Li, Z. Y.; McLellan, J.; Siekkinen, A.; Xia, Y. *Journal of Physical Chemistry B* **2006**, *110*, 15666–15675.

[96] Kottmann, J.; Martin, O. J.; Smith, D. R.; Schultz, S. *Physical Review B* **2001**, *64*, 235402.

[97] Urbieta, M.; Barbry, M.; Zhang, Y.; Koval, P.; Sánchez-Portal, D.; Zabala, N.; Aizpurua, J. *ACS Nano* **2018**, *12*, 585–595.

[98] Fukuoka, N.; Tanabe, K. *Nanomaterials* **2019**, *9*.

[99] Mock, J. J.; Barbic, M.; Smith, D. R.; Schultz, D. A.; Schultz, S. *J. Chem. Phys* **2002**, *116*, 6755.

[100] Harra, J.; Mäkitalo, J.; Siikanen, R.; Virkki, M.; Genty, G.; Kobayashi, T.; Kauranen, M.; Mäkelä, J. M. *Journal of Nanoparticle Research* **2012**, *14*.

[101] Britannica, The Editors of Encyclopaedia. "lithography". Encyclopedia Britannica, 6 Oct. 2023, Accessed 28 November 2023. 1911; `https://www.britannica.com/technology/lithography`.

[102] Lithography — Tate. `https://www.tate.org.uk/art/art-terms/l/lithography`.

[103] The First Photograph - Heliography. https://web.archive.org/web/20090908012105/http://www.hrc.utexas.edu/exhibitions/permanent/wfp/heliography.html.

[104] Nall, J. R.; Lathrop, J. W. *IRE Transactions on Electron Devices* **1958**, *5*, 117.

[105] Lathrop, J. W. *IEEE Annals of the History of Computing* **2013**, *35*, 48–55.

[106] Ronse, K. *Comptes Rendus Physique* **2006**, *7*, 844–857.

[107] van den Brink, M. A.; Jasper, H.; Slonaker, S. D.; Wijnhoven, P.; Klaassen, F. *Proceedings Volume 2726, Optical Microlithography IX; https://doi.org/10.1117/12.240936* **1996**, *2726*, 734–753.

[108] Moore, G. E. *Proceedings of the IEEE* **1998**, *86*, 82–85.

[109] Moore, G. E. *IEEE Solid-State Circuits Society Newsletter* **2009**, *11*, 36–37.

[110] Roser, M.; Ritchie, H.; Mathieu, E. *Our World in Data* **2023**,

[111] Abbe, E. *Archiv für mikroskopische Anatomie* **1873**, *9*, 413–418.

[112] Wilson, M.; DeRose, J.; Greb, C. Microscope Resolution: Concepts, Factors and Calculation — Science Lab — Leica Microsystems. https://www.leica-microsystems.com/science-lab/life-science/microscope-resolution-concepts-factors-and-calculation/.

[113] F.R.S., L. R. *The London, Edinburgh, and Dublin Philosophical Magazine and Journal of Science* **1879**, *8*, 261–274.

[114] The Rayleigh criterion for resolution — ASML. https://www.asml.com/en/technology/lithography-principles/rayleigh-criterion.

[115] Lin, B. J. *C. R. Physique* **2006**, *7*, 858–874.

[116] Jain, K.; Lin, B. J. *IEEE Electron Device Letters* **1982**, *3*, 53–55.

[117] Jain, K. *Excimer laser lithography*; SPIE Optical Engineering Press, 1990; p 212.

[118] Ronse, K.; Jansen, P.; Gronheid, R.; Hendrickx, E.; Maenhoudt, M.; Goethals, M.; Vandenberghe, G. *Proceedings of the Custom Integrated Circuits Conference* **2008**, 371–378.

[119] Ober, C. K.; Käfer, F.; Yuan, C. *Polymer* **2023**, *280*, 126020.

[120] Wu, B.; Kumar, A. *Journal of Vacuum Science & Technology B: Microelectronics and Nanometer Structures Processing, Measurement, and Phenomena* **2007**, *25*, 1743–1761.

[121] Gronheid, R.; Younkin, T. R.; Leeson, M. J.; Fonseca, C.; Hooge, J. S.; Nafus, K.; Biafore, J. J.; Smith, M. D. *Proc. SPIE 7969, Extreme Ultraviolet (EUV) Lithography II, 796904* **2011**, 40–50.

[122] Garcia, R.; Knoll, A. W.; Riedo, E. *Nature Nanotechnology 2014 9:8* **2014**, *9*, 577–587.

[123] Eigler, D. M.; Schweizer, E. K. *Nature 1990 344:6266* **1990**, *344*, 524–526.

[124] Xu, K.; Chen, J. *Applied Nanoscience (Switzerland)* **2020**, *10*, 1013–1022.

[125] Ginger, D. S.; Zhang, H.; Mirkin, C. A. *Angewandte Chemie International Edition* **2004**, *43*, 30–45.

[126] Brünger, W.; Kley, E. B.; Schnabel, B.; Stolberg, I.; Zierbock, M.; Plontke, R. *Microelectronic Engineering* **1995**, *27*, 135–138.

[127] Bartolo, P. J.; Mitchell, G. *Rapid Prototyping Journal* **2003**, *9*, 150–156.

[128] Ruska, E. *Bioscience Reports* **1987**, *7*, 607–629.

[129] von Ardenne, M. *Z. Phys.* **1938**, *109*, 553–572.

[130] Feynman, R. P. *Journal of Microelectromechanical Systems* **1992**, *1*, 60–66.

[131] Christy, R. W. *Journal of Applied Physics* **1960**, *31*, 1680–1683.

[132] Haller, I.; White, P. *Journal of Physical Chemistry* **1963**, *67*, 1784–1788.

[133] Larkin, M. W.; Matta, R. K. *Solid State Electronics* **1967**, *10*.

[134] Pasiecznik, J.; Reeds, J. W. *Journal of Vacuum Science and Technology* **1978**, *15*, 909–912.

[135] Carr, D. W.; Tiberio, R. C. *Materials Research Society Symposium - Proceedings* **2000**, *584*, 33–43.

[136] Manfrinato, V. R.; Stein, A.; Zhang, L.; Nam, C. Y.; Yager, K. G.; Stach, E. A.; Black, C. T. *Nano Letters* **2017**, *17*, 4562–4567.

[137] Lee, B.; Hong, J.; Amos, N.; Dumer, I.; Litvinov, D.; Khizroev, S. *Journal of Nanoparticle Research* **2013**, *15*, 1–8.

[138] Zhou, W.; Apkarian, R.; Wang, Z. L.; Joy, D. *Scanning Microscopy for Nanotechnology: Techniques and Applications* **2007**, 1–40.

[139] Electron Microscopy- Electron Source - Advancing Materials. `https://www.thermofisher.com/blog/materials/electron-source-fundamentals/`.

[140] Goldstein, J. I.; Newbury, D. E.; Echlin, P.; Joy, D. C.; Lyman, C. E.; Lifshin, E.; Sawyer, L.; Michael, J. R. **2003**,

[141] Gesley, M. *Journal of Applied Physics* **1989**, *65*, 914–926.

[142] Everhart, T. E.; Thornley, R. F. M. *Journal of Scientific Instruments* **1960**, *37*, 246.

[143] Lloyd, G. E. *Mineralogical Magazine* **1987**, *51*, 3–19.

[144] Raman, S. N.; Paul, D. F.; Hammond, J. S.; Bomben, K. D. *Microscopy Today* **2011**, *19*, 12–15.

[145] Zadora, G.; Brozek-Mucha, Z. *Materials Chemistry and Physics* **2003**, *81*, 345–348.

[146] Müller, E. W.; Tsong, T. T. *New York: Elsevier* **1969**,

[147] Hill, R.; Notte, J.; Ward, B. *Physics Procedia* **2008**, *1*, 135–141.

[148] Ward, B. W.; Notte, J. A.; Economou, N. P. *Journal of Vacuum Science & Technology B: Microelectronics and Nanometer Structures* **2006**, *24*, 2871.

[149] Notte, J.; Ward, B.; Economou, N.; Hill, R.; Percival, R.; Farkas, L.; McVey, S. An introduction to the helium ion microscope. AIP Conference Proceedings. 2007; pp 489–496.

[150] Hlawacek, G.; Veligura, V.; van Gastel, R.; Poelsema, B. *Journal of Vacuum Science & Technology B, Nanotechnology and Microelectronics: Materials, Processing, Measurement, and Phenomena* **2014**, *32*, 020801.

[151] Fitzek, H.; Schroettner, H.; Wagner, J.; Hofer, F.; Rattenberger, J. *Journal of Microscopy* **2015**, *260*, 133–139.

[152] Boden, S. A. *NanoScience and Technology* **2016**, 149–172.

[153] Boden, S. A.; Asadollahbaik, A.; Rutt, H. N.; Bagnall, D. M. *Scanning* **2012**, *34*, 107–120.

[154] spherical aberration — Glossary — JEOL Ltd. `https://www.jeol.com/words/semterms/20121024.024959.php{\#}gsc.tab=0`.

[155] Joy, D. C. *Biological Low-Voltage Scanning Electron Microscopy* **2008**, 107–127.

[156] Leary, R.; Brydson, R. *Advances in Imaging and Electron Physics* **2011**, *165*, 73–130.

[157] chromatic aberration — Glossary — JEOL Ltd. `https://www.jeol.com/words/semterms/20121024.011200.php{\#}gsc.tab=0`.

[158] Ernst, N.; Bozdech, G.; Schmidt, H.; Schmidt, W. A.; Larkins, G. L. *Applied Surface Science* **1993**, *67*, 111–117.

[159] Manfrinato, V. R.; Zhang, L.; Su, D.; Duan, H.; Hobbs, R. G.; Stach, E. A.; Berggren, K. K. *Nano Letters* **2013**, *13*, 1555–1558.

[160] Ren, L.; Chen, B. *International Conference on Solid-State and Integrated Circuits Technology Proceedings, ICSICT* **2004**, *1*, 579–582.

[161] Bernstein, G. H.; Carter, A. D.; Joy, D. C. *Scanning* **2013**, *35*, 1–6.

[162] Pantenburg, F. J.; Achenbach, . S.; Mohr, . J.; Achenbach, . S.; Mohr, J. *Journal of Vacuum Science & Technology B: Microelectronics and Nanometer Structures Processing, Measurement, and Phenomena* **1998**, *16*, 3547–3551.

[163] Hu, W. W.; Sarveswaran, K.; Lieberman, M.; Bernstein, G. H. *Journal of Vacuum Science & Technology B: Microelectronics and Nanometer Structures Processing, Measurement, and Phenomena* **2004**, *22*, 1711–1716.

[164] Cord, B.; Lutkenhaus, J.; Berggren, K. K. *Journal of Vacuum Science & Technology B: Microelectronics and Nanometer Structures Processing, Measurement, and Phenomena* **2007**, *25*, 2013–2016.

[165] Rahman, F.; Carbaugh, D. J.; Wright, J. T.; Rajan, P.; Pandya, S. G.; Kaya, S. *Microelectronic Engineering* **2020**, *224*, 111238.

[166] Owen, G. *Reports on Progress in Physics* **1985**, *48*, 795.

[167] F Hoole, A. C.; Welland, M. E.; Broers, A. N. *Semiconductor Science and Technology* **1997**, *12*, 1166.

[168] Duan, H.; Winston, D.; Yang, J. K. W.; Cord, B. M.; Manfrinato, V. R.; Berggren, K. K. *Journal of Vacuum Science & Technology B* **2010**, *28*, C6C58–C6C62.

[169] Yang, J. K. W.; Berggren, K. K. *Journal of Vacuum Science & Technology B: Microelectronics and Nanometer Structures Processing, Measurement, and Phenomena* **2007**, *25*, 2025–2029.

[170] Yang, J. K. W.; Cord, B.; Duan, H.; Berggren, K. K.; Klingfus, J.; Nam, S.-W.; Kim, K.-B.; Michael, .; Rooks, J.; Rooks, M. J. *Journal of Vacuum Science & Technology B: Microelectronics and Nanometer Structures Processing, Measurement, and Phenomena* **2009**, *27*, 2622–2627.

[171] Winston, D.; Cord, B. M.; Ming, B.; Bell, D. C.; DiNatale, W. F.; Stern, L. A.; Vladar, A. E.; Postek, M. T.; Mondol, M. K.; Yang, J. K. W.; Berggren, K. K. *Journal of Vacuum Science & Technology B: Microelectronics and Nanometer Structures* **2009**, *27*, 2702.

[172] Namatsu, H.; Yamaguchi, T.; Nagase, M.; Yamazaki, K.; Kurihara, K. *Microelectronic Engineering* **1998**, *41-42*, 331–334.

[173] Grigorescu, A. E.; Hagen, C. W. *Nanotechnology* **2009**, *20*, 292001.

[174] Van Delft, F. C. *Journal of Vacuum Science & Technology B: Microelectronics and Nanometer Structures Processing, Measurement, and Phenomena* **2002**, *20*, 2932–2936.

[175] Gangnaik, A. S.; Georgiev, Y. M.; Holmes, J. D. *Chemistry of Materials* **2017**, *29*, 1898–1917.

[176] Kuznetsova, N. A.; Malkov, G. V.; Gribov, B. G. *Russian Chemical Reviews* **2020**, *89*, 173–190.

[177] Lawson, R. A.; Lee, C. T.; Yueh, W.; Tolbert, L.; Henderson, C. L. *Microelectronic Engineering* **2008**, *85*, 959–962.

[178] Yoo, J. B.; Park, S. W.; Kang, H. N.; Mondkar, H. S.; Sohn, K.; Kim, H. M.; Kim, K. B.; Lee, H. *Polymer* **2014**, *55*, 3599–3604.

[179] Gibbons, F.; Zaid, H. M.; Manickam, M.; Preece, J. A.; Palmer, R. E.; Robinson, A. P. *Small* **2007**, *3*, 2076–2080.

[180] Yang, D. X.; Frommhold, A.; Xue, X.; Palmer, R. E.; Robinson, A. P. *Journal of Materials Chemistry C* **2014**, *2*, 1505–1512.

[181] Okamura, H.; Forman, D. C.; Ober, C. K. *Polymer Bulletin* **2014**, *71*, 2395–2405.

[182] Yang, D. et al. *Journal of Physical Chemistry Letters* **2022**, *13*, 1578–1586.

[183] Manyam, J.; Manickam, M.; Preece, J. A.; Palmer, R. E.; Robinson, A. P. G. *https://doi.org/10.1117/12.879469* **2011**, *7972*, 727–738.

[184] Parsons, J.; Burrows, C. P.; Sambles, J. R.; Barnes, W. L. *Journal of Modern Optics* **2010**, *57*, 356–365.

[185] Yee, K. S. *IEEE Transactions on Antennas and Propagation* **1966**, *14*, 302–307.

[186] Hagness, S. C.; Taflove, A.; Gedney, S. D. *Handbook of Numerical Analysis* **2005**, *13*, 199–315.

[187] Palik, E. D. *Handbook of optical constants of solids*, 3rd ed.; Academic Press, 1998.

[188] Philipp, H. R. *Journal of The Electrochemical Society* **1973**, *120*, 295.

[189] Kischkat, J.; Peters, S.; Gruska, B.; Semtsiv, M.; Chashnikova, M.; Klinkmüller, M.; Fedosenko, O.; MacHulik, S.; Aleksandrova, A.; Monastyrskyi, G.; Flores, Y.; Masselink, W. T. *Applied Optics* **2012**, *51*, 6789–6798.

[190] König, T. A.; Ledin, P. A.; Kerszulis, J.; Mahmoud, M. A.; El-Sayed, M. A.; Reynolds, J. R.; Tsukruk, V. V. *ACS Nano* **2014**, *8*, 6182–6192.

[191] Tamada, M.; Koshikawa, H.; Hosoi, F.; Suwa, T. *Thin Solid Films* **1998**, *315*, 40–43.

[192] Berenger, J. P. *Journal of Computational Physics* **1994**, *114*, 185–200.

[193] Ţucureanu, V.; Matei, A.; Avram, A. M. *Critical Reviews in Analytical Chemistry* **2016**, *46*, 502–520.

[194] Difference IR vs FTIR — Bruker. `https://www.bruker.com/en/products-and-solutions/infrared-and-raman/ft-ir-routine-spectrometer/what-is-ft-ir-spectroscopy/difference-ir-vs-ftir.html`.

[195] Raman, C. V. *Proceedings of the Indian Academy of Sciences - Section A* **1953**, *37*, 333–341.

[196] Winston, D.; Ferrera, J.; Battistella, L.; Vladár, A. E.; Berggren, K. K. *Scanning* **2012**, *34*, 121–128.

[197] Ramachandra, R.; Griffin, B.; Joy, D. *Ultramicroscopy* **2009**, *109*, 748–757.

[198] Vraneš, M.; Borišev, I.; Tot, A.; Armaković, S.; Armaković, S.; Jović, D.; Gadžurić, S.; Djordjevic, A. *Physical Chemistry Chemical Physics* **2016**, *19*, 135–144.

[199] Flatabo, R.; Agarwal, A.; Hobbs, R.; Greve, M. M.; Holst, B.; Berggren, K. K. *Nanotechnology* **2018**, *29*, 275301.

[200] Guo, H.; Itoh, H.; Wang, C.; Zhang, H.; Fujita, D. *Applied Physics Letters* **2014**, *105*, 023105.

[201] Hill, R.; Notte, J. A.; Scipioni, L. *Advances in Imaging and Electron Physics*; Academic Press Inc., 2012; Vol. 170; pp 65–148.

[202] Fallica, R.; Kirchner, R.; Ekinci, Y.; Mailly, D. *Journal of Vacuum Science & Technology B, Nanotechnology and Microelectronics: Materials, Processing, Measurement, and Phenomena* **2016**, *34*, 06K702.

[203] Cohen-Tanugi, D.; Yao, N. *Journal of Applied Physics* **2008**, *104*, 063504.

[204] Ohya, K.; Inai, K.; Nisawa, A.; Itoh, A. *Nuclear Instruments and Methods in Physics Research Section B: Beam Interactions with Materials and Atoms* **2008**, *266*, 541–548.

[205] Manfrinato, V. R.; Wen, J.; Zhang, L.; Yang, Y.; Hobbs, R. G.; Baker, B.; Su, D.; Zakharov, D.; Zaluzec, N. J.; Miller, D. J.; Stach, E. A.; Berggren, K. K. *Nano Letters* **2014**, *14*, 4406–4412.

[206] Baragiola, R. A.; Ritzau, S. M.; Monreal, R. C.; Dukes, C. A.; Riccardi, P. *Nuclear Instruments and Methods in Physics Research Section B: Beam Interactions with Materials and Atoms* **1999**, *157*, 110–115.

[207] Lee, C.-L.; Chien, S.-W.; Tsai, K.-Y. *Novel Patterning Technologies* **2018**, *10584*, 269–280.

[208] Lee, C. L.; Chien, S. W.; Tsai, K. Y.; Liu, C. H. *Journal of Micro/Nanopatterning, Materials, and Metrology* **2021**, *20*, 033201.

[209] Brand, C.; Sclafani, M.; Knobloch, C.; Lilach, Y.; Juffmann, T.; Kotakoski, J.; Mangler, C.; Winter, A.; Turchanin, A.; Meyer, J.; Cheshnovsky, O.; Arndt, M. *Nature Nanotechnology* **2015**, *10*, 845–848.

[210] Nesse, T.; Simonsen, I.; Holst, B. *Physical Review Applied* **2019**, *11*, 024009.

[211] Ditlbacher, . H. et al. *Optics Express, Vol. 22, Issue 11, pp. 13234-13243* **2014**, *22*, 13234–13243.

[212] Shi, W.; Friedman, A. K.; Baker, L. A. *Analytical Chemistry* **2017**, *89*, 157–188.

[213] Palau, A. S.; Eder, S. D.; Bracco, G.; Holst, B. *arXiv preprint arXiv:2111.12582* **2021**,

[214] Cronin, A. D.; Schmiedmayer, J.; Pritchard, D. E. *Reviews of Modern Physics* **2009**, *81*, 1051–1129.

[215] Li, Z.; Jin, J.; Yang, F.; Song, N.; Yin, Y. *Nature Communications 2020 11:1* **2020**, *11*, 1–11.

[216] Chen, J.; Ye, Z.; Yang, F.; Yin, Y. *Small Science* **2021**, *1*, 2000055.

[217] Korgel, B. A.; Lee, D. C.; Hanrath, T.; Yacaman, M. J.; Thesen, A.; Matijevic, M.; Kilaas, R.; Kisielowski, C.; Diebold, A. C. *IEEE Transactions on Semiconductor Manufacturing* **2006**, *19*, 391–395.

[218] Lehnert, T.; Ghorbani-Asl, M.; Köster, J.; Lee, Z.; Krasheninnikov, A. V.; Kaiser, U. *ACS Applied Nano Materials* **2019**, *2*, 3262–3270.

[219] Tsybeskov, L.; Grom, G. F.; Jungo, M.; Montes, L.; Fauchet, P. M.; McCaffrey, J. P.; Baribeau, J. M.; Sproule, G. I.; Lockwood, D. J. *Materials Science and Engineering: B* **2000**, *69-70*, 303–308.

[220] Liu, S.; Zhao, Q.; Xu, J.; Yan, K.; Peng, H.; Yang, F.; You, L.; Yu, D. *Nanotechnology* **2012**, *23*, 085301.

[221] Su, D. *Green Energy & Environment* **2017**, *2*, 70–83.

[222] Cai, J.; Zhu, Z.; A Alkemade, P. F.; van Veldhoven, E.; Wang, Q.; Ge, H.; Rodrigues, S. P.; Cai, W.; Li, W.-D. *Advanced Materials Interfaces* **2018**, *5*, 1800203.

[223] Deng, Y.; Zhuang, X.; Wang, W.; Gu, R.; He, D.; Wang, L.; Cheng, X. *Nanotechnology* **2021**, *32*, 415302.

[224] Livengood, R.; Tan, S.; Greenzweig, Y.; Notte, J.; McVey, S. *Journal of Vacuum Science & Technology B: Microelectronics and Nanometer Structures* **2009**, *27*, 3244.

[225] Shi, X.; Prewett, P.; Huq, E.; Bagnall, D. M.; Boden, S. A. **2016**,

[226] Van Der Drift, E.; Maas, D. J. *Nanofabrication: Techniques and Principles*; Springer-Verlag Wien, 2012; Vol. 9783709104; pp 93–116.

[227] Chen, X.; Palmer, R. E.; Robinson, A. P. *Nanotechnology* **2008**, *19*, 275308.

[228] Rao, A. M.; Zhou, P.; Wang, K. A.; Hager, G. T.; Holden, J. M.; Wang, Y.; Lee, W. T.; Bi, X. X.; Eklund, P. C.; Cornett, D. S.; Duncan, M. A.; Amster, I. J. *Science* **1993**, *259*, 955–957.

[229] Tada, T.; Kanayama, T. *Journal of Photopolymer Science and Technology* **1997**, *10*, 647–650.

[230] Ziegler, J. F.; Ziegler, M. D.; Biersack, J. P. *Nuclear Instruments and Methods in Physics Research, Section B: Beam Interactions with Materials and Atoms* **2010**, *268*, 1818–1823.

[231] Joy, D. C. *Monte Carlo modeling for electron microscopy and microanalysis*; Oxford University Press, 1995; p 216.

[232] Ghanbari, R. A. Physics and Fabrication of Quasi-One-Dimensional Conductors. Ph.D. thesis, 1993.

[233] Rai-Choudhury, P. *Handbook of Microlithography, Micromachining, and Microfabrication. Volume 1: Microlithography*; SPIE PRESS, 1997.

[234] Wu, B.; Neureuther, A. R. *Citation: Journal of Vacuum Science & Technology B: Microelectronics and Nanometer Structures Processing* **2001**, *19*, 2508.

[235] Li, W.-D.; Wu, W.; Stanley Williams, R. *Journal of Vacuum Science & Technology B* **2012**, *30*, 06F304.

[236] Marcott, C.; Lo, M.; Kjoller, K.; Prater, C.; Gerrard, D. P. *Microscopy Today* **2012**, *20*, 16–21.

[237] Walia, J.; Rashid, S.; Variola, F.; Berini, P. *Advanced Engineering Materials* **2023**, *25*, 2201707.

[238] Garcia-Vidal, F. J.; Ciuti, C.; Ebbesen, T. W. *Science* **2021**, *373*.

[239] Nagarajan, K.; Thomas, A.; Ebbesen, T. W. *Journal of the American Chemical Society* **2021**, *143*, 16877–16889.

[240] Lee, Y. M.; Kim, S. E.; Park, J. E. *Nano Convergence 2023 10:1* **2023**, *10*, 1–28.

[241] Akimov, A. V.; Mukherjee, A.; Yu, C. L.; Chang, D. E.; Zibrov, A. S.; Hemmer, P. R.; Park, H.; Lukin, M. D. *Nature* **2007**, *450*, 402–406.

[242] Koenderink, A. F. Single-Photon Nanoantennas. 2017.

[243] Dzsotjan, D.; Sorensen, A. S.; Fleischhauer, M. *Physical Review B - Condensed Matter and Materials Physics* **2010**, *82*.

[244] Huck, A.; Andersen, U. L. *Nanophotonics* **2016**, *5*, 483–495.

[245] Thomas, A.; George, J.; Shalabney, A.; Dryzhakov, M.; Varma, S. J.; Moran, J.; Chervy, T.; Zhong, X.; Devaux, E.; Genet, C.; Hutchison, J. A.; Ebbesen, T. W. *Angewandte Chemie International Edition* **2016**, *55*, 11462–11466.

[246] Pang, Y.; Thomas, A.; Nagarajan, K.; Vergauwe, R. M.; Joseph, K.; Patrahau, B.; Wang, K.; Genet, C.; Ebbesen, T. W. *Angewandte Chemie - International Edition* **2020**, *59*, 10436–10440.

[247] Sau, A.; Nagarajan, K.; Patrahau, B.; Lethuillier-Karl, L.; Vergauwe, R. M.; Thomas, A.; Moran, J.; Genet, C.; Ebbesen, T. W. *Angewandte Chemie - International Edition* **2021**, *60*, 5712–5717.

[248] Memmi, H.; Benson, O.; Sadofev, S.; Kalusniak, S. *Physical Review Letters* **2017**, *118*, 126802.

[249] Dayal, G.; Morichika, I.; Ashihara, S. *Journal of Physical Chemistry Letters* **2021**, *12*, 3171–3175.

[250] Verdelli, F.; Schulpen, J. J.; Baldi, A.; Rivas, J. G. *Journal of Physical Chemistry C* **2022**, *126*, 7143–7151.

[251] Qian, X. M.; Nie, S. M. *Chemical Society Reviews* **2008**, *37*, 912–920.

[252] Tabatabaei, M.; Najiminaini, M.; Davieau, K.; Kaminska, B.; Singh, M. R.; Carson, J. J. L.; Lagugné-Labarthet, F. *ACS Photonics* **2015**, *2*, 752–759.

[253] Oldenburg, R. S. J. D. et al. *Optics Express,* **2008**, *16*, 9144–9154.

[254] Wallace, G. Q.; Lagugné-Labarthet, F. *Analyst* **2018**, *144*, 13–30.

[255] Wen, Y.; Liu, S.; Zhang, H.; Wang, L. *Plasmonics* **2018**, *13*, 1767–1773.

[256] Cakmakyapan, S. et al. *Optics Express, Vol. 22, Issue 16, pp. 19504-19512* **2014**, *22*, 19504–19512.

[257] Bao, Y. J.; Li, H. M.; Chen, X. C.; Peng, R. W.; Wang, M.; Lu, X.; Shao, J.; Ming, N. B. *Applied Physics Letters* **2008**, *92*.

[258] Aslan, E.; Aslan, E.; Wang, R.; Hong, M. K.; Erramilli, S.; Turkmen, M.; Saracoglu, O. G.; Dal Negro, L. *ACS Photonics* **2016**, *3*, 2102–2111.

[259] Nagai, H. *Journal of Applied Polymer Science* **1963**, *7*, 1697–1714.

[260] Pelton, M.; Gray, S. K.; Wu, X. *Optics Express, Vol. 18, Issue 23, pp. 23633-23645* **2010**, *18*, 23633–23645.

[261] Kumar, M.; Dey, J.; Verma, M. S.; Chandra, M. *Nanoscale* **2020**, *12*, 11612–11618.

[262] Schwaighofer, A.; Brandstetter, M.; Lendl, B. *Chemical Society Reviews* **2017**, *46*, 5903–5924.

[263] Pillarisetty, R. *Nature 2011 479:7373* **2011**, *479*, 324–328.

[264] Reich, K. V.; Chen, T.; Shklovskii, B. I. *Physical Review B - Condensed Matter and Materials Physics* **2014**, *89*, 235303.

[265] Pietryga, J. M.; Park, Y. S.; Lim, J.; Fidler, A. F.; Bae, W. K.; Brovelli, S.; Klimov, V. I. *Chemical Reviews* **2016**, *116*, 10513–10622.

[266] Li, Y.; Qian, F.; Xiang, J.; Lieber, C. M. *Materials Today* **2006**, *9*, 18–27.

[267] Gellé, A.; Jin, T.; De La Garza, L.; Price, G. D.; Besteiro, L. V.; Moores, A. *Chemical Reviews* **2020**, *120*, 986–1041.

[268] Jia, C.; Lin, Z.; Huang, Y.; Duan, X. *Chemical Reviews* **2019**, *119*, 9074–9135.

[269] Lorchat, E.; López, L. E.; Robert, C.; Lagarde, D.; Froehlicher, G.; Taniguchi, T.; Watanabe, K.; Marie, X.; Berciaud, S. *Nature Nanotechnology 2020 15:4* **2020**, *15*, 283–288.

[270] Qiu, Z.; Tang, D. *Journal of Materials Chemistry B* **2020**, *8*, 2541–2561.

[271] Hochbaum, A. I.; Chen, R.; Delgado, R. D.; Liang, W.; Garnett, E. C.; Najarian, M.; Majumdar, A.; Yang, P. *Nature 2008 451:7175* **2008**, *451*, 163–167.

[272] Yang, S.; Qiu, P.; Chen, L.; Shi, X. *Small Science* **2021**, *1*, 2100005.

[273] Deng, J.; Su, Y.; Liu, D.; Yang, P.; Liu, B.; Liu, C. *Chemical Reviews* **2019**, *119*, 9221–9259.

[274] Wang, J.; Li, B.; Gu, T.; Ming, T.; Wang, J.; Wang, P.; Yu, J. C. *ACS Nano* **2014**, *8*, 8152–8162.

[275] Fang, J.; Zhou, Z.; Xiao, M.; Lou, Z.; Wei, Z.; Shen, G. *InfoMat* **2020**, *2*, 291–317.

[276] Kamata, Y. *Materials Today* **2008**, *11*, 30–38.

[277] Nguyen, P.; Ng, H. T.; Meyyappan, M. *Advanced Materials* **2005**, *17*, 549–553.

[278] Z. Pei, L.; Y. Cai, Z. *Recent Patents on Nanotechnology* **2011**, *6*, 44–59.

[279] Sze, S.; Ng, K. K. *Physics of Semiconductor Devices* **2006**,

[280] Kuo, Y. H.; Lee, Y. K.; Ge, Y.; Ren, S.; Roth, J. E.; Kamins, T. I.; Miller, D. A.; Harris, J. S. *Nature 2005 437:7063* **2005**, *437*, 1334–1336.

[281] Fox, M. A. M. *Optical properties of solids*; Oxford University Press, 2010; p 396.

[282] Wang, Z. L. *Journal of Physics: Condensed Matter* **2004**, *16*, R829.

[283] Sharma, D. K.; Shukla, S.; Sharma, K. K.; Kumar, V. *Materials Today: Proceedings* **2022**, *49*, 3028–3035.

[284] Strunk, J.; Kähler, K.; Xia, X.; Muhler, M. *Surface Science* **2009**, *603*, 1776–1783.

[285] Nuruddin, A.; Abelson, J. R. *Thin Solid Films* **2001**, *394*, 48–62.

[286] Song, J.; Wang, X.; Liu, J.; Liu, H.; Li, Y.; Wang, Z. L. *Nano Letters* **2008**, *8*, 203–207.

[287] Wang, Z. L.; Song, J. *Science* **2006**, *312*, 242–246.

[288] Carolan, D. *Progress in Materials Science* **2017**, *90*, 128–158.

[289] Zhu, X.; Ten Brink, G. H.; De Graaf, S.; Kooi, B. J.; Palasantzas, G. *Chemistry of Materials* **2020**, *32*, 1627–1635.

[290] Vaughn, D. D.; Schaak, R. E. *Chemical Society Reviews* **2013**, *42*, 2861–2879.

[291] Gerion, D.; Zaitseva, N.; Saw, C.; Casula, M. F.; Fakra, S.; Van Buuren, T.; Galli, G. *Nano Letters* **2004**, *4*, 597–602.

[292] Wagner, R. S.; Ellis, W. C. *Appl. Phys. Lett* **1964**, *4*, 89.

[293] Holmes, J. D.; Johnston, K. P.; Doty, R. C.; Korgel, B. A. *Science* **2000**, *287*, 1471–1473.

[294] Chockla, A. M.; Korgel, B. A. *Journal of Materials Chemistry* **2009**, *19*, 996–1001.

[295] Smith, D. K.; Lee, D. C.; Korgel, B. A. *Chemistry of Materials* **2006**, *18*, 3356–3364.

[296] Korgel, B. A. *One-Dimensional Nanostructures: Principles and Applications* **2013**, 41–63.

[297] Lu, H.; Meng, X. *Scientific Reports 2015 5:1* **2015**, *5*, 1–7.

[298] Di Martino, G.; Michaelis, F. B.; Salmon, A. R.; Hofmann, S.; Baumberg, J. J. *Nano Letters* **2015**, *15*, 7452–7457.

[299] Gong, B.; Shi, T.; Liao, G.; Li, X.; Huang, J.; Zhou, T.; Tang, Z. *Applied Surface Science* **2017**, *406*, 294–300.

[300] De Leon, N. P.; Lukin, M. D.; Park, H. *IEEE Journal on Selected Topics in Quantum Electronics* **2012**, *18*, 1781–1791.

[301] Caupin, F.; Herbert, E. *Comptes Rendus Physique* **2006**, *7*, 1000–1017.

[302] Fujiwara, H.; Suzuki, T.; Pin, C.; Sasaki, K. *Nano Letters* **2020**, *20*, 389–394.

[303] Pandres, E. P.; Crane, M. J.; Davis, E. J.; Pauzauskie, P. J.; Holmberg, V. C. *ACS Nano* **2021**, *15*, 8653–8662.

[304] Barbillon, G.; Bijeon, J. L.; Plain, J.; de la Chapelle, M. L.; Adam, P. M.; Royer, P. *Surface Science* **2007**, *601*, 5057–5061.

[305] Wen, J.; Wang, H.; Wang, W.; Deng, Z.; Zhuang, C.; Zhang, Y.; Liu, F.; She, J.; Chen, J.; Chen, H.; Deng, S.; Xu, N. *Nano Letters* **2017**, *17*, 4689–4697.

[306] Hooshmand, N.; Panikkanvalappil, S. R.; El-Sayed, M. A. *Journal of Physical Chemistry C* **2016**, *120*, 20896–20904.

[307] DIPHENYLGERMANE: 1675-58-7. https://www.chemicalbook.com/ProductChemicalPropertiesCB6474986{_}EN.htm.

[308] Fang, F.; Zhao, D. X.; Zhang, J. Y.; Shen, D. Z.; Lu, Y. M.; Fan, X. W.; Li, B. H.; Wang, X. H. *Nanotechnology* **2007**, *18*, 235604.

[309] Oh, D. K.; Choi, H.; Shin, H.; Kim, K.; Kim, M.; Ok, J. G. *Ceramics International* **2021**, *47*, 2131–2143.

[310] Xu, S.; Wang, Z. L. *Nano Research 2011 4:11* **2011**, *4*, 1013–1098.

[311] Wen, X.; Wu, W.; Ding, Y.; Wang, Z. L. *Journal of Materials Chemistry* **2012**, *22*, 9469–9476.

[312] Mullane, E.; Geaney, H.; Ryan, K. M. *Chemical Communications* **2012**, *48*, 5446–5448.

[313] Salamin, Y.; Ma, P.; Baeuerle, B.; Emboras, A.; Fedoryshyn, Y.; Heni, W.; Cheng, B.; Josten, A.; Leuthold, J. *ACS Photonics* **2018**, *5*, 3291–3297.

Appendix A

MATLAB Script Used to Generate Dose Contrasts Plots

```
clear;

count = 0; %%%Initialise counting function
P_i = 1;  %%%Initial pitch
P_f = 30;  %%% final pitch
pitch = zeros(1,P_f - P_i +1); %%%initialise pitch list
dminlist = zeros(1,length(pitch)); %%%initialise list to
   store values of dmin
contrast = zeros(1,length(pitch)); %%%initialise list to
   store values of contrast
contrast1 = zeros(1,length(pitch));%%%initialise list to
   store values of contrast for a second function

x = [0:0.5:195];
```

```
for p = P_i:P_f
    count = count + 1;
    pitch(count) = p;

    %%A unitless (n,m) coordinate system is used to define
        the 2D grid of point exposures. Units are obtained
       by
    %%multiplying by the pitch
    n = 0; %%%index of first coordinates



    d = floor(2000/p); %%%%distance between points in nm.
       the value in 'floor' is the size of the square
       writefield

    arr = [1:1:d]; %%%array containing number of points in
        n and m directions
    cpi = ceil(length(arr)/2); %%%centre point index i.e.
       the point at the centre of the grid

    %%Here we define empty lists to store the various
       variables so we can
    %%check them as required
    r1list = zeros(d);
    r2list = zeros(d);
    s1list = zeros(d,d);
    s1sqlist = zeros(d,d);
    xdminlist = zeros(d,d);
    xdmaxlist = zeros(d,d);
```

```
dmin = zeros(d,d);
dmax = zeros(d,d);
dmin1 = zeros(d,d);
dmax1 = zeros(d,d);

for i = 1: d
    n=n+1;
    m=0;%%%index of second coordinates
    r1 = cpi - n; %%Distance in n-direction from the
       centre
    r1sq = (cpi - n).^2;%%%% distance in the n-
       direction from the centre squared
    r1list(n) = r1;

    for j = 1: d
        m = m + 1;

        r2 = cpi - m; %%Distance in m-direction from
           the centre
        r2list(m) = r2;

        r2sq = (cpi - m).^2 ;%%%% distance in the m-
           direction from the centre squared

        s1 = cpi - m + 1/2;%%distance in the m-
           direction from the centre plus half a unit.
           This defines the point that uses the minimum
            dose
        s1sq = (cpi - m + 1/2)^2;%%distance in the m-
           direction from the centre plus half a unit
           squared
```

```
s1list(n,m) = s1;
s1sqlist(n,m) = s1sq;

xdmin = abs(p*(sqrt(s1sq + r1sq))); %%%
   distance from a point in the array to a
   point equidistant between the centre point
   and one of its nearest neighbour
xdminlist(n,m) = xdmin;

xdmax = abs(p*(sqrt(r2sq + r1sq))); %%%%
   distance from a point in the array to the
   centre point.
xdmaxlist(n,m) = xdmax;


%%%%% Simulation fitting function
%dmin(n,m) = 50*((1./(0.7).^2)*exp(-((xdmin)
   ./0.7).^2) + ((25)./(75.^2))*exp(-((xdmin)
   ./75).^2)) + 450*exp(-(xdmin)./1) + 200*sqrt
   (1./(1 + ((xdmin)./1.2).^5));
%dmax(n,m) = 50*((1./(0.7).^2)*exp(-((xdmax)
   ./0.7).^2) + ((25)./(75.^2))*exp(-((xdmax)
   ./75).^2)) + 450*exp(-(xdmax)./1) + 200*sqrt
   (1./(1 + ((xdmax)./1.2).^5));

%%%%He Ion experiment fitting function using
   filter funciton
%dmin(n,m) = sqrt(1/(1+(xdmin/3).^10));
%dmax(n,m) = sqrt(1/(1+(xdmax/3).^10));
```

```
        %%%%% Fullerene fitting function
        dmin(n,m) = sqrt(1/(1+(xdmin/3).^10));
        dmax(n,m) = sqrt(1/(1+(xdmax/3).^10));
        %%%%% EBL Paper fitting function
        %dmin1(n,m) = 1/(1 + (xdmin/0.5).^2.1);
        %dmax1(n,m) = 1/(1 + (xdmax/0.5).^2.1);
       end

    end


dmintotal1 = sum(dmin,1);
dmintotal2 = sum(dmintotal1);

dmaxtotal1 = sum(dmax,1);
dmaxtotal2 = sum(dmaxtotal1);

dmaxlist(count) = dmaxtotal2;
dminlist(count) = dmintotal2;

contrast(count) = (dmaxtotal2-dmintotal2)./(dmaxtotal2
   +dmintotal2);

dmin1total1 = sum(dmin1,1);
dmin1total2 = sum(dmin1total1);

dmax1total1 = sum(dmax1,1);
dmax1total2 = sum(dmax1total1);

dmax1list(count) = dmax1total2;
dmin1list(count) = dmin1total2;
```

```
    contrast1(count) = (dmax1total2-dmin1total2)./(
       dmax1total2+dmin1total2);
end


plot(pitch,contrast, pitch,contrast1)
```

Appendix B

Data Generation for Simulated PSFs

In order to simulate the PSF for various resist materials on a SiN_x two inputs must be first generated. The first input is the trajectory of He^+ ions, and is generated using the SRIM package. The inputs for both PMMA and a fullerene-derivative resist are shown below. After ion trajectories were calculated with SRIM, the output file, "COLLISION.txt", is tidied up with the following Python script to give a new text file; "COLLISION-fancy.txt".

```
import re

f = open('sim_COLLISION.txt','r')
fp = open('sim_COLLISION-fancy.txt','w')

# pass annoying non-data line tha starts with \xb3
for line in f:
    if line[0]=='\xb3': break

for line in f:
    if line[0]=='\xb3':
        m = re.split('\xb3',line)
```

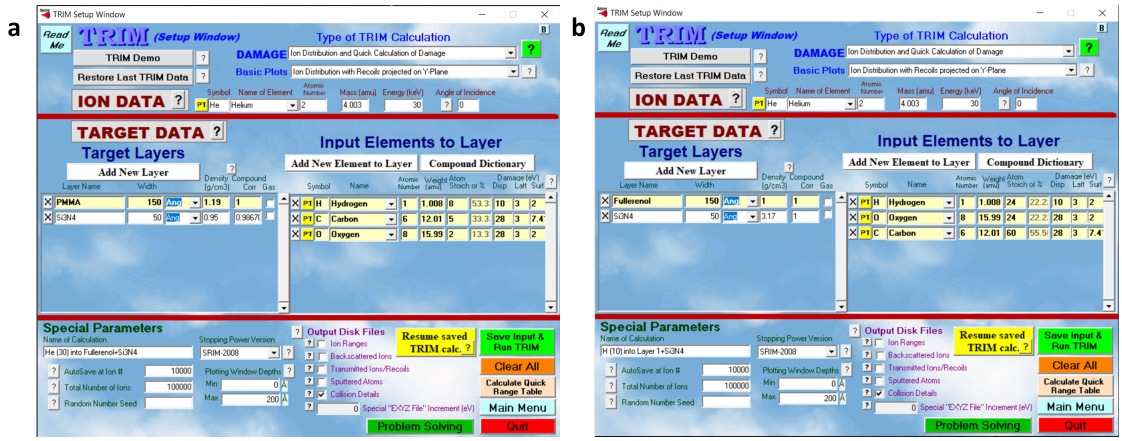

Figure B.1: SRIM inputs used to generate He^{+} ion trajectories for (a) PMMA and (b) a fullerene-derivative resist.

```
        ionNum, energy, z, y, x, SP = m[1], m[2], m[3], m
           [4], m[5], m[6]
        fp.write(ionNum+" "+energy+" "+z+" "+y+" "+x+" "+
           SP+"\n")

f.close()
fp.close()
```

To generate the second input file for the simulation the following Python is used to generate the stoichiometry of the resists.

```
# -*- coding: utf-8 -*-
"""
Created on Thu May  7 12:31:13 2020

@author: OMEARARO
"""


''' Put the material you want at the end '''


# # PMMA -> (C5O2H8)n
```

```
# names = 'H','C','O'
# numbers = 1, 6, 8
# weights = 1.0079, 12.0107, 15.999
# stoichs = 8, 5, 2
# d = 1.19 # total density, in g/cm^3

# #HSQ
# names = 'H', 'Si', 'O'
# numbers = 1, 14, 8
# weights = 1.008, 28.09, 16.000 # atomic weights of H, Si
   , O
# stoichs = 8, 8, 12 # stoichiometry: H8Si8O12
# d = 1.4 # total density, in g/cm^3

#Fullerenol
names = 'H', 'C', 'O'
numbers = 1, 6, 8
weights = 1.008, 12.0107, 15.999
stoichs = 24, 60, 24
d = 1

if len(weights) != len(stoichs) and len(weights) != len(
   names):
    print( "error: weights and stoichs must be equal in
       size")
    import sys; sys.exit(1)
material_weight = sum([s*w for s,w in zip(stoichs,weights)
   ])

# A human-friendly format
for n,w,s in zip(names, weights, stoichs):
```

```
    print( "density of species",n,"is", d*w*s/
       material_weight)

# For copy-and-paste into a simulation input file
print( len(names))
for Z,w,s in zip(numbers, weights, stoichs):
    print( Z)
    print( w)
    print( d*w*s / material_weight)
```

The results from this script are then input into a text file to generate the second input for the PSF simulation. The text file is in the format shown below.

```
1               ##Path pruner. Set to 1
1               ##No. of generations of SEs
59              ##Cutoff energy in eV
2               ##No. of layers i.e. resist + substrate
150             ##Thickness of layer 1 (resist) in
   Angstrom
3               ##No. of elements in layer. The next 9
   lines are output of Python script
1               ##Atomic No. of first element
1.008           ##Atomic mass of first element
0.02143141892789752             ##Component density of
   first element
6               ##Atomic No. of second element
12.0107         ##Atomic mass of second element
0.6384085895766338              ##Component density of
   second element
8               ##Atomic No. of third element
15.999          ##Atomic mass of third element
0.3401599914954687              ##Component density of
```

```
   third element
50              ##Thickness of layer 2 (SiNx substrate)
2               ##No. of elements in layer
14              ##Atomic No. of Si
28.08           ##Atomic mass of Si
0.8409583571021105              ##Component density of Si
7               ##Atomic No. of N
14              ##Atomic mass of N
0.5590416428978893              ##Component density of SiN
10              ##Lateral mesh size in Angstrom
50              ##Vertical mesh spacing in Angstrom
1               ##States only a single plane is analysed
   for energy dissipation
50              ##slice width in Angstrom
100000          ##No of ions analysed
15.6            ##Stopping power of resist in eV/Angstrom
```

The two input files are then used as arguments in the ”Simulation.java” file. The full simulation repository can be found at:

https://github.com/dwinston/jprox-hebeam

Appendix C

Lumerical Script to Calculate Extinction Spectra

Lumerical FDTD simulation regions and script files were generated by modifying the "Plasmon Mode Excitation" sample file available from Ansys.com. The script used to calculate the extinction spectra shown in this thesis is given below.

```
##############################################
 ##Script: plasmon_mode_excitation_scattering_linear.lsf
 ##this script will plot the results from the parameter
 ##sweep.

 #####Variables:
 #####run_sim:     0, do not run any simulation (load
    results from file)
              ####1, run simulations (parameter sweep)

 ##########Copyright 2019 Lumerical Inc.
##############################################
clear;
sweep_name = "sweep_polarization";
```

```
###run;

run_sim = 1; # 0, do not run any simulation
              #####1, run sweep

if (run_sim) {
    runsweep(sweep_name);
}

scat = getsweepresult(sweep_name, "scat");
total = getsweepresult(sweep_name, "total");

wavelength = scat.lambda;
scat = scat.sigma;
total = -total.sigma;
ext = scat + total;

##############################################
###Varibles for Title
#select("::model::rbowtie");
#R = get("radius")*1e9;
#L = get("triangle_side_length")*1e9;
#S = get("separation")*1e9;


#select("::model::mesh");
#M = 0;
#en = get("enabled");
#if (en == 0){
    #M = 0;
```

```
#} else{
    #select("::model");
    #M = get("mesh_size")*1e9;
#}

#P = 00;

#select("::model::FDTD");
#x = get("x max bc");
#if (x == "PML"){
    #P = 00;
#} else{ select("::model");
    #P = get("simulation_x_span")*1e9;
#}


#select("::model::FDTD");
#T = get("simulation time")*1e15;


##############################################
# Linear x
#plot(wavelength, pinch(scat, 2, 1), pinch(total, 2, 1),
   pinch(ext, 2, 1),
  #  "wavelength (um)", "cross section (m^2)");#,
    #"R = " + num2str(R) + "nm L = " + num2str(L) + "nm S
       = " + num2str(S) + "nm M = " + num2str(M) + "nm P =
       " + num2str(P) + "nm T = " + num2str(T) + "fs");
#plot(wavelength, pinch(ext, 2, 1),
    #"wavelength (um)", "cross section (m^2)", "Extinction
       ");
```

```
#setplot("x min", 3*10^-7);
#setplot("x max", 100*10^-7);
#legend("Scattering", "Absorption", "Extinction");

plot(wavelength, pinch(ext, 2, 1),
    "wavelength (um)", "cross section (m^2)", "Extinction
       ");

legend( "Extinction");
```